Title
New Probes of Axions and Ultra-Heavy Dark Matter

Author
Riggins, Paul

Publication Date
2019

Peer reviewed|Thesis/dissertation

New Probes of Axions and Ultra-Heavy Dark Matter

by

Paul Riggins

A dissertation submitted in partial satisfaction of the

requirements for the degree of

Doctor of Philosophy

in

Physics

in the

Graduate Division

of the

University of California, Berkeley

Committee in charge:

Assistant Professor Surjeet Rajendran, Chair
Professor Lawrence Hall
Professor Eliot Quataert

Spring 2019

New Probes of Axions and Ultra-Heavy Dark Matter

Abstract

New Probes of Axions and Ultra-Heavy Dark Matter

by

Paul Riggins

Doctor of Philosophy in Physics

University of California, Berkeley

Assistant Professor Surjeet Rajendran, Chair

The Standard Model of particle physics is known to be incomplete, and many extensions and modifications have been proposed to resolve outstanding issues. In order to discriminate which of these many ideas may be correct, we seek novel approaches to acquire new data and apply old data. The research in this dissertation advances these efforts, probing physics beyond the Standard Model in three distinct ways. First, we propose a novel design of a laboratory search for axions based on photon regeneration with superconducting radiofrequency resonant cavities. We use a confined static magnetic field to avoid degrading the large resonant quality factors. After analysis of fundamental issues and limitations, we conclude this design can potentially probe axion-photon couplings beyond astrophysical limits, comparable and complementary to next generation optical experiments. Second, we demonstrate that rotational superradiance can be efficient in millisecond pulsars. We use measurements from the two fastest known pulsars to place bounds on bosons with masses below 10^{-11} eV and Yukawa couplings to neutrons, exceeding fifth force constraints by 3 orders of magnitude for masses near the pulsar rotation rates. For certain neutron star equations of state, these measurements also constrain the QCD axion. Third, we consider dark matter (DM) candidates that heat white dwarfs through the production of high-energy Standard Model (SM) particles, and show that such particles will efficiently thermalize the stellar medium and ignite type Ia supernovae. Based on the existence of long-lived white dwarfs and the observed supernovae rate, we derive new constraints on DM with masses greater than 10^{16} GeV which produce SM particles through DM-DM annihilations, DM decays, and DM-SM scattering interactions in the stellar medium.

Soli Deo Gloria

Contents

List of Figures

Acknowledgments

This dissertation and PhD would not have been possible except for the help and support of many people.

I want to thank Surjeet Rajendran, my advisor, for many refreshing and formative perspectives on physics and research, and for the ways he supported me during my PhD. I am deeply grateful to my colleagues and friends Ryan Janish and Vijay Narayan, for countless hours doing physics together, fruitful collaborations that led to the majority of this dissertation. I thank also my other co-authors Peter Graham and David E. Kaplan, as well as the many other physics colleagues at UC Berkeley and elsewhere who contributed to this research through feedback and stimulating discussions.

I'd like to thank the wonderful staff of the Physics Department, especially Ben Spike (now at Wisconsin), Amanda Dillon, and Joelle Miles, for their tireless support of students, and for many good conversations and hours working together on the Major Curriculum Committee and Berkeley Connect.

My work at Berkeley was generously supported in part by the UC Berkeley Presidential Chair Fellows Curriculum Enrichment Grant Program and the Berkeley Connect Fellowship, in conjunction with the Physics Department. I am grateful for this support, and for the curriculum development and mentoring experiences I got to enjoy through these opportunities.

I am indebted to Drs. Andrew Lui and Sue Gritzner for helping me get back on my feet; and to Ben Meyer and Ryan Hileman for the Voicecode and Talon projects, respectively, that have helped me use my computer again, both for physics and the rest of life.

I want to thank Isaac and Kayla Wolf, the best neighbors ever, and all of my friends in Monday Small Group, the rest of Veritas Graduate Christian Fellowship, and elsewhere, for giving me community, perspective, prayer, and friendship through my years here.

I want to thank my loving parents, sister, and brother-in-law, Bruce and Judy Riggins and Sharon and Stephen Crane, without whom I never would have made it to Berkeley, much less through it.

And most of all, I am deeply grateful and indebted to Marquita Ellis, my dear wife, for her endless love, support, prayers, advice, and encouragement through this degree, all while successfully navigating the rigors of her own PhD. You are amazing.

Chapter 1

Motivation and Overview

The Standard Model of particle physics is perhaps the most successful scientific theory of all time, in its predictive power. However, we know it to be an incomplete description of the particle content and physical laws of nature. It seems unable to account for dark matter, for instance, and it does not describe quantum gravity, just to name two of the missing pieces. New particles are expected to appear at energies higher than we have probed, and quantum field theory itself may need to give way to a more complete description.

To address these failings, theoretical researchers have invented and investigated a dizzying variety of effective field theories and conceptions of quantum gravity, most of which purport to fill one or another of the gaps in the Standard Model and which claim to be consistent with current experimental data. Some of these models are considered "well-motivated" and receive disproportionate community attention, since they may be able to economically solve a number of problems at once, and/or they have well-developed origin stories in cosmological history. Other models are more generic, parameterizing certain properties and interactions (like a mass and cross-section for dark matter) without concern for the specific microphysics or origins that would give rise to them. Most of these proposed ideas, well-motivated or not, will turn out to be wrong—the challenge for physics, as an experimental science, is to sort out which ones.

The research presented in this dissertation has been developed in response to this challenge, seeking to probe and constrain the existence of new physics beyond the Standard Model. The three projects contained in the subsequent chapters illustrate a spectrum of approaches including both detection and exclusion efforts, terrestrial and astrophysical data sources, well-motivated and "exotic" models. There is no guarantee that our theoretical biases, which have led us to favor some ideas over others, will continue to be faithful guides. This work broadly takes the view that we have little idea where new physics will be discovered next, or what it will be, so it is prudent to look for and apply new data and phenomena wherever we can find them.

Here is an overview of the projects presented:

Chapter 2 is a detection effort, proposing a new terrestrial experiment to look for axions with electromagnetic couplings. We describe a novel light-shining-through-walls set up and

consider key fundamental issues necessary for the experiment to be successful and on par with other next-generation proposals. This work was done in collaboration with Ryan Janish, Vijay Narayan, and Surjeet Rajendran; the chapter is adapted from our paper [1].

Chapter 3 also constrains axions and axion-like particles, but by supposing couplings to neutrons and using existing astrophysical data from millisecond pulsars. We demonstrate how ultralight particles could drive rapid superradiant growth, causing a star to spin down below observed rotation rates. This is primarily an exclusion effort, but also hints at new particles and astrophysical signatures to look for. This work was done in collaboration with David E. Kaplan and Surjeet Rajendran; the chapter is adapted from our paper, in preparation [2].

Chapter 4 is another exclusion effort using existing astrophysical data, using white dwarfs and type Ia supernovae to constrain ultra-heavy dark matter with a wide variety of Standard Model couplings. We investigate how such particles would cause white dwarfs to explode, ruling out dark matter candidates because we see the stars still intact. Our results also suggest distinct characteristics of dark matter-induced supernovae, which could be investigated in future searches. This work was done in collaboration with Peter W. Graham, Ryan Janish, Vijay Narayan, and Surjeet Rajendran; the chapter is adapted from our paper [3].

Chapter 2

Axion production and detection with superconducting RF cavities

We propose a novel design of a laboratory search for axions based on photon regeneration with superconducting RF cavities. Our particular setup uses a toroid as a region of confined static magnetic field, while production and detection cavities are positioned in regions of vanishing external field. This permits cavity operation at quality factors of $Q \sim 10^{10} - 10^{12}$. The limitations due to fundamental issues such as signal screening and back-reaction are discussed, and the optimal sensitivity is calculated. This experimental design can potentially probe axion-photon couplings beyond astrophysical limits, comparable and complementary to next generation optical experiments.

2.1 Introduction

Axions are well-motivated additions to the standard model (SM). They provide an elegant solution to the strong CP problem [4, 5, 6, 7], are a natural dark matter candidate [8, 9, 10], can relax naturalness problems [11, 12], and appear generically in theories of quantum gravity [13, 14]. Purely laboratory searches for axions are thus an important experimental front. Given that axions can naturally be very light and have suppressed interactions with the SM, a promising approach is to search for the coherent interaction of a classical axion field with electromagnetic (EM) fields [15].

Photon regeneration, or "Light Shining Through Walls" (LSW), experiments make use of axion-photon oscillations in a transverse magnetic field to convert photons into axions that can traverse an optical barrier and then convert back into detectable photons [16]. Small axion-photon conversion probabilities are overcome by the use of resonators to sustain large EM fields [17]. This is the basis of experiments such as the Any Light Particle Search (ALPS) [18, 19, 20], which employ optical cavities aligned with dipole magnets over a long baseline. LSW can also be done at radio frequencies (RF) [21, 22, 23], as in the CERN Resonant Weakly Interacting sub-eV Particle Search (CROWS) [24], by producing and detecting

the axion through excited modes in matched RF cavities subject to an external magnetic field. While interesting, current constraints from LSW experiments are less stringent than those due to stellar cooling or searches for solar axions (see [25] for a review).

We propose a novel design for an axion LSW experiment using high-Q superconducting RF (SRF) cavities, which can in principle reach beyond these astrophysical bounds. SRF cavities provide an opportunity for a significantly enhanced axion search due to their extremely large quality factors; however, they must be isolated from large magnetic fields in order to avoid catastrophic SRF degradation. This requires several qualitative modifications from previous setups, most notably the use of a sequestered axion-photon conversion region containing a confined static magnetic field while production and detection cavities are positioned in regions of vanishing static field. The focus of this paper is to determine the fundamental factors that affect the sensitivity of such an experimental design—a more detailed consideration of experimental strategies is left to future work. We calculate the optimal signal strength and irreducible noise sources, and find the proposed setup capable of probing axion-photon couplings beyond astrophysical limits and with a reach comparable and complementary to next generation optical experiments.

2.2 Conceptual Overview

LSW searches rely on the axion EM interaction, given by the effective Lagrangian

$$-\frac{1}{4}F_{\mu\nu}F^{\mu\nu} + \frac{1}{2}(\partial_\mu a)^2 - \frac{1}{2}{m_a}^2 a^2 - \frac{1}{4}gaF_{\mu\nu}\widetilde{F}^{\mu\nu}, \tag{2.1}$$

where a is the axion field of mass m_a, $\widetilde{F}^{\mu\nu} = \epsilon^{\mu\nu\rho\sigma}F_{\rho\sigma}$, and g is the axion-photon coupling. In the limit of classical fields, an axion obeys the equation of motion

$$\left(\Box + m_a^2\right) a = -g\vec{E}\cdot\vec{B}, \tag{2.2}$$

and modifies Maxwell's equations:

$$\vec{\nabla}\cdot\vec{E} = -g\vec{B}\cdot\vec{\nabla}a, \tag{2.3}$$

$$\vec{\nabla}\times\vec{B} = \frac{\partial\vec{E}}{\partial t} - g\left(\vec{E}\times\vec{\nabla}a - \vec{B}\frac{\partial a}{\partial t}\right). \tag{2.4}$$

We will generally consider any light, neutral pseudoscalar a and treat $\{m_a, g\}$ as independent parameters.

In an RF LSW experiment such as CROWS [24], a production cavity sources axions through a non-vanishing $\vec{E}\cdot\vec{B}$, where $\vec{E}$ is the electric field of an excited cavity mode and $\vec{B}$ is an external, static magnetic field. These axions propagate into a detection cavity where, again in the presence of a static magnetic field, they excite an identical frequency mode in the detection cavity. The signal power that can be extracted is [21]:

$$P_{\text{signal}} = P_{\text{input}}Q_{\text{pc}}Q_{\text{dc}}\left(\frac{gB_0}{f}\right)^4|G|^2. \tag{2.5}$$

Here $Q_{\rm pc}$ and $Q_{\rm dc}$ are the loaded quality factors of production and detection cavities, $f \approx$ GHz is the frequency of the excited modes, $P_{\rm input}$ is the driving RF power delivered to the production cavity, and B_0 is the static field penetrating both cavities. $|G|$ is a form factor which depends on the arrangement of the cavities, choice of modes, etc. This is roughly constant for $m_a \lesssim 2\pi f$, and is exponentially suppressed for larger masses.

The quality factors Q of both cavities are key factors in determining the sensitivity of such an experiment. For normal conducting cavities, $Q \sim 10^5 - 10^6$, however advances in SRF technology have led to the development of superconducting cavities with $Q \sim 10^{10} - 10^{12}$ which have application in particle accelerators [26]. It is worthwhile to consider whether these can be leveraged in an axion LSW search [27, 28].[1] A simple replacement of the RF cavities[2] in the above arrangement with SRF cavities does not work—an external B_0 greater than the critical field $\sim 0.2\,\mathrm{T}$, at which flux penetrates the cavity, would result in excessive dissipation and degrade Q.

This problem is avoided by placing production and detection SRF cavities in regions of vanishing static field while confining a large, static magnetic field in a distinct conversion region, depicted schematically in Fig. 2.1. The basic elements of an SRF LSW experiment as follows:

1. Axions are sourced in a production cavity free of any external field.

2. The axions then convert into photons in an isolated region of static magnetic field.

3. The resulting photons propagate out of the conversion region—that is, the axion-induced fields must not also be screened by the conductors which confine the large static field.

4. Any resulting RF signal is coupled to and amplified by an SRF detection cavity.

We discuss a possible design that is able to realize all these conditions, and in what follows we will use it to determine the optimal sensitivity of an axion SRF search.

(1) A specific mode or set of modes in the production cavity is driven such that $\vec{E} \cdot \vec{B}$ does not identically vanish.

(2) A static B_0 is generated and confined by DC current-carrying superconducting wires wrapped to form a toroidal enclosure.

(3) There is a gap in this enclosure, preventing the toroid from acting as a shielding cavity for the axion-induced fields. Our use of a gapped toroid is inspired by its related use in experiments (ABRACADABRA and DM Radio) searching for dark matter axions [30, 31].

(4) The axion-induced fields are coupled to the detection cavity inductively via an outside pickup loop. Here, we must properly account for the back-reaction of the amplified signal

[1] See [29] for a proposal to detect axions with SRF cavities that is quite distinct from ours.

[2] It is actually not obvious whether a larger signal is obtained by replacing both cavities or only the detection cavity, see Sec. 2.3.1—we choose here to study an SRF production cavity as it involves some novel considerations.

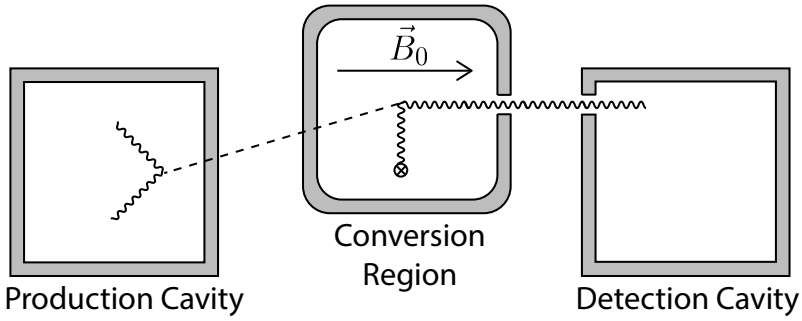

Figure 2.1: Basic elements of an axion LSW experiment using SRF cavities and a conversion region of confined static magnetic field, to be contrasted with an RF cavity experiment such as CROWS [24].

onto the toroid. We emphasize that a realistic implementation would require a more detailed signal field read-out mechanism in order to maintain a large effective Q on the detection side.

2.3 Determining the Axion Signal

2.3.1 SRF axion source

The axion field produced by an SRF cavity is given by (2.2), with the EM fields on the right-hand-side being those of the driven cavity modes. We focus on one frequency component ω of this $\vec{E} \cdot \vec{B}$, which may arise from a single cavity mode with frequency $\omega/2$ or from two distinct modes driven together whose frequency sum or difference is ω:

$$a\left(\vec{x}, t\right) = -g\, e^{i\omega t} \int_{\mathrm{pc}} d^3\vec{y}\, \frac{e^{ik_a|\vec{x}-\vec{y}|}}{4\pi|\vec{x}-\vec{y}|} \left(\vec{E} \cdot \vec{B}\right)_\omega , \tag{2.6}$$

where $k_a = \sqrt{\omega^2 - m_a^2}$ is the axion momentum and the subscript ω on $\vec{E} \cdot \vec{B}$ indicates restriction to a single frequency component. The integration $\vec{y}$ is taken over the volume of the production cavity and $\vec{x}$ indicates any point in space, e.g., within the conversion region. The driven modes must be chosen such that $(\vec{E} \cdot \vec{B})_\omega$ is not vanishing. This is not an issue in principle, though care must be taken in order to ensure the largest possible magnitude of the axion source (see Appendix A.1).

An SRF production cavity is unable to support EM fields greater than the critical field at which Q severely degrades due to flux penetration. This sets a fundamental limit on the strength of an SRF axion source which is independent of the cavity Q, the input power, or choice of modes. The limit depends only on the material properties of the chosen superconductor. For a standard niobium SRF cavity [32], the field limit is

$$(\vec{E} \cdot \vec{B})_{\mathrm{srf}} \lesssim (0.2\ \mathrm{T})^2. \tag{2.7}$$

By comparison, the axion source produced by an RF cavity in a large static field (as in CROWS) is

$$(\vec{E}\cdot\vec{B})_{\rm rf} \sim (0.1\ {\rm T})^2 \left(\frac{P_{\rm input}}{100\ {\rm W}}\right)^{\frac{1}{2}} \left(\frac{Q_{\rm pc}}{10^5}\right)^{\frac{1}{2}} \left(\frac{B_0}{5\ {\rm T}}\right). \tag{2.8}$$

Interestingly an SRF axion source may be similar in magnitude to that of a conventional LSW setup. The improved reach of our set-up is primarily due to the increase in Q on the detection side, and the decision to employ an SRF or RF cavity for production would depend on more detailed engineering considerations.

2.3.2 Gapped toroid conversion region

An axion interacts with the $\vec{B}_0$ within our conversion region and induces EM fields, described to leading order by effective sources

$$\rho_{\rm eff} = -g\vec{B}_0\cdot\vec{\nabla}a, \qquad \vec{J}_{\rm eff} = g\vec{B}_0\partial_t a \tag{2.9}$$

For a toroidal magnet, the static field is of the form $\vec{B}_0 \sim B_0(r)\,\hat{\phi}$ within the volume of the toroid, and ideally vanishes everywhere outside. This is the principle advantage of using a toroid, as the SRF cavities can be located in regions of nearly vanishing static field. However it is essential that the toroid be gapped, for instance due to spaces between wire turns. A gapped toroid of this sort acts as a polarizer, confining the toroidal static field while permitting the poloidal axion-induced field to propagate outside and be detected, as shown in Fig. 2.2. Indeed, this behavior is same reason that a gapped toroid is being employed in [31, 30].

We can understand this as follows: the axion effective current $\vec{J}_{\rm eff}$ follows the direction of the static toroidal field $\vec{B}_0$ and sources a poloidal field $\vec{B}_a$. Both fields vanish in the toroid thickness as Meissner screening currents are set up on the internal surface. The static field requires poloidal surface currents which are unaware of gaps in the toroid—they do not encounter the gaps as they circulate. For this reason, the static B-field is effectively contained within the toroid. Any leakage is due to fringe effects, which are suppressed by the small size of the gap and can be made smaller than the critical SRF threshold. On the other hand, the axion-induced field will drive toroidal currents which are aware of the gaps. An internal toroidal current must either collect charge on the edges of the gap or propagate onto the external surface of the toroid, where it sources detectable field. This field is unsuppressed by the gap size, as long as the gap has a sufficiently small parasitic capacitance (see Sec. 2.3.4).

We now make the approximation that all length scales in the setup (cavity sizes, separations, dimensions of the toroid, etc.) are comparable and of order ω^{-1}. We additionally assume that the axion-induced poloidal field B_a is able to escape the toroid without suppression, as though the conducting toroid were not present. This is valid in the quasistatic limit, as we motivate in Sec. 2.3.3. Combining (2.6) and (2.9), we find the axion-induced

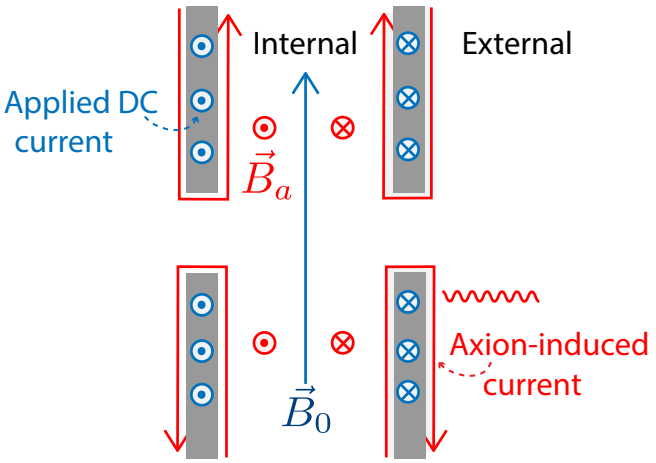

Figure 2.2: Schematic of the gapped toroid as a polarizer, zoomed on to the cross-section of a gap. The static $\vec{B}_0$ due to applied DC current (blue) remains internal, while the axion-induced $\vec{B}_a$ (red) causes Meissner screening currents (also red) to flow on internal and external surfaces due to the gap. The external currents give rise to detectable fields outside the toroid.

field in the center of the torus has a magnitude

$$B_a = \frac{g^2 B_{\rm pc}^2 B_0}{\omega^2}\beta \tag{2.10}$$
$$\approx 10^{-26}\ \mathrm{T}\left(\frac{g\ \mathrm{GeV}}{10^{-11}}\right)^2\left(\frac{B_{\rm pc}}{0.2\ \mathrm{T}}\right)^2\left(\frac{B_0}{5\ \mathrm{T}}\right)\left(\frac{\beta}{0.05}\right),$$

where $B_{\rm pc}$ is the field amplitude in the production cavity (note, we have simply taken $E_{\rm pc} \sim B_{\rm pc}$ in the above estimate) and $\omega \sim 2\pi\,\mathrm{GHz}$. β is a dimensionless form factor which is a function of the cavity modes, cavity and toroid geometries, spatial variation in $\vec{B}_0$, etc. The size of β is estimated in Appendix A.1, and we find in principle that it can be made $\mathcal{O}(0.1)$ in the limit $m_a \ll \omega$.

2.3.3 Screening beyond the quasistatic limit

The reasoning presented above for the propagation of axion-induced fields outside the gapped toroid is essentially valid for quasistatic frequencies, $R \lesssim \omega^{-1}$, where R is the characteristic dimension of the toroid. In the low-frequency limit, the axion-induced magnetic field scales as $B_a \propto (R\omega)$ and so we would try make our toroid as large as possible. However once R becomes larger than ω^{-1} the axion-induced fields outside the toroid are suppressed (or *screened*), and thus an optimal design would saturate the quasistatic limit $R \sim \omega^{-1}$. We discuss this in detail in Appendix A.2; here we will briefly describe the physical reasons for this result.

Beyond the quasistatic limit, the cross-capacitance of the toroid becomes important: radiation across the center will cause currents and charges on one side of the toroid to affect those on the other side. Meissner currents flowing along the surface of the toroid are no longer approximately uniform; instead, there will be multiple sections of current flowing in opposite directions, with alternating charge buildups in between. The resulting Meissner currents and charge distribution is spatially modulated and behaves as a multipolar source. We thus expect the axion-induced fields outside the toroid to drop-off parametrically as a power-law $B_a \propto (R\omega)^{-n}$, due to destructive interference of out-of-phase source contributions. We show this behavior and calculate $n > 0$ explicitly for a toy model of a thin cylindrical conductor in the high-frequency limit in Appendix A.2. Thus, we expect it is safe to saturate $R \sim \omega^{-1}$ without concern that there will be a precipitous (e.g., exponential) drop in the external fields for slightly larger sizes or frequencies. Likewise, we may treat the approximation of $\mathcal{O}(1)$ field propagation as accurate even at the boundary of the quasistatic limit.

Note that in our setup the internal toroid signal currents will also have significant spatial modulation beyond the quasistatic limit, but for a very different reason: the source axion field (2.6) itself varies on length scales of order ω^{-1} due to the propagator factor, independent of the choice of modes. In any case, the multipolar screening described in this section is more general and results from satisfying boundary conditions on the superconducting toroid—this would be present even if the axion field were spatially uniform.

2.3.4 Pickup and equivalent transducer circuit

To compute the signal strength, it is useful to describe this system with a model circuit, as in the left side of Fig. 2.3. For concreteness we assume the axion-induced EM field is coupled to the detection cavity via a pickup loop located in the central hole of the toroid. An actual design would likely require a more sophisticated read-out mechanism in order to maintain a large effective Q, however this does not alter the optimal signal power.

The model circuit is a straightforward rendering of the signal current flowing on the toroid. This current flows toroidally, distributed over the inner and outer surfaces of the toroid, as discussed in Sec. 2.3.2. We focus on the loop of signal current nearest to the pick-up loop, which flows around the central hole, concentric to the pick-up. This current path is represented in the model circuit by the red arrows in Fig. 2.3, and it includes segments on both the inner and outer toroid surface. The magnitude of toroid current is determined by the Meissner boundary conditions. It thus receives contributions from the magnetic fields produced by both the axion effect current and any current in the pick-up loop, the latter being a back-reaction which sets the maximal power that may be drawn from the pick-up loop.

The axion effective current in the volume of the toroid is represented by I_a, and its coupling to the inner toroid surface current by an effective mutual inductance M_a. The self inductance of the toroid current path is $L_t \sim R$, with R the toroid radius. We choose $M_a \sim R$, which ensures that the current driven in the model circuit due to I_a agrees with that required by the Meissner effect. The current induced on the inner surface of the toroid

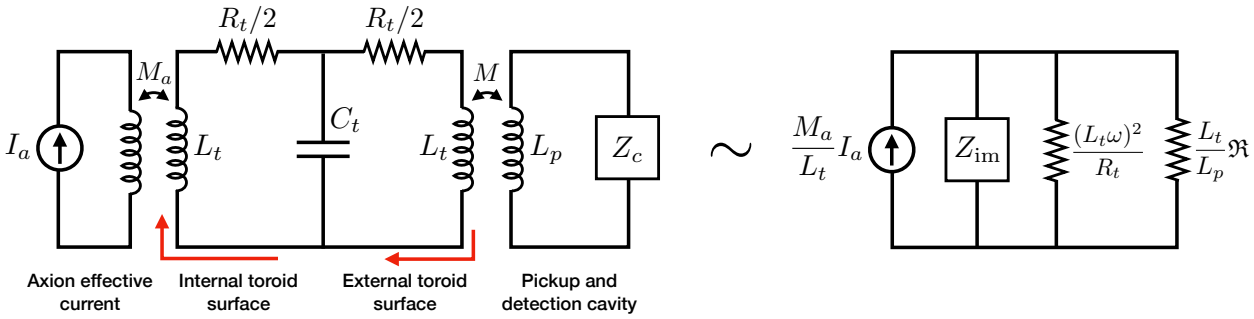

Figure 2.3: (Left) Mapping of our experimental setup onto an effective circuit model. This is parameterized by an axion effective current (I_a) running through the toroid volume, effective mutual inductance capturing the Meissner effect (M_a), toroid inductance (L_t), toroid resistance (R_t), shunting capacitance (C_t), inductive coupling to an outside pickup loop (L_p) through a mutual coupling (M), and a detection cavity (Z_c). (Right) Approximate equivalent circuit, for the purposes of computing the maximum signal power. $\mathfrak{R} \propto Q$ is the detection cavity shunt resistance and $Z_{\rm im}$ contains all imaginary impedances.

can pass to the outer surface, where it couples to a pickup loop of inductance L_p through a mutual inductance M and then feeds into a cavity of impedance Z_c. Alternatively, the current may jump across the gaps between wires and remain on the inner surface: this is captured by the shunting capacitance C_t. As we will show, $\omega L_t \ll (\omega C_t)^{-1}$, and so current always prefers to circulate between the inner and outer surfaces.

The resistances R_t account for the tiny but non-zero surface losses on the toroid. It is valid to ignore R_t when determining the magnitude of axion-induced fields through (2.10). However, it is important not to ignore it entirely when considering the amplification of signal fields by the SRF cavity. The detection cavity will be rung up to contain a large current, for which the pickup loop L_p will act as an antenna and excite additional currents on the external surface of the toroid, resulting in additional dissipation via R_t. This back-reaction current is again set by the Meissner boundary conditions, which are reproduced by M and $L_t \sim R$ in the circuit model of Fig. 2.3. Taking the pick-up loop to have radius r and contain a current I_p, it will source a field at the toroid surface $B \sim I_p r^2/R^3$ which requires a Meissner current $I \sim BR \sim I_p r^2/R^2$. Since the mutual inductance is of order $M \sim r^2/R$, the required current is indeed $I \sim I_p M/L_t$ that derived from considering our circuit.

We now estimate the relevant model circuit parameters. The current source I_a represents the total axion effective current threading the toroid and is of order $J_{\rm eff}R^2$. More precisely, it is the current that gives rise to the outside field B_a (2.10):

$$\begin{aligned} I_a \sim B_a R &\sim \frac{g^2 B_{\rm pc}^2 B_0}{\omega^3}\beta \\ &\approx 10^{-13}\ \text{nA}\ \left(\frac{g\ \text{GeV}}{10^{-11}}\right)^2 \left(\frac{B_{\rm pc}}{0.2\ \text{T}}\right)^2 \left(\frac{B_0}{5\ \text{T}}\right) \left(\frac{\beta}{0.05}\right), \end{aligned} \tag{2.11}$$

again with $\omega = 2\pi\,\mathrm{GHz}$ and $m_a \ll \omega$.

Strictly speaking, the two toroid inductances labeled L_t may be different as they inductively couple to different objects. They are both set by the toroid size, however, so for simplicity we take them both to be

$$L_t \sim R \approx 125\ \mathrm{nH} \left(\frac{R}{10\ \mathrm{cm}}\right). \tag{2.12}$$

If the toroid is composed of N turns of wire, then C_t is given by

$$C_t \sim \frac{1}{N}\frac{2\pi R \cdot d}{g} \tag{2.13}$$

where d is the wire diameter and $g = 2\pi R/N - d$ is the spacing between wires. For fixed wire diameter, C_t and the fringe fields can be made small by taking a large N and $g \approx d$, which yields:

$$C_t \approx 10^{-2}\ \mathrm{pF} \left(\frac{d}{\mathrm{mm}}\right). \tag{2.14}$$

The use of superconducting wires allows R_t to be as small as few nΩ (the minimum RF surface resistance of type II superconductors [33]), or at worst as large as mΩ (the nominal low-temperature resistance of quenched NbTi wires [34]). We expect the resistance will be somewhat larger than nΩ, as the wires operate in the vortex state and harbor toroidal magnetic flux tubes. These tubes interact with RF currents in the wires via the so-called Magnus force [35], and their resulting motion is a significant source of dissipation [36]. The precise value of R_t will depend on the detailed geometry of the flux tubes and the surface current. We provide a rough estimate of this resistance, but stress that in what follows we consider the consequences of any R_t within the above bounds. Since the interaction of RF currents and flux tubes is of the "Lorentz" form $\vec{J} \times \vec{B}$, the resistance should scale as $\sin\theta$, the angle between the direction of flux tubes and that of the RF current. In this system, the magnetic field inducing the flux tubes is toroidal but the axion-induced current is poloidal, and so ideally $\theta = 0$. However, the flux tubes will not be perfectly toroidal: static fringe fields provide a deflection of order $\theta \sim B_f/B_0$. ABRACADABRA has measured the fringe fields outside of their toroidal magnet to be 10^{-6} of the primary field [37], which we adopt here. We assume that the deflected component of flux tubes contribute an RF resistance similar to that of trapped flux in SRF cavities, which is on the order nΩ/mG [33]. Thus we estimate:

$$R_t \approx 100\ \mathrm{n\Omega} \left(\frac{B_0}{5\ \mathrm{T}}\right)\left(\frac{\theta}{10^{-6}}\right). \tag{2.15}$$

Finally, we choose to model the cavity as a parallel RLC circuit for concreteness, with capacitance C, inductance L, resistance $\mathfrak{R}$, and thus an impedance:

$$Z_c = \left(\frac{1}{\mathfrak{R}} + \frac{1}{i\omega L} + i\omega C\right)^{-1}. \tag{2.16}$$

This cavity has natural resonance frequency $\omega_0^2 = (LC)^{-1}$ and quality factor $Q = \mathfrak{R}/\omega_0 L \gg 1$. We take $\omega_0 \sim L^{-1} \sim C^{-1} \sim 2\pi\,\mathrm{GHz}$, as set by the physical cavity size. Note that the effective shunt resistance $\mathfrak{R}$ of this cavity model is very large, proportional to the inverse of the small resistivity of the cavity walls.

All the circuit parameters have so far been estimated by physical considerations, except the pickup loop inductance L_p. This is a free parameter which we tune to optimize the signal, within reasonable limitations as discussed in Sec. 2.3.5. We assume the mutual inductance M can be made close to optimal, $M \approx \sqrt{L_p L_t}$. There is also some freedom in choosing the frequency ω sourced by the production cavity. Indeed, ω need not be exactly equal the detection cavity's natural frequency ω_0, although we require that both lie in the GHz range.

2.3.5 Optimal signal strength

The signal we are able to extract is given by the power dissipated in the detection cavity. Here we compute the maximum of this power, varying the pickup inductance and driving frequency. We use our model circuit for this, and employ the equivalent circuit shown on the right side of Fig. 2.3. This circuit is constructed such that, to lowest order in the small quantities R_t and C_t, the power dissipated in the resistor $(L_t/L_p)\mathfrak{R}$ is the same as the power dissipated in the cavity impedance Z_c. Similarly, the power dissipated in the resistor $(L_t\omega)^2/R_t$ is the same as the total power dissipated in the toroid resistors.

This can be demonstrated by making a series of transformations to sub-circuits of the circuit on the left side of Fig. 2.3, each of which preserves the input, output, and dissipated power of the transformed sub-circuit and results in a purely parallel topology. First, the leftmost transformer can be replaced by a rescaled current source $I_a M_a/L_t$ and inductor L_t. Recall that $M_a \sim L_t$, so the rescaled current is $\mathcal{O}(I_a)$. Next the elements between the transformers can be rewritten to lowest order in R_t and C_t as a resistor $(L_t\omega)^2/R_t$ and capacitor C_t. Finally, the rightmost transformer and cavity impedance can be replaced by an inductor L_t and a rescaled cavity $(L_t/L_p)Z_c$. The imaginary impedances are gathered into Z_{im}, which to lowest order in R_t and C_t is:

$$Z_{\mathrm{im}} \sim \left(\frac{2}{i\omega L_t} + i\omega C_t + \frac{1}{i\omega \frac{L_t}{L_p} L} + i\omega \frac{L_p}{L_t} C \right)^{-1} . \tag{2.17}$$

The system is on resonance when $Z_{\mathrm{im}}^{-1} = 0$. To lowest order in C_t, this occurs at the frequency

$$\omega_{\mathrm{res}} \sim \omega_0 \sqrt{1 + 2\frac{L}{L_p}}, \tag{2.18}$$

which we will choose to be our driving frequency ω. On resonance, all current in the equivalent circuit passes through the two resistors. The power dissipated in the cavity resistor is

maximized when these two resistors are equal, which occurs at a pickup loop inductance of

$$L_\star \sim L \frac{QR_t}{L_t\omega_0}. \tag{2.19}$$

An inductance L_p that is significantly less than L results in a resonance frequency that is far perturbed from the natural one. In a realistic experimental implementation, care would need to be taken to ensure that the loaded resonance frequency was not too far perturbed from the detection cavity's natural frequency, lest the quality factor degrade. As a heuristic implementation of this, we will demand that $\omega \sim \omega_0$ and thus $L_p \gtrsim L$.

We will consider the optimal signal power in two parameter regimes. First, suppose the cavity is of higher quality than the toroid, $\mathfrak{R} = Q\omega_0 L \gg 1/R_t$. Impedance matching requires $L_p = L_\star \gg L$, happily yielding a resonance frequency very close to ω_0. We then draw the *toroid-limited* power

$$P_{\max} \sim \frac{1}{8}|I_a|^2 \frac{(L_t\omega)^2}{R_t}. \tag{2.20}$$

This is the maximal power that can be extracted from the toroid as long as the driving frequency remains near ω_0. It thus depends only on the toroid properties and frequency, and notably does not scale with Q.

In the second case, suppose that the toroid is of higher quality than the cavity, $\mathfrak{R} = Q\omega_0 L \ll 1/R_t$. We would hope to again match L_p to $L_\star$, however that would require $L_p \ll L$ and we are thus prevented from impedance matching. Insisting on $L_p \gtrsim L$, the optimal choice is $L_p \sim L$ for which we draw the *cavity-limited* power

$$P_{\max} \sim \frac{1}{2}|I_a|^2 Q L_t \omega_0. \tag{2.21}$$

In general, the maximum signal power is the lesser of (2.20) and (2.21), being limited by resistive losses in the toroid or cavity, respectively:

$$P_{\text{signal}} \sim |I_a|^2(\omega L_t)\ \text{Min}\left[\frac{\omega L_t}{R_t}, Q\right] \tag{2.22}$$

The relevant toroid parameter to be compared with Q is

$$\frac{\omega L_t}{R_t} \sim 10^{10}\left(\frac{100\ \text{n}\Omega}{R_t}\right). \tag{2.23}$$

Thus for $Q \gtrsim 10^{10}$ the toroid impedance may indeed be non-negligible. The numerical similarity between Q and $\omega L_t/R_t$ reflects the fact that both arise from the small resistivity of superconductors to RF currents. This also suggests that the experimental details which affect the losses in these systems will be important in determining which of the above regimes is realized.

2.4 Sensitivity to Axion-Photon Coupling

2.4.1 Noise

The fundamental sources of noise in this system are thermal and quantum fluctuations of current in the toroid and detection cavity, as well as the intrinsic noise of the device which reads the amplified signal from the cavity. The thermal and quantum noise can be estimated from the circuit on the right side of Fig. 2.3. The equivalent resistances of both the cavity and toroid will source Johnson currents, behaving as additional parallel current sources. With L_p tuned as outlined in Sec. 2.3.5, the noise sourced by the effective cavity resistance is always greater than or equal to that sourced by the toroid resistance, so we take a noise source I_T:

$$\left\langle |I_T|^2 \right\rangle \sim 4T_{\rm sys}\frac{1}{\Re}\frac{L_p}{L_t}\,d\nu. \tag{2.24}$$

The system temperature $T_{\rm sys}$ is the sum of the thermal temperature T and the quantum noise temperature $T_{\rm QM} \sim \omega \approx 50$ mK. I_T drives fluctuations of the physical magnetic flux Φ_T inside the detection cavity,

$$|\Phi_T| = \frac{\Re}{\omega_0}\sqrt{\frac{L_t}{L_p}}\,|I_T| \tag{2.25}$$

resulting in a noise spectrum of cavity flux,

$$\begin{aligned} S_\Phi^{1/2} &\sim \left(4T_{\rm sys}\frac{QL}{\omega_0}\right)^{\frac{1}{2}} \\ &\approx \frac{\Phi_0}{\sqrt{\rm Hz}}\left(\frac{T_{\rm sys}}{0.1\ {\rm K}}\right)^{\frac{1}{2}}\left(\frac{Q}{10^{10}}\right)^{\frac{1}{2}} \end{aligned} \tag{2.26}$$

where Φ_0 is the fundamental magnetic flux quantum.

Consider coupling the small signal flux in the cavity to a low-noise read-out device, such as a SQUID magnetometer. The intrinsic flux noise in such devices is of order $10^{-6}\,\Phi_0/\sqrt{\rm Hz}$ [38], much smaller than the cavity fluctuations (2.26). We thus take (2.26) as the dominant source of noise.

2.4.2 Projected sensitivity

The noise power extracted from the cavity due to the fluctuations (2.24) is

$$P_{\rm noise} = \Re\frac{L_t}{L_p}\left\langle |I_T|^2 \right\rangle \sim 4T_{\rm sys}\,d\nu \tag{2.27}$$

and the signal-to-noise ratio (SNR) thus

$$\mathrm{SNR} \sim \frac{1}{8}|I_a|^2\,(\omega L_t)\ \mathrm{Min}\left[\frac{\omega L_t}{R_t}, Q\right]\frac{t_{\mathrm{int}}}{T_{\mathrm{sys}}} \tag{2.28}$$

where the relevant bandwidth $d\nu$ is given by the inverse of the total integration time t_{int}.

One may be concerned that tuning L_p to as outlined in Sec. 2.3.5 to maximize the power draw is not truly optimal, as the best measurement will result from maximizing the SNR. The signal and noise powers extracted from the detection cavity for a general L_p, derived from the circuit on the right side of Fig. 2.3, are

$$P_{\mathrm{signal}} \sim |I_a|^2\,\frac{(L_t\omega)^2}{R_t}\left(\frac{L_\star}{L_p}\right)\left(1+\frac{L_\star}{L_p}\right)^{-2}, \tag{2.29}$$

$$P_{\mathrm{noise}} \sim T_{\mathrm{sys}}\,d\nu\,\left(1+\frac{L_\star}{L_p}\right)^{-1}. \tag{2.30}$$

The SNR thus nominally increases with decreasing L_p, although it saturates to the intrinsic SNR of the toroid at the impedance matched $L_p = L_\star$. The optimal choice of L_p is thus either $L_\star$ or L, the same as that which draws the maximal power (2.22).

Demanding SNR > 5, the estimated reach at low axion masses $m_a \ll \omega$ is given by:

$$\begin{aligned} g > 2\cdot 10^{-11}\ \mathrm{GeV}^{-1}\cdot &\left(\frac{\omega/2\pi}{\mathrm{GHz}}\right)\left(\frac{B_0}{5\ \mathrm{T}}\right)^{-\frac{1}{2}} \\ &\left(\frac{B_{\mathrm{pc}}}{0.2\ \mathrm{T}}\right)^{-1}\left(\frac{\beta}{0.05}\right)^{-\frac{1}{2}}\left(\frac{L_t}{125\ \mathrm{nH}}\right)^{-\frac{1}{2}} \\ &\left(\frac{R_t}{100\ \mathrm{n}\Omega}\right)^{\frac{1}{4}}\left(\frac{t_{\mathrm{int}}}{\mathrm{year}}\right)^{-\frac{1}{4}}\left(\frac{T_{\mathrm{sys}}}{0.1\ \mathrm{K}}\right)^{\frac{1}{4}}. \end{aligned} \tag{2.31}$$

This is independent of the detection cavity quality factor if it is sufficiently large ($Q \geq 10^{10}$ for these parameters). The full sensitivity is show in Fig. 2.4 using:

$$\begin{aligned} &\frac{\omega}{2\pi} = \mathrm{GHz},\quad B_{\mathrm{pc}} = 0.2\ \mathrm{T},\quad B_0 = 5\ \mathrm{T} \\ &L_t = 125\ \mathrm{nH},\quad t_{\mathrm{int}} = 1\ \mathrm{year},\quad T_{\mathrm{sys}} = 0.1\ \mathrm{K}, \end{aligned}$$

and considering two cases of cavity and toroid losses:

$$\begin{aligned} &(1)\ R_t = 100\ \mathrm{n}\Omega\ \text{ and }\ Q \geq 10^{10} \\ &(2)\ R_t = \mathrm{n}\Omega\ \text{ and }\ Q \geq 10^{12}. \end{aligned}$$

We have used a form factor of $\beta = 0.05$, assuming $m_a \ll \omega$ (see Appendix A.1). The estimated sensitivity of our SRF axion design is capable of surpassing current astrophysical limits, and is comparable to the expected reach of the next generation optical experiment, ALPS II [20].

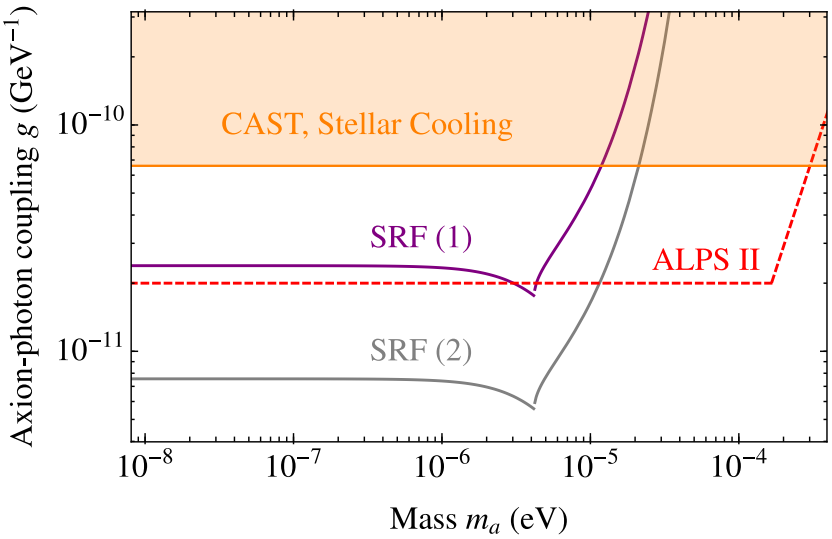

Figure 2.4: Projected sensitivity of proposed SRF LSW setup to axion-photon couplings—see text for the choices of experimental parameters. Also shown are existing solar axion (CAST) [39] and stellar cooling bounds and, for comparison, the future projected reach of the next generation optical experiment ALPS II [20].

2.5 Discussion

We have proposed a novel design for an LSW axion search leveraging SRF cavity technology and employing a region of isolated, static magnetic field. Our particular realization uses a gapped toroid, similar to that of [31, 30], to contain a static field while allowing the propagation of axion-induced signal fields. It would be interesting to consider other possible geometries for the conversion region, though the gapped toroid illustrates the necessary features. Our focus in this work is understanding the fundamental factors which set the sensitivity of such an experiment, namely the possible screening of the signal fields beyond the quasistatic limit and back-reaction from the non-negligible toroid impedance. We calculate the optimal signal strength, and for reasonable toroid parameters and SRF quality factors we find a sensitivity to axion-photon couplings in excess of astrophysical limits and comparable to complementary optical experiments. Notably, the optimal sensitivity is in fact independent of both production and detection cavity Q factors in the limit of large Q, and is instead determined by the properties of the conversion region.

We conclude with a few comments on experimental feasibility that have not yet been addressed. We have modeled the coupling of the detection cavity and axion-induced signal fields with an inductive pickup, yet a naive implementation of such a coupling would likely compromise the detection Q due to losses in the pickup wire. It is critical to explore coupling mechanisms that will not degrade Q, which is complicated by the fact that the toroid operates

on the extreme of the quasistatic regime and thus requires microwave engineering. There are other sources of noise not considered here which must be understood and managed in a practical implementation, such as stray external fields which require shielding and additional losses due to non-superconducting support materials used in the system. Finally, perhaps the biggest engineering challenge here is the necessity of frequency-matching the two SRF cavities to within $1/Q \lesssim 10^{-10}$. This demands a precise resonance monitoring and feedback mechanism to counter frequency drifts, and is a major hurdle for any photon regeneration experiment utilizing high-Q cavities, such as [40].

Chapter 3

Particle Probes with Superradiant Pulsars

We demonstrate that rotational superradiance can be efficient in millisecond pulsars. Measurements from the two fastest known pulsars PSR J1748-2446ad and PSR B1937+21 can place bounds on bosons with masses below 10^{-11} eV. The bounds are maximally good at masses corresponding to the rotation rate of the star, where scalar interactions that mediate forces $\sim 10^6$ times weaker than gravity are ruled out, exceeding existing fifth force constraints by 3 orders of magnitude. For certain neutron star equations of state, these measurements would also constrain the QCD axion with masses between 5×10^{-13} and 3×10^{-12} eV. The observed absence of pulsars above ~ 700 Hz, despite the ability of many neutron star equations of state to support frequencies well above 1 kHz, could be due to the superradiant damping of the stellar rotation as a result of its coupling to a new particle of mass $\sim 2\pi \cdot 1500$ Hz with Yukawa couplings to nucleons.

3.1 Introduction

Ultra-light bosonic particles that interact with ultra-low couplings to the standard model are an interesting target to search for new physics. Such particles emerge in a variety of contexts. They are prime dark matter candidates [41] or can act as mediators between the standard model and the dark sector. They may also emerge naturally in the context of ultra-weakly coupled gauge theories or in cosmological relaxation scenarios where the evolution of the universe can lead to ultra-light particles in a sufficiently old universe [11, 12]. Currently, the strongest reliable constraints on the existence of such particles with mass below $\sim$ eV are placed by direct laboratory searches in Cavendish experiments [42]. A more sensitive way to search for such particles was suggested in [14, 43], using the superradiance instability of black holes. It is well known that rotating black holes can lose their angular momentum through excitation of particles whose masses are close to the rotational frequency of the black hole. The authors of [14, 43] point out that the rotational frequency of extremal astrophysical

black holes can be close to the masses of interesting light particles, such as the QCD axion. Constraints on these particles can be placed through observations of rotating black holes. Alternately, gaps in the spectrum of rotating black holes can be used to discover particles whose masses correspond to that rotational frequency. Extremal, stellar mass black holes most effectively probe mass scales $\sim 10^{-9}$ eV (corresponding to rotation rates ~ 100 kHz). More recently, extremal black holes of masses $\sim 10\ M_\odot$ have been used to place superradiant constraints on lighter particles [44, 45], including masses comparable to what we will study here.

The applicability of this interesting idea is limited by difficulties in directly measuring the angular momentum of black holes [46]. The rotation rate is not directly measured - it is instead inferred either by models of the jets emerging from the black hole or through fits of the spectrum of accretion disk emissions. The superradiant instability is a strong function of the rotation rate of the black hole: while a nearly extremal black hole would have a rapid superradiant instability, a black hole that spins only $\sim$ 20 - 30 percent slower would not be significantly affected by the superradiant instability. In addition to these observational difficulties, there are also theoretical uncertainties. The calculations of [14, 43, 44, 45] assume that the geometry of the black hole is described by the Kerr solution without any matter sources just outside the event horizon. While this is a conventional assumption, it is well known that if all of the conventional assumptions about black hole physics are correct, there cannot be a solution to the black hole information problem [47]. The existence of a singular firewall just outside the horizon of the black hole is a plausible resolution to this problem [48]. Recently, it has been shown that such firewall solutions are in fact compatible with General Relativity [49]. If these firewalls exist, they can support higher order multipoles outside the black hole. In addition, they also change the boundary condition just outside the horizon. These deviations can source departures from the axisymmetric assumptions made in the calculations of [14, 43] - specifically, these departures can cause mixing between superradiant and absorptive modes, potentially dampening the growth of such modes.

It is thus interesting to ask if the superradiance instability can be effective in other astrophysical objects whose properties are better understood observationally. Superradiance as a general instability of rotating systems was discovered well before its application to the rotation of black holes [50]. The only aspect of black hole physics necessary for the existence of this instability is the absorption provided by the black hole horizon for the particle [50, 51, 52]. In this paper, we argue that these conditions can also be satisfied for another class of extremal, rotating objects, namely, millisecond pulsars. Unlike a black hole, the gravitational forces exerted by such a pulsar are not strong enough to create an absorptive region for the particle. However, such an absorptive region can be provided by non-gravitational interactions of the particle with the stellar medium.

We show that an absorptive coupling to light particles can be sufficient to slow down the rotation rates of millisecond pulsars provided the particles have masses $\sim 10^{-11}$ eV ($\sim$ kHz). Unlike black holes, millisecond pulsars are easily discovered through electromagnetic signals. Further, in contrast to measurements of black hole rotation, the frequencies of millisecond pulsars are the most precisely known numbers in astrophysics. Since the composition of the

pulsar is known, it is also possible to reliably estimate deviations from axisymmetry and show that the growth of the superradiant mode is not damped by mixing with absorptive modes. Consequently, the existence of these objects can be used to place a robust bound on particles of mass $\sim 10^{-11}$ eV that couple sufficiently strongly with the stellar medium. While the possibility of using superradiant pulsars to constrain such particles has been discussed before [53, 54, 55], only the stellar conductivity has been concretely considered as a dissipation mechanism. Perhaps more significantly, the effects of mixing with absorptive modes have not yet been carefully considered, though they are necessary to place realistic constraints.

The rest of the paper is organized as follows. In section 3.2, we review the phenomenon of superradiance and show that it is applicable to a wide variety of rotating systems. The formalism necessary to estimate the superradiance rates of particles coupled to the stellar medium is developed in section 3.3. After examining the feasibility of superradiance in real astrophysical environments, bounds on particle models are placed in section 3.4.

3.2 Superradiance

A rotating body can spin down by emitting light degrees of freedom. This radiative emission requires two conditions. First, the degrees of freedom must be light enough so that there is phase space available for the process. Second, there must be a non-zero matrix element between the rotating medium and the light degree of freedom. Consider an isolated, axisymmetric rotating object. There is phase space available for this object to spin down, for example, through the emission of a photon or other suitably light degree of freedom. The emitted particle needs to carry angular momentum away from the rotating object - in an inertial reference frame centered on the rotating body, the emitted particle will have a non-zero azimuthal angular quantum number. But, when the rotating body is axisymmetric, this particle cannot be emitted since the coupling between the rotating body and the kinematically accessible, angular momentum carrying mode vanishes due to the axisymmetry. While the leading order process is forbidden, there can be higher order processes. For example, if the rotating object has soft deformations (*e.g.* phonons), these deformations break the axisymmetry and can couple to the kinematically allowed emissive mode. Thus, the body can spin down by simultaneously producing the light degree of freedom while sourcing soft deformations on itself (which are eventually damped away through other dissipative effects). Clearly, when this process can occur in a rotating body, it will also be possible for the body to absorb the light particle when it is non-rotating: in this case, the absorption leads to deformations of the body and an increase in its angular momentum. Hence, the existence of absorption signals the possibility of superradiant emission when the emission is kinematically allowed.

This description of superradiance and its subsequent effects can be captured by the following set of equations. Consider an object that is coupled to a light degree of freedom Ψ with mass μ. The interactions of Ψ with the object will induce an absorptive term in its

equation of motion:

$$\Box\Psi + \mu^2\Psi + Cv^\alpha\nabla_\alpha\Psi + V_{eff}\left(\Psi\right) = 0 \tag{3.1}$$

where C is the absorption coefficient, v^α the four velocity of the system and $V_{eff}\left(\Psi\right)$ is any other potential that dictates the motion of Ψ. This expression is the covariant generalization of the familiar equation for absorption in the rest frame of the system

$$\Box\Psi + \mu^2\Psi + C\dot{\Psi} + V_{eff}\left(\Psi\right) = 0 \tag{3.2}$$

since in the rest frame $v^\alpha = (1, 0, 0, 0)$, were we assume C has at most a weak dependence on v^α. Owing to absorption, an initial amplitude of Ψ exposed to this system will decay exponentially as $e^{-\frac{C}{2}t}$.

Let the system rotate with frequency Ω. Choose spherical coordinates (t, r, θ, ϕ) centered around the axis of rotation. In these coordinates, $v^\alpha = (1, 0, 0, \Omega\, r\sin\theta) + \mathcal{O}\left((\Omega r)^2\right)$. Now, consider the equation of motion for a specific angular momentum mode of Ψ. These are of the form $\tilde{\Psi}\left(r, \theta\right) e^{-iEt}e^{im\phi}$ where E is the energy and m the azimuthal angular quantum number of the mode. For a non-relativistic mode, the energy E is dominated by the rest mass μ of the particle. The equation of motion of this mode takes the form

$$\left(\Box + \mu^2\right)\tilde{\Psi}\left(r, \theta\right) - iC\left(\mu - m\,\Omega\right)\tilde{\Psi}\left(r, \theta\right) + V_{eff}\left(\Psi\right)e^{i\mu t}e^{-im\phi} = 0 \tag{3.3}$$

In this equation, for sufficiently large $m\,\Omega$, $\mu - m\,\Omega < 0$ and the term $C\left(\mu - m\,\Omega\right)$ flips sign. This converts the absorptive term into an emissive term leading to exponential growth $\propto e^{\frac{C}{2}t}$ of Ψ. This exponential growth is indicative of emission of Ψ by the system, leading to energy loss from the system through decay of its rotational energy.

Superradiance is thus a general instability of rotating systems that leads to the decay of the rotational energy in the system. In the next section, we will show that this instability can be very efficient in compact, rapidly rotating systems such as neutron stars if the stellar medium couples to light particles whose masses are order the rotation rate Ω of the star.

3.3 Superradiance in Neutron Stars

Superradiance results in the conversion of rotational kinetic energy into excitations of certain angular momentum modes of particles coupled to the rotating medium. The rate of superradiance is governed by equation (3.3), where the superradiant term appears in the same form as an absorptive term, but has the opposite sign. Consequently, much like absorption, the rate of superradiance is proportional to the occupation number of the concerned mode. In this way, superradiance can be thought of as a form of stimulated emission. The amplitude of a bosonic superradiant mode will grow at a rate proportional to its occupation number, resulting in exponential amplification of the mode. This exponential increase in the amplitude will lead to exponential energy loss from the rotating system. On the other hand,

a superradiant fermionic mode will not lead to such an exponential energy loss since Pauli exclusion leads to the saturation of the mode's amplitude once it acquires one particle, thereafter shutting off the superradiant channel. This exponential growth occurs in the region where the mode overlaps with the rotating medium. It is only in this region that equation (3.3) describes the equation of motion of the mode. The efficiency of superradiant energy loss thus depends strongly on the overlap between the rotating medium and the superradiant mode.

The rotational angular momentum modes of a light bosonic particle bound gravitationally to a spinning neutron star satisfy the characteristics discussed in the above paragraphs to act as an efficient superradiant conduit (see Figure 3.1). These modes are solutions to equation (3.3) where the potential V_{eff} is given by the gravitational interaction energy between the star and the bound particle. The non-relativistic limit of this equation is obtained by decomposing the field Ψ in the form $e^{-i\mu t}\psi_{nlm}(t, r, \theta, \phi)$ and dropping time derivates of order $\frac{\dot{\psi}_{nlm}}{\mu}$ and higher, yielding

$$i\dot{\psi}_{nlm} = -\frac{1}{2\mu}\left(\nabla^2\psi_{nlm}\right) - \frac{G\,M\,\mu}{r}\psi_{nlm} + i\frac{C\,(\mu - m\,\Omega)}{2\,\mu}\psi_{nlm} \tag{3.4}$$

Without the absorptive term $\propto C$ on the right-hand side, equation (3.4) is the Schrodinger equation describing a mode ψ_{nlm} with radial quantum number n, total angular momentum l and azimuthal angular momentum m, moving in the gravitational potential of a star of mass M. Assuming the star to be spherically symmetric (we will discuss the effects of deviations away from spherical and axisymmetry in section 3.4.1), the modes ψ are the usual Hydrogenic wavefunctions with real eigenenergies that correspond to the bound state energy. These modes are localized around the "Bohr" radius $\sim \frac{n^2}{\alpha_g\,\mu}$ where the gravitational "fine structure" constant $\alpha_g = GM\mu$ (see Figure 3.1).

The absorptive term in (3.4) is of course non-Hermitian and leads to these modes developing imaginary eigenenergies, indicating growth or decay of the mode. To estimate this imaginary part, note that the absorptive term is non-zero only in the interior of the star. For physically relevant neutron stars, it will turn out that the mass of the particles that can undergo superradiance are such that the Bohr radius of the mode is much bigger than the radius R of the star. The absorptive term only affects a small part of the wavefunction and its effects can be estimated using perturbation theory. The imaginary part of the energy shift caused by this perturbation is

$$\frac{\Gamma_{nlm}}{2} = \langle\psi_{nlm}|\frac{C}{2}\frac{(\mu - m\,\Omega)}{\mu}|\psi_{nlm}\rangle \equiv \frac{C_{nlm}}{2}\frac{(\mu - m\,\Omega)}{\mu} \tag{3.5}$$

Physically, this corresponds to the expectation that the mode can only grow/decay inside the star and hence the growth rate is proportional to the probability of finding the particle in that region (see Figure 3.1). For $\mu > m\,\Omega$, the imaginary part is positive, leading to absorption and exponential damping of the mode. When $\mu < m\,\Omega$, the imaginary part is negative, leading to emission and exponential amplification of the mode. In both cases, the rate of absorption/emission is given by (3.5).

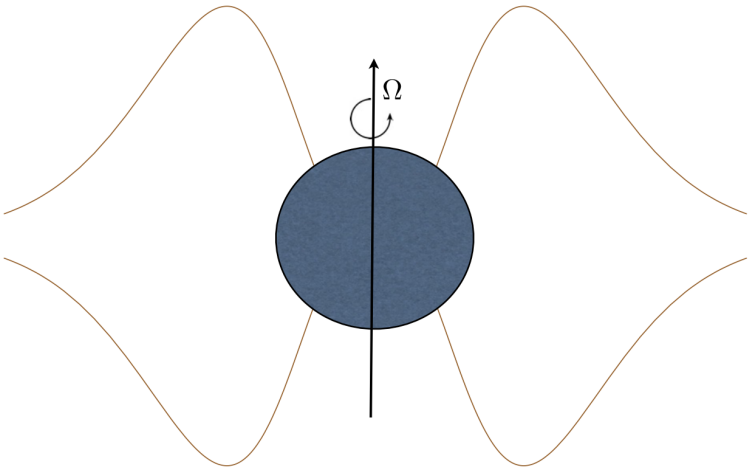

Figure 3.1: A state with non-zero azimuthal angular momentum bound gravitationally to a neutron star. The star spins with frequency Ω. Superradiant growth occurs in the region where the mode overlaps with the star.

Using the rate (3.5), it is easy to see that efficient superradiance requires two conditions. First, equation (3.5) is a strong function of the size R of the star since the probability of finding the particle within the star depends upon its size. This size is however limited by the rotational frequency Ω of the star, since relativistic considerations require that $\Omega R < 1$. Consequently, superradiance is most efficient in objects that are close to satisfying this bound. Second, equation (3.5) is also a strong function of the angular momentum m required to achieve the superradiance condition. This is because modes with high angular momentum are localized away from the star, leading to a suppressed probability of finding the particle inside the star. Consequently, superradiance is most effective when the mass of the particle μ is close to Ω. In this case, the superradiance condition $\mu - m\,\Omega < 0$ will be satisfied by low angular momentum modes $m \cong 1$. When $\mu \gg \Omega$, the superradiance condition will only be satisfied by modes with very high angular momentum. But, these modes are at Bohr radii ($\propto n^2 \gtrsim m^2$) far from the star leading to a highly suppressed overlap with the star and hence a suppressed superradiance rate. Similarly, when $\mu \ll \Omega$, even though the superradiance condition is satisfied by many low lying modes, the Bohr radius of the mode ($\propto \mu^{-2}$) is also far from the star leading to suppressed overlap.

These considerations suggest that superradiance could be efficient in millisecond pulsars, due to the large angular momentum. A typical millisecond pulsar has a radius $R \sim 10 - 15$ km, with rotational frequency $\Omega \sim 2\pi(1\,\text{kHz})$, close to saturating the extremality bound $\Omega R < 1$. The very existence of such pulsars should constrain the existence of particles with masses $\mu \sim \Omega \sim 10^{-11}$ eV that couple sufficiently strongly to the stellar medium. We pursue

this question in the rest of the paper, starting with section 3.3.1 where we estimate the superradiance rate for particles that are coupled to the stellar medium.

3.3.1 Rate

In this section, we estimate the superradiance rate (3.5) for the states $|\psi_{nlm}\rangle$ of a scalar field Ψ that are bound gravitationally to a neutron star. This rate, up to the kinematic ratios in (3.5), is the absorption rate C_{nlm} of the mode $|\psi_{nlm}\rangle$ in the stellar medium when the medium is at rest. Energy and angular momentum have to be conserved in this absorption process. This requires the excitation of inelastic degrees of freedom in the stellar medium, in addition to energy and angular momentum being transferred to the bulk stellar rotation. The energies of these inelastic degrees of freedom have to be comparable to the energy of $|\psi_{nlm}\rangle$ and are therefore $\sim \Omega$. In the stellar medium, these light degrees of freedom can be phonon modes of the neutrons or other low frequency oscillations, for instance. For simplicity, we will compute the superradiant emission of Ψ when it has scalar interactions with the stellar medium.

3.3.1.1 Scalar Absorption Rate

We now turn to the main operator of interest for this paper, the neutron Yukawa interaction

$$\epsilon \, \Psi \, \overline{n} \, n. \tag{3.6}$$

We may use this to probe any new ultralight scalar or CP-violating pseudoscalar. Depending on the neutron star equation of state, this may even include the QCD axion: many neutron star equation of states predict a pseudoscalar condensate in the star, throughout $\mathcal{O}(1)$ of the star's mass [56]. In this phase we expect $\theta_{\text{eff}} \sim 1$, in which case the QCD axion obtains a neutron coupling $\epsilon \sim \theta_{\text{eff}} \, m_n / f_a \sim m_n / f_a$, which is large enough to probe new regions of parameter space.

In order to estimate the scalar-phonon conversion rate, we begin with 1D toy model which we believe captures the essence of the process, and extrapolate to 3D at the end. Take a string of N neutrons spread over a length R. The absorption of Ψ results in phonon excitations of the string. Let us enumerate these phonon excitations $|k\rangle$. The string consists of N neutrons and we assume that these neutrons have nearest neighbor interactions. Since we ultimately want to model a neutron star, we will take the string to contain a nuclear density of neutrons with the strength of nearest neighbor couplings set by the QCD scale. For small displacements, these nearest neighbor interactions will be harmonic and the states $|k\rangle$ correspond to phonon excitations of the string. The neutrons and the Ψ particles are non-relativistic throughout this process and are modelled with the non-relativistic "free" hamiltonian (*i.e.* neglecting (3.6)):

$$H_F = \frac{p_\Psi^2}{2\,\mu} + \sum_{j=1}^{N} \frac{p_j^2}{2\,m_n} + \frac{1}{2} m_n \omega^2 \left(\delta x_j - \delta x_{j-1}\right)^2 \tag{3.7}$$

where δx_j is the displacement from the equillibrium position x_j^0 of the j^{th} neutron, p_j the corresponding conjugate momemtum, m_n the mass of the neutron, $\omega \sim \Lambda_{QCD}$ the strength of the nearest neighbor interaction and p_Ψ the conjugate momentum of Ψ.

The Hamiltonian (3.7) can be diagonalized through a coordinate transformation given by

$$\delta x_j = \sum_{s=1}^{N} y_{js} Y_s \tag{3.8}$$

where y_{js} are the normalized wavefunctions, after which the Hamiltonian becomes

$$H_F = \frac{p_\Psi^2}{2\,\mu} + \sum_{j=1}^{N} \frac{|q_j|^2}{2\,m_n} + \frac{1}{2} m_n \omega_j^2 |Y_j|^2 \tag{3.9}$$

where q_j are the conjugate momenta of the coordinates Y_j and the frequencies $\omega_j \sim \frac{j}{N}\,\omega$. (This becomes $\omega_j \sim \frac{j}{N^{1/3}}\,\omega$ for a 3D system, though in practice we use measured values of the phonon frequencies rather than this estimate.) The normalized wavefunctions are given approximately by $y_{js} \sim N^{-1/2} \exp(i2\pi js/N)$. Notice the normalization suppression by $\sqrt{N}$ due to the participation by all N neutrons in the oscillation. In terms of the new phonon coordinates Y_j and these wave functions y_{js}, the position x_j of the j^{th} neutron is given by

$$x_j = x_j^0 + \delta x_j = x_j^0 + \sum_{s=1}^{N} y_{js} Y_s \tag{3.10}$$

The Hamiltonian (3.9) describes N free harmonic oscillators with frequencies between $\frac{\omega}{N}$ and ω. These correspond to sound waves (phonons) in the one dimensional string of neutrons, with quantized frequencies. (Note we will be neglecting the $\omega = 0$ translational mode, since dissipation via that mode is insignificant and it does not otherwise affect our calculation.) The quantization unit for the frequencies is set by the number of neutrons in the string. In the one dimensional example, this number is directly proportional to the length R of the string, resulting in quantization set by the physical size of the system as one might expect for a sound wave. The eigenstates $|k\rangle$ of this system are given by $\prod_{s=1}^{N} |k_s\rangle$ where $|k_s\rangle$ is an eigenstate of the free harmonic oscillator with frequency ω_s and occupation number k_s.

We now have a description of the string. Before proceeding with the computation of the absorption coefficient, we must also model the interaction of the scalar field Ψ with the neutrons. The perturbation (3.6) caused by Ψ is a shift to the mass of the neutron. The resulting total hamiltonian that also includes these interactions is

$$H = H_F + \epsilon \sum_{j=1}^{N} \Psi\left(x_j\right) \tag{3.11}$$

We will represent Ψ in terms of its creation and annihilation operators (a_Ψ and $a_\Psi^\dagger$ respectively). This is necessary since absorption requires operators that can destroy particle number. In this representation, Ψ is given by

$$\Psi\left(x_j\right) = \int \frac{dp}{(2\pi)} \frac{1}{\sqrt{2E_p}} \left(a_{\Psi,p}^\dagger e^{-ipx_j} \; + \; a_{\Psi,p} e^{ipx_j}\right) \tag{3.12}$$

where E_p is the energy of the state of momentum p. The Ψ particles absorbed by the string of neutrons are also non-relativistic and hence $E_p \sim \mu$.

The above states are the eigenstates in the free theory. Of course, we need these states in the full interacting theory. These can be calculated using the Lippmann-Schwinger equation,

$$|k, \psi_{nlm}\rangle_{\text{int}} = \left(1 + G_+ \epsilon \sum_{j=1}^{N} \Psi\left(x_j\right) + G_+ \left(\epsilon \sum_{j=1}^{N} \Psi\left(x_j\right)\right) G_+ \left(\epsilon \sum_{l=1}^{N} \Psi\left(x_l\right)\right) + \ldots\right) |k, \psi_{nlm}\rangle \tag{3.13}$$

where G_+ is the retarded Green's function of the free phonon Hamiltonian H_F with energy E equal to the total initial energy of the system. Formally, G_+ is obtained by inverting $E - H_F$. Using these states and a form of the optical theorem, the absorption rate is

$$C_{nlm} = \text{Im}\left(\langle k, \psi_{nlm}| \left(\left(\epsilon \sum_{j=1}^{N} \Psi\left(x_j\right)\right) + \left(\epsilon \sum_{j=1}^{N} \Psi\left(x_j\right)\right) G_+ \left(\epsilon \sum_{l=1}^{N} \Psi\left(x_l\right)\right) + \ldots\right) |k, \psi_{nlm}\rangle\right) \tag{3.14}$$

The second term in (3.14) is the lowest order (in ϵ) term that can give rise to imaginary coefficients. This term allows for absorption of Ψ and excitation of phonons, followed by propagation of the excited phonon states and then subsequent re-emission of Ψ and de-excitation of phonons. The Green's function G_+ develops poles from the propagation of the on-shell, excited phonon states. These poles are of course regulated by the width Γ of the intermediate states, yielding imaginary coefficients.

More concretely, the imaginary part is

$$C_{nlm} = \text{Im}\left(\langle k, \psi_{nlm}| \left(\epsilon \sum_{j=1}^{N} \Psi\left(x_j\right)\right) G_+ \left(\epsilon \sum_{l=1}^{N} \Psi\left(x_l\right)\right) |k, \psi_{nlm}\rangle\right) + \mathcal{O}\left(\epsilon^3\right) \tag{3.15}$$

Inserting a complete set of intermediate phonon states $\sum_{k'} |k'\rangle\langle k'|$ into (3.15), we get

$$\langle k, \psi_{nlm}| \left(\epsilon \sum_{j=1}^{N} \Psi\left(x_j\right)\right) \sum_{k'} |k'\rangle\langle k'| G_+ \sum_{k''} |k''\rangle\langle k''| \left(\epsilon \sum_{l=1}^{N} \Psi\left(x_l\right)\right) |k, \psi_{nlm}\rangle \tag{3.16}$$

The propagator $\langle k'|G_+|k''\rangle$ of the intermediate phonon states in (3.16) is obtained by inverting the free phonon hamiltonian $E - H_F$ and is

$$\langle k'|G_+|k''\rangle = \frac{\delta_{k'k''}}{E - E_{k'} + i\,\Gamma_{k'}} \tag{3.17}$$

The parameters $E_{k'}$ and $\Gamma_{k'}$ in this expression are of course the energy and decay rate of the state $|k'\rangle$. Using (3.17), (3.16) is equal to

$$\sum_{k'} \langle k, \psi_{nlm}| \left(\epsilon \sum_{j=1}^{N} \Psi\left(x_j\right) \right) |k'\rangle \frac{1}{E - E_{k'} + i\,\Gamma_{k'}} \langle k'| \left(\epsilon \sum_{l=1}^{N} \Psi\left(x_l\right) \right) |k, \psi_{nlm}\rangle \tag{3.18}$$

The next task is to compute the transition elements in (3.18) that lead to the excitation of phonon modes. In the problem of interest, Ψ is a light field, with $\mu \lesssim \omega_1$. We expect the dominant contribution to the transition element is the excitation of the lowest phonon states while leaving the other states unperturbed. $|k'\rangle$ is therefore of the form $|k_1 + 1\rangle \otimes \prod_{s=2}^{N} |k_s\rangle$, and so we only need the one-phonon contribution from the interaction potential. Taylor expanding the scalar operator to first order about the neutron equilibrium positions, we find

$$\epsilon \sum_{j=1}^{N} \Psi\left(x_j\right) \approx \epsilon \sum_{j=1}^{N} \left(\Psi(x_j^0) + \left.\frac{\partial \Psi}{\partial x}\right|_{x_j^0} \delta x_j \right) \tag{3.19}$$

The first term cannot excite phonons, and does not contribute to the absorption rate. The second term is the desired one-phonon contribution. The action of the scalar operator on the bound states $|\psi_{nlm}\rangle$ yields

$$\langle 0| \frac{\partial \Psi}{\partial x} |\psi_{nlm}\rangle = \frac{1}{\sqrt{2\mu}} \frac{\partial \psi_{nlm}}{\partial x} \tag{3.20}$$

where $|0\rangle$ is the vacuum state and $\psi_{nlm}(x)$ is the spatial wavefunction of $|\psi_{nlm}\rangle$ at x.

Using (3.19) and (3.20) in (3.18), we have

$$\langle k'| \Psi\left(x_l\right) |k, \psi_{nlm}\rangle \approx \langle k'| \frac{1}{\sqrt{2\mu}} \left.\frac{\partial \psi_{nlm}}{\partial x}\right|_{x_l^0} \delta x_l\, |k\rangle \tag{3.21}$$

To evaluate (3.21), we express δx_l in terms of the phonon creation and annihilation operators. Recalling (3.10), this is

$$\delta x_l = \sum_{s=1}^{N} \frac{y_{ls}}{\sqrt{m_n \omega_s}} (a_s^\dagger + a_s) \tag{3.22}$$

Inserting this and recalling that $|k'\rangle = |k_1 + 1\rangle \otimes \prod_{s=2}^{N} |k_s\rangle$, the matrix element evaluates to

$$\langle k'| \left(\epsilon \sum_{l=1}^{N} \Psi\left(x_l\right) \right) |k, \psi_{nlm}\rangle \approx \sum_{l=1}^{N} \frac{1}{\sqrt{2\mu}} \left.\frac{\partial \psi_{nlm}}{\partial x}\right|_{x_l^0} \frac{y_{l1}}{\sqrt{m_n \omega_1}} \sqrt{k_1 + 1} \tag{3.23}$$

where k_1 is the occupation number of the lowest phonon mode with frequency ω_1. Suppose the string of neutrons is in equillibrium with a system that has temperature T (in a neutron

star, the neutrons are in equllibrium with a gas of electrons in the star, whose temperature ranges between 10^5 K - 10^9 K). The occupation number k_s of a mode with frequency ω_s is

$$k_s = \frac{T}{\omega_s} \gg 1 \tag{3.24}$$

For simplicity, let us also convert the sum over the neutron positions in (3.23) with an integral over a neutron number density $n(x) \sim N/R$ performed over the stellar medium. With these substitutions and a little rearranging, (3.23) becomes

$$\langle k'| \left(\epsilon \sum_{l=1}^{N} \Psi\left(x_l\right) \right) |k, \psi_{nlm}\rangle \approx \frac{\epsilon}{\sqrt{2\mu}} \sqrt{\frac{T}{\omega_1}} \frac{1}{\sqrt{2m_n\omega_1}} \int_S dx\, n(x) \frac{\partial \psi_{nlm}}{\partial x}\, y_1(x) \tag{3.25}$$

where $y_1(x)$ is the $s = 1$ wavefunction y_{1l} written as a function of neutron position x instead of neutron index l. With (3.25), we have evaluated the inner products in (3.18). Substituting these results into (3.15), we get the absorption rate

$$C_{nlm} \sim \frac{\epsilon^2}{2\mu} \left(\frac{T/\omega_1}{2m_n\omega_1} \right) \left| \int_S dx\, n(x) \frac{\partial \psi_{nlm}}{\partial x}\, y_1(x) \right|^2 \left(\frac{\Gamma_1}{(\mu - \omega_1)^2} \right) \tag{3.26}$$

The integral in the above expression is of course performed only inside the star (of size R).

We now generalize the above computation to three dimensions. In three dimensions, the interaction $\epsilon\, \Psi\, \overline{n}\, n$ can excite phonons in all three directions. The small oscillations of the neutrons about their equillibrium positions can still be diagonalized through transformations similar to (3.10), where N is now the total number of neutrons in the object. The rest of the calculation goes forward as described in the above paragraphs, with the result

$$C_{nlm} \sim \frac{\epsilon^2}{2\mu} \left(\frac{T/\omega_1}{2m_n\omega_1} \right) \left| \int_S d^3\mathbf{r}\, n(\mathbf{r}) \nabla \psi_{nlm} \cdot \mathbf{y}_1(\mathbf{r}) \right|^2 \left(\frac{\Gamma_1}{(\mu - \omega_1)^2} \right) \tag{3.27}$$

$$\sim \frac{\epsilon^2}{2\mu} \left(\frac{T/\omega_1}{2m_n\omega_1} \right) \left| \int_0^R r^2 dr\, n(r) \frac{\partial \psi_{nl}}{\partial r} y_1(r) \right|^2 \left(\frac{\Gamma_1}{(\mu - \omega_1)^2} \right) \tag{3.28}$$

where the integration is performed inside the star, and in the second step we have estimated the factors in the integral (defining $\psi_{nl}(r) = \psi_{nlm}/Y_{lm}$) for calculational simplicity. This assumes that the phonon wavefunction has the same angular structure as the scalar field, e.g., an $l = m = 2$ scalar excites an $l = m = 2$ phonon. Otherwise, the integral in (3.27) vanishes for a spherical star. (We discuss the impact of deviations from spherical symmetry in Section 3.4.1.)

The integral in (3.27) also vanishes if the scalar force $\nabla\psi_{nlm}$ is constant. In order to excite a phonon mode in the star, the gradient of the scalar field must change over the extent of the star—a constant force only shifts the center of mass of the star. This condition is satisfied even at lowest order for scalars with $l \neq 1$, and so (3.28) is a good approximation. But we must be more careful with the case $l = 1$. In this case $\nabla\psi_{nlm}$ = constant at

lowest order in r/a_0, where $a_0 \gg R$ is the Bohr radius. We must therefore turn to the second-order term for the leading contribution to C_{nlm}. This is equivalent to making the substitution $\partial\psi_{nl}/\partial r \to (r/a_0)(\psi_{nl}/\partial r)$ in equation (3.28) when $l = 1$, and leads to an additional $\sim (R/a_0)^2$ suppression in C_{nlm}. As a result, constraints due to superradiance of the ψ_{211} mode will not be stronger than the constraints due to ψ_{322}, despite the larger overlap with the star.

For the normalized phonon wavefunctions we approximate $y_1(r) = \sqrt{4\pi}e^{i\pi r/R}/\sqrt{N}$ for $l = 1$, since the lowest frequency dipole phonon mode has a single node in the star and non-zero displacement at the center. For $l = 2$ phonons (and also $l = 0$, which will become relevant for mixing in Section 3.4.1), we use $y_1(r) = \sqrt{20\pi/3}(r/R)e^{i\pi r/(4R)}/\sqrt{N}$, since these lowest-frequency modes have vanishing displacement at the center and no nodes. These approximate forms do not substantially impact the results, but we introduce them nevertheless to describe the phonon modes we are coupling to. Also, for simplicity, we treat the star as a sphere of uniform density.

For the hydrogenic wavefunctions ψ_{nlm} (with $l > 1$, for instance), the integral in (3.28) scales as

$$C_{nlm} \propto \left| R^3 \cdot \frac{N}{R^3} \cdot \frac{R^{l-1}}{a_0^{l+3/2}} \cdot \frac{e^{i2\pi r/R}}{\sqrt{N}} \right|^2 \sim NR^{-5} \left(\frac{R}{a_0}\right)^{2l+3} \tag{3.29}$$

For masses μ much bigger than the rotation rate Ω of the star, the superradiant modes require large l. In this case, the high power of l in the overlap with the star suppresses the superradiance rate. For μ much smaller than R^{-1}, even though the lowest modes are superradiant, the Bohr radius of the orbit $a_0 = (GM\mu^2)^{-1}$ is big, leading to a suppression of the rate. Consequently, as anticipiated in section 3.3, superradiance is maximally effective when $\mu \sim \Omega \sim R^{-1}$.

The above estimate captures the parameter behavior of the absorption rate. There are three sources of possible $\mathcal{O}(1)$ deviations between this estimate and the true answer. First, we have not attempted to specify the neutron star equation of state, or to construct the detailed phonon wavefunctions that describe the three dimensional oscillations. This will not affect the parametric dependence (such as the functional dependence on the fourier momentum) of the transition elements, but could give rise to different $\mathcal{O}(1)$ coefficients for the transition elements. Second, the inner product (3.25) involves integration over angular coordinates in the stellar medium. These integrals enforce conservation of angular momentum. They evaluate to zero for forbidden transitions and give rise to order one coefficients for the allowed transitions. We will not explicitly evaluate these integrals, but instead set them equal to 1 for the allowed transitions by approximating (3.27) as (3.28). And third, the true absorption rate may have mild dependence on the rotation rate Ω that we have neglected in this non-rotating calculation, as the stellar medium, oscillation modes, and damping rates are affected by the rotation. Because of these approximations, there may be $\mathcal{O}(1)$ uncertainties in our absorption rate calculation. However, these $\mathcal{O}(1)$ differences do not significantly change our constraints on the coupling ϵ, since the bound on ϵ depends on the square root of the absorption rate (see Section 3.4).

Before continuing, let us consider the decay width Γ_1 of the phonon mode that allows for absorption of the scalar. The low-frequency phonon modes decay primarily by gravitational radiation, the effects of viscosity being very small by comparison [57]. We discuss these damping rates further for the phonon modes of interest in Section 3.4.2. We can crudely estimate the decay rates as a ratio of the radiated power to the phonon kinetic energy, for instance as

$$\Gamma_1 = \frac{\frac{1}{5}G(MR\,\delta R_{\rm ph})^2\omega_1^6}{\frac{1}{2}M(\delta R_{\rm ph}\,\omega_1)^2} \sim GMR^2\omega_1^4 \tag{3.30}$$

for the quadrupolar phonons, where $\delta R_{\rm ph}$ is the typical displacement of neutrons in the phonon oscillation. Notice that Γ_1 contains an additional factor of $M \propto N$, so that we may rewrite $C_{nlm} \propto N^2$ and interpret it as a coherent scattering of scalars into gravitons. For large values of the coupling ϵ, scalar radiation may overtake gravitational radiation as the dominant damping mechanism. We have little interest in couplings this large, however, and so we neglect this effect.

3.4 Constraints

The absorption coefficients computed in section 3.3.1 can be used to predict the spin down rate of neutron stars. The existence of rapidly rotating pulsars such as PSR J1748-2446ad [58] and PSR B1937+21 [59] can be used to place limits on particles whose existence would have prevented these pulsars from spinning at the observed rates. However, before placing bounds on such particles we first investigate the stability of the superradiant mode. Superradiance can be effective only if there is continuous accumulation of particles into the mode leading to exponential amplification of the mode. If the mode is depleted through some other absorptive process, it will no longer undergo exponential amplification and will not efficiently remove angular momentum from the rotating system. These aspects are discussed in section 3.4.1, where we examine the superradiant instability in realistic astrophysical environments. Following this discussion, we place bounds on possible scalar couplings to neutrons in section 3.4.2.

3.4.1 Mode Stability

The modes described by equation (3.4) describe an ideal neutron star with a spherically symmetric mass distribution and an absorption coefficient C that is time independent and constant inside the star. In this ideal world, these modes are eigenfunctions of the Hamiltonian and their growth rate is completely governed by (3.5). However, real neutron stars do not satisfy these conditions. Departures from these symmetries leads to mixing between various modes. In particular, there will be mixing between superradiant and absorptive modes, leading to damping of the superradiant growth. If these mixing terms are appreciable, superradiance will not have a significant impact on the rotational angular momentum of the system.

In the section, we will first describe and develop a formalism to estimate mixing. We will then consider the mixing effects from the free precession of the star, the equatorial bulge in the star caused by rapid rotation, stellar quakes, and tidal disruptions of the system due to companion objects around the pulsar. We estimate the maximum possible mixing that can be produced in realistic astrophysical situations. This is then incorporated into the parameter space of particle physics models probed by superradiance in Section 3.4.2.

3.4.1.1 Overview and Formalism

The superradiant modes have different azimuthal angular momentum than the absorptive modes. They are therefore mixed together by non-axisymmetric perturbations of the star. Scalars couple to the neutron density and are perturbed by the asymmetries in the mass distribution of the star. Gravitational asymmetries can also cause mixing between modes. These can arise either as a result of asymmetries in the mass distribution of the star or from the presence of companions to the pulsar.

How large a mixing δ can we tolerate between a superradiant mode (say $\psi_{l+1,ll}$) and an absorptive mode (say $\psi_{n'l'm'}$)? In the presence of this mixing, the physical mode around the star is the linear combination $|\psi_{l+1,ll}\rangle + \delta|\psi_{n'l'm'}\rangle$. The occupation number of this mode changes at a rate $\sim \Gamma_{l+1,ll} + \delta^2\Gamma_{n'l'm'}$. The mode will grow if this rate is positive, requiring

$$\delta^2 \lesssim -\frac{\Gamma_{l+1,ll}}{\Gamma_{n'l'm'}} \sim \frac{C_{l+1,ll}}{C_{n'l'm'}} \tag{3.31}$$

where in the last equality we dropped the kinematic factors that relate the absorption/ superradiance rate Γ to the non-rotating absorption rate C, except for the critical difference in sign.

The most stringent demands on these mixing terms are between that of the superradiant mode $\psi_{l+1,ll}$ and the absorptive modes ψ_{n00}, when non-axisymmetries are present to mix those modes. This is due to the fact that the absorption rates Γ_{nlm} are strong functions of the overlap of the mode with the star (see equation (3.28)). The modes $\psi_{l+1,ll}$ carry angular momentum and are localized away from the origin leading to a suppressed overlap with the star. On the other hand, the modes ψ_{n00} do not carry angular momentum and have support at the origin leading to an enhanced absorption rate Γ_{n00}. Consequently, the superradiance growth condition (3.31) is the hardest to satisfy for these mixings.

For this paper we restrict our interest to the largest superradiant modes ψ_{211} and ψ_{322}, so in this section we will only care to calculate effects that might cause a superradiant mode to mix with absorptive modes that have $l \leq 2$. Any modes with higher angular momentum will have a suppressed overlap with the star that would cause them to be absorbed slower than ψ_{211} or ψ_{322} would be superradiantly emitted, even with $\mathcal{O}(1)$ mixing. We will see below that the allowed mixings are determined by the multipoles of the asymmetries in the system and the usual selection rules. For instance, in order mix $|\psi_{l+1,ll}\rangle$ into $|\psi_{n00}\rangle$, the system must have a $Y_{l,-l}$ asymmetry. As a result, we may neglect any effects that cannot produce a dipole

or quadrupole perturbation to the system, since any higher order perturbations cannot cause mixing of ψ_{211} or ψ_{322} with a low angular momentum $l \leq 2$ absorptive mode.

In addition to the damping mechanisms introduced by the astrophysical environment, it is theoretically possible that once the particle mode grows, the number density in the mode may become significant enough to cause self interactions that may damp the growth of the mode. Instabilities of this kind were considered in [14, 43] and were not found to be a problem for similar superradiant growth around rotating black hole systems. This is not a surprise since the particles of interest have extremely weak self interaction couplings (such as the QCD axion). This then clears the way to placing limits on various particle physics models in Section 3.4.2.

Before we proceed on to specific sources of mixing, let us briefly develop the general formalism that will provide us with the mixing magnitudes δ. Any non-axisymmetries in the neutron density or gravitational fields will appear as perturbations $H' \propto e^{-i\omega' t}$ to the scalar Hamiltonian, and their effect on the Schrodinger equation (3.4) can be estimated using time-dependent perturbation theory. The mixing between initial state $|i\rangle$ and final state $|f\rangle$ with energy difference $\Delta\omega$ is then

$$\delta^2 \sim \frac{|\langle f|\, H' \,|i\rangle|^2}{(\omega' - \Delta\omega)^2} \tag{3.32}$$

Any gravitational 2^l-pole perturbation can be captured by the appropriate multipole of the gravitational field:

$$H'_{\text{grav}} = -G\mu \frac{r_i p_i}{r^3} - \frac{G\mu}{2} \frac{r_i r_j Q_{ij}}{r^5} - \cdots \tag{3.33}$$

where p_i and Q_{ij} are the dipole and quadrupole moments of the system, respectively. The pulsar will not have a gravitational dipole of its own, since that would simply correspond to a center of mass displacement, but a dipole gravitational potential can arise from the effects of a binary companion.

To account for mixing due to scalars scattering off neutrons in a non-axisymmetric pulsar, we may perform a calculation very similar to the absorption calculation earlier, this time investigating the real part of the second-order term. In this case, however, we are interested in the elastic scattering process where a scalar ψ is absorbed into a phonon mode, and then re-emitted into a different scalar mode ψ'. In a spherically symmetric star, a phonon with wavefunction $y \propto Y_{lm}$ only couples to scalars with $\psi \propto Y_{lm}$. In the presence of a density asymmetry $\delta n\, Y_{LM}$, however, that same phonon can also couple to $\psi' \propto Y_{l\pm L, m+M}$. Let us parameterize the density asymmetry by the amplitude δR of the perturbation, such that $\delta n \sim (\delta R/R)\, n$, where n is the average neutron density in the star. Then we can approximate

the mixing between scalar modes ψ and ψ' due to some appropriate asymmetry by inserting

$$\langle f|\, H'_{\rm scat}\, |i\rangle \sim \frac{\epsilon^2}{2\mu}\left(\frac{T/\omega_1}{2m_n\omega_1}\right)\left(\frac{\delta R}{R}\right)\left(\int_0^R r^2 dr\, n(r)\frac{\partial\psi'^*}{\partial r}y_1(r)\right) \times\left(\int_0^R r^2 dr\, n(r)\frac{\partial\psi}{\partial r}y_1(r)\right)\frac{1}{\mu-\omega_1} \tag{3.34}$$

as the matrix element in (3.32). Note this rate is not suppressed by the decay width Γ_1, because the scatter is elastic and concerns the real part of the matrix element.

In the sections that follow, we will be considering mixing rates for the two fastest known pulsars PSR J1748-2446ad (716 Hz) and PSR B1937+21 (642 Hz). We will use the nominal value $R \sim 12$ km for both, the measured mass $M = 1.96 M_\odot$ for PSR J1748-2446ad, and the nominal mass $M \sim 1.4 M_\odot$ for PSR B1937+21 (see Section 3.4.2 for details).

3.4.1.2 Equatorial Bulge and Free Precession

Superradiance is effective only in a rapidly rotating neutron star. A rapidly rotating neutron star will not remain spherically symmetric owing to centrifugal pressures that will cause the star to develop an equatorial bulge, giving rise to a quadrupole moment for the star [60]. But, this rotation by itself does not break the axisymmetry around the rotational axis and hence this quadrupole moment breaks spherical symmetry but preserves axisymmetry. Consequently, this effect leads to mixing between the hydrogenic modes of (3.4) that carry different radial (n) and total orbital angular momenta (l) while preserving the azimuthal quantum number m, *i.e.* it mixes states of the form ψ_{nlm} and $\psi_{n'l'm}$. Since the azimuthal quantum numbers m are unaffected, this mixing does not couple the superradiant modes with absorptive modes.

However, the rotation axis of a real neutron star will undergo free precession. The rotation axis of the star is tilted from the precession axis by a "wobble angle" θ_w, about which it precesses with a frequency Ω_p. These effects break the axisymmetry of the system, leading to coupling between the rotational quadrupole deformation and modes of different azimuthal angular quantum momenta. Let us first estimate the sizes of these asymmetries before computing their effects on the modes. The free precession frequency Ω_p of the star is given by $\Omega_p = \frac{\Delta I}{I}\Omega$ where I is the moment of inertia of the star and ΔI is its non-axisymmetric piece [61]. We estimate ΔI to be of order the quadrupole moment Q induced by the rotation of the star. This has been estimated for a variety of equations of state to be $Q = qG^2M^3$, with $q \sim 1$ for the most rapidly rotating neutron stars [60]. Using Q, the ratio $\frac{\Delta I}{I} \sim q\left(\frac{GM}{R}\right)^2$, giving rise to a precession frequency $\Omega_p \sim q\left(\frac{GM}{R}\right)^2\Omega$. Similarly, the maximum "wobble angle" θ_w about which the star can precess without breaking apart has been estimated to be $\sim 10^{-3}\left(\frac{2\pi\cdot 1\text{kHz}}{\Omega}\right)^2$ [61].

We now estimate the mixing that is caused by the wobble θ_w rotating with a frequency Ω_p. There are two sources that can cause this mixing. First, the gravitational perturbations from the wobble can cause mixing. And secondly, the interaction (3.6) can cause the modes

to mix via their interaction with the wobbling stellar medium. To calculate the gravitational effects of the wobble, we must first know the mass moments of the tilted star. We estimate the wobble-induced quadrupole moments by treating the star as a uniform density ellipsoid tilted by a small angle. The resulting moments are given by

$$Q_{2m} \sim Q \left(\theta_w Y_{2,1}\, e^{-i\Omega_p t} + \theta_w^2 Y_{2,2}\, e^{-i2\Omega_p t} + \text{h.c.}\right) \tag{3.35}$$

For a rotating pulsar we have $Q = qG^2M^3$ as discussed above. Because this wobble induces quadrupole perturbations in the system, it is able to effectively mix the ψ_{322} mode with the strongly absorptive scalar states, such as ψ_{100}. It could also mix ψ_{211} with $\psi_{21,-1}$ or ψ_{210}, but these three modes have the same overlap with the star and thus comparable superradiance/absorption rates, and we will therefore simply require $\delta^2 \lesssim 1$.

To understand condition (3.31), we now need to calculate the absorption rate C_{100} of the ψ_{100} mode. This mode couples primarily to the lowest $l = 0$ breathing mode of the star, but this has a frequency similar to the $l = 1$ phonon and $l = 2$ phonon that the ψ_{211} and ψ_{322} scalars couple to, respectively [57]. And, because of the star's rotation (see Section 3.4.2), the $l = 0$ and $l = 1$ phonon modes also have similar damping rates, roughly 10^{-1} suppressed relative to the $l = 2$ phonon. Inserting the hydrogenic wavefunction ψ_{100} into equation (3.28), we find the ratios

$$\frac{\Gamma_{211}}{\Gamma_{100}} \sim \frac{\Gamma_{322}}{\Gamma_{100}} \sim 10^{-6} \left(\frac{M}{1.4M_\odot}\right)^2 \left(\frac{R}{12\text{ km}}\right)^2 \left(\frac{\mu}{10^{-11}\text{ eV}}\right)^4 \tag{3.36}$$

With these ratios in hand and an estimate of the mixing from gravitational effects using equations (3.32) and (3.33), we find that the condition (3.31) is easily satisfied in our region of interest. The wobble-induced gravitational perturbations do not damp the superradiant growth of the scalar modes.

Scattering off neutrons, on the other hand, can provide efficient mixing. The mixing fractions to absorptive modes from scalar-neutron scattering are given by equations (3.32) and (3.34). We can estimate the wobble-induced density perturbations by

$$\frac{\delta\rho}{\rho_0} \sim \left(\frac{\Delta I}{I}\right) \left(\theta_w Y_{2,1}\, e^{-i\Omega_p t} + \theta_w^2 Y_{2,2}\, e^{-i2\Omega_p t} + \text{h.c.}\right) \tag{3.37}$$

Mixing between modes with $\Delta m = |m - m'| = (1 \text{ or } 2)$ therefore proceeds with a perturbation of amplitude $\delta R/R \sim (\Delta I/I)\theta_w^{\Delta m} \sim 10^{-7} - 10^{-4}$. Considering the same mixing channels, we find that the ψ_{211} superradiance is not affected, but the $\psi_{322} \to \psi_{100}$ mixing can spoil superradiance of the ψ_{322} mode for large values of the Yukawa coupling. This is folded into our constraint plots.

3.4.1.3 Equatorial Ellipticity

The mass distribution in the star will break axisymmetry at some level. The multipole moments of this anisotropy will mix modes with different azimuthal angular momenta thereby

mixing modes with different azimuthal angular momenta. Distortions from axisymmetry are captured by the dimensionless equatorial ellipticity of the star $\epsilon_s = \frac{I_{xx}-I_{yy}}{I_{zz}}$ [62] where the Is are the moments of inertia of the system about the respective axes. The maximum values of ϵ_s that can be supported by the star have been estimated to be $\sim 10^{-7}$ [62]. This asymmetry creates a time dependent perturbation of the star that rotates with the frequency Ω of the star. Following section 3.4.1.2, we estimate that the effects of equatorial ellipiticity are much smaller than those of the free precession of the star. This is because the asymmetry size $\delta R/R \sim \epsilon_s$ of the equatorial ellipiticity is no bigger than the wobble-induced asymmetry, and this perturbation varies at a frequency Ω larger than the precession frequency Ω_p responsible for the wobble-induced mixing.

It is also possible that the star may occasionally undergo some internal violent process that causes it to release a sudden burst of radiation. These processes are also not efficient in mixing multiple levels. The change to the total mass of the star caused by such an event is irrelevant since such a change is axisymmetric and cannot mix modes of different azimuthal angular quantum numbers. After the explosion, the equatorial ellipticity of the star will be different than the value it started out with and this change in the ellipticity can mix all the modes. But, the new value of the ellipticity cannot be larger than the maximum allowed by the equation of state of the star. Furthermore, the change to the equatorial ellipticity will also be suppressed by the actual mass lost in the process and since this change must be much less than the actual mass of the star (else the star could not have survived the explosion), the effect of such explosions are insignificant. We treat the effects of "stellar quakes" on mixing the modes in the next section.

3.4.1.4 Mixing via Phonons

Stars can support phonon modes in any multipole, including dipole phonon modes so long as there are one or more radial nodes. As discussed previously, we must consider the mixing effects of dipole and quadrupole perturbations, which may affect our superradiant modes of interest. These phonons can be populated thermally, by stellar quakes, or by other driving mechanisms in the star. For thermally populated phonons, $\delta R/R \propto 1/\sqrt{N}$, and these perturbations are too small to provide any efficient mixing.

Stellar quakes, on the other hand, may efficiently mix when they occur. Recall from 3.4.1.2 that the maximal dimensionless ellipticity ϵ_s that can be supported by the star is roughly $\sim 10^{-7}$. Strictly speaking, this is only a bound on quadrupolar deformations of the star, but we will use it as a proxy to estimate the maximal displacement of any multiple deformation. The pulsar may have undergone violent "stellar quakes" in its history, but the displacements caused by such quakes must be smaller than the maximum equatorial ellipticity ϵ_s that can be supported by the star. We will therefore take $\delta R/R \sim 10^{-7}$ to be a conservative upper bound on the quake-produced phonon amplitudes that might cause mixing. This effect isn't stronger than the wobble-induced mixing for ψ_{322} superradiance, for the same reasons that we can ignore the equatorial ellipticity effect, but for sufficiently large values of the coupling it could serve to spoil ψ_{211} superradiance through mixing with

ψ_{100}. At worst, this might limit our ability to place constraints above $\epsilon \sim 10^{-18}$, which is already stronger than gravity and so not of great interest to us. Furthermore, period glitches are rare in old pulsars, and so we may suppose that stellar quakes are also [63]. The effect of stellar quake mixing, therefore, is simply to reduce the effective lifetime of our star that is useful for superradiance. So long as the millisecond pulsar has not experienced a quake within the past $O(1)$ of its lifetime, we may ignore this effect.

3.4.1.5 Disruptive Companions

Accretion from the companions is often believed to be the mechanism responsible for powering the initial spin up of the neutron star to the millisecond regime [59], and most millisecond pulsars still have small companions $\lesssim M_\odot$ [59]. A companion object of mass M_c at a distance r_c will cause tidal disruptions of the bound particle state. The tidal disruption provides dipole and quadrupole gravitational perturbations which can cause the ψ_{211} and ψ_{322} states to get absorbed through mixing with $l = m = 0$ states. Typically we would be most concerned with the ψ_{100} state, since it has the largest absorption rate, but in this case the more dangerous mixing channels are ψ_{200} and ψ_{300} because the smaller energy difference between the initial and final scalars leads to a smaller denominator in the mixing (3.32). Expanding the gravitational potential due to the companion at the pulsar, we find the non-zero matrix elements for the desired mixing processes are

$$\begin{aligned}\delta^2_{211\to\text{abs}} &\sim \frac{\left|\langle\psi_{200}|\, G\, M_c\, \mu\, \frac{r Y_{1,-1}}{r_c^2}\, |\psi_{211}\rangle\right|^2}{(\Omega_c - (E_{200} - E_{211}))^2} \\ \delta^2_{322\to\text{abs}} &\sim \frac{\left|\langle\psi_{300}|\, G\, M_c\, \mu\, \frac{r^2 Y_{2,-2}}{r_c^3}\, |\psi_{322}\rangle\right|^2}{(\Omega_c - (E_{300} - E_{322}))^2}\end{aligned} \tag{3.38}$$

Unlike the previous mixing processes, where the denominator was always dominated by the oscillation frequency of the perturbation, the denominator in (3.38) can be dominated by the energy difference between the states. This is because we wish to describe companions that are relatively far from the star—the time variation Ω_c from these objects may therefore typically be slower than the energy differences between the states. It will turn out that the orbital rate dominates the denominator for PSR J1748-2446ad, whereas the energy splitting dominates the denominator for the nearly isolated pulsar PSR B1937+21.

The most dangerous mixings are between that of the superradiant mode $\psi_{l+1,ll}$ and the absorptive mode $\psi_{l+1,00}$, instead of ψ_{100} as in the other mixing processes, because these two states are nearly degenerate in energy. In Newtonian gravity, these levels are exactly degenerate, up to corrections from deviations from spherical symmetry. This exact degeneracy in Newtonian gravity is a feature of the pure r^{-1} nature of the potential. But, General Relativity induces corrections to this law. For example, the gravitational effects of angular momentum leads to corrections to the r^{-1} potential, giving rise to familiar effects such as the GR corrections to the precession of the perihelion of Mercury. Similarly, since the states

$\psi_{l+1,ll}$ and $\psi_{l+1,00}$ have different total angular momenta, their energies will also be different. We can estimate this splitting to be roughly $\frac{GM\mu}{r_b}v_b^2 \sim \frac{(GM\mu)^4\mu}{l^4}$, where $r_b \sim l^2/(GM\mu^2)$ and $v_b \sim GM\mu/l$ are the radius and typical tangential velocity of the particle's orbit in a Bohr model of this gravitational atom.

The fastest known pulsar PSR J1748-2446ad with a rotation frequency of 716 Hz [58] has a companion of mass $0.1M_\odot$ at an orbital period ~ 26 hours. The second fastest pulsar PSR B1937+21 (with a rotation frequency 642 Hz) is known to be an isolated pulsar, with an upper bound of $\lessapprox 10^{-9}M_\odot$ on any companion for a distance as large as $\sim 3\times 10^8$ km [59]. Since these are the fastest known pulsars, we will use their existence to impose various bounds on particle physics models in section 3.4.2. Inserting these values, we find the condition (3.31) prevents superradiant growth for low values of μ around PSR J1748-2446ad due to its companion, but scalars around the isolated PSR B1937+21 are unaffected by tidal mixing.

Finally, we can also estimate the maximum possible effect of accreting gas on the particle modes. The maximum rate of accretion is limited by the Eddington limit, where the radiation pressure on free electrons balances gravity. This rate is $\sim 4\times 10^{-8}M_\odot \mathrm{yr}^{-1}$ [59]. This estimate is almost certainly an overestimate as the accretion rate should fall as we move away from the star. Using this limit, the maximum amount of mass that could be accreting even out to a distance $r_c \sim 10^7$ km is $\sim 10^{-15}M_\odot$, too small to provide any problematic mixing.

In addition to mixing with $\psi_{l+1,00}$, we may also worry about mixing with absorptive modes $\psi_{l+1,l,-l}$. These have overlap with the star similar to the superradiant meds, leading to absorptive rates $\Gamma_{l+1,l,-l} \sim \Gamma_{l+1,ll}$. Hence, as long as the mixing between these modes is less than 1, the superradiant mode will easily grow. The mixing between them is given by an equation analogous to (3.38). But, we need to estimate the energy difference between these two states. The GR correction identified in the above paragraph gives an identical contribution to the energies of both states since they have the same total angular momentum. But, since we are dealing with a spinning neutron star, there is an additional contribution to the energies of these states from gravitomagnetism. A spinning object generates gravitomagnetism which leads to the analogue of the "spin-orbit" coupling between the rotating neutron star and the azimuthal quantum number of the state. This gravitomagnetic field $B_g \sim G\frac{MR^2\Omega}{r_b^3}$ and it couples to the tangential velocity $v_b \sim \sqrt{\frac{GM}{r_b}}$ of the mode. In a mode with non-zero azimuthal angular momentum, $\langle v_b\rangle$ is non-zero and hence this gives rise to an energy splitting $\sim G\frac{M\mu R^2\Omega}{r_b^2}v_b$. Numerically, we find that this splitting is a tenth or less of the GR correction computed in the above paragraph for the states of interest to us in section 3.4. These mixings will be larger by a factor of 100 or more for the isolated PSR B1937+21, for which the mixing is dominated by the energy splitting. However, since both these states have nearly identifical absorption rates the stability condition (3.31) is still easily satisfied for mixing between these modes.

3.4.2 Results

The estimates in section (3.4.1) suggest that the superradiant mode can grow in real astrophysical environments. The existence of long lived, rapidly rotating pulsars constrains particles that can undergo efficient superradiant growth since superradiant growth occurs at the expense of the rotational energy of the star. We will use the pulsars PSR J1748-2446ad (716 Hz) [58] and PSR B1937+21 (642 Hz) [59] to constrain particles that couple to the stellar medium. These pulsars are particularly interesting because not only are they the fastest known pulsars, but their astrophysical environment is also devoid of close, massive companions whose presence may disrupt the growth of the superradiant mode (see section 3.4.1.5).

The existence of these pulsars implies that the rate (3.28) is small enough so that the pulsars would not have significantly slowed down due to superradiant emission during their lifetime τ. The angular momentum of the star is $L_s \sim 10^{176}\hbar$ and the emission of each particle of mass μ with azimuthal angular momentum $m \sim 1$ costs angular momentum $\sim \hbar$. The superradiant mode grows as $e^{\Gamma_{l+1,ll}\tau}$ and we require that this exponential term be smaller than $\sim \frac{L_s}{\hbar}$, implying $\Gamma_{l+1,ll} \lessapprox \frac{176}{\tau}$. Bounds can be placed on particles that fail this test. But, in order to do so, we need to know the age τ of the pulsar in question.

Reliable upper bounds on the age of the pulsar can be placed from measurements of the spin down rates of the star. The spin down rate gives an estimate of the time required for the frequency of the pulsar to change by an order one amount. This time, called the characteristic age of the pulsar, is $\sim 2 \times 10^8$ years for PSR B1937+21 [64]. Reliable observational lower bounds on the pulsar lifetime are obviously harder to establish. Millisecond pulsars are old objects and are not the result of recent stellar activity [59]. In some cases, such as PSR J0034-0534, a lower bound on the age of the pulsar can be determined by observations of the temperature of its companion star [64], which is correlated with its age. These observations suggest that millisecond pulsars are old objects with ages $\sim 10^8 - 10^9$ years. There are also theoretical arguments that suggest this lifetime. The formation of these rapid pulsars are believed to have been the result of accretion from a nearby companion star. The progenitor neutron star needs to accrete mass $\sim 0.1 M_\odot$ in order to achieve the rotation rates observed in milli-second pulsars [59]. Accretion at the maximum possible Eddington rate of $\sim 4 \times 10^{-8} M_\odot \mathrm{yr}^{-1}$ [59] suggests that the lifetime of the star τ must be at least $\gtrsim 10^7$ years. Consequently, if the accretion proceeds slightly more slowly than the maximum possible Eddington rate, the time neccessary to form the source must be $\gtrapprox 10^8$ years. It is thus reasonable to take the age of the pulsar to be equal to the pulsar's measured characteristic age $\sim 10^8 - 10^9$ years. Furthermore, we will suppose that the pulsar has been spinning at its current rate for $\mathcal{O}(1)$ of this lifetime.

While the characteristic age of PSR B1937+21 has been measured, this determination has not yet been made for PSR J1748-2446ad. Current measurements of the spin down rate of PSR J1748-2446ad suggest a lower bound on its characteristic lifetime $\gtrapprox 2.5 \times 10^7$ years [58]. This lower bound is too conservative since formation from accretion would take longer. Instead, we use the following method to estimate the characteristic age of this object. The

pulsar's characteristic age is determined from its measured rotation rate and the magnitude of its dipole magnetic field. Millisecond pulsars typically have surface dipole magnetic fields clustered around $\sim 3 \times 10^4$ T [64]. Taking this to be the surface magnetic field of PSR J1748-2446ad, we estimate its characteristic age $\sim 10^9$ years. With all this in consideration, we conservatively take the stellar lifetime to be $\tau = 3 \times 10^8$ years for each pulsar in setting our constraints.

We are nearly ready to place bounds on scalars of mass μ that couple to neutrons through a Yukawa interaction of strength ϵ. Stellar parameters such as the temperature T, mass (in order to obtain the number of neutrons N), radius R, the frequency ω_1 of the lowest phonon mode and its damping rate Γ_1 enter into the estimate of the superradiance rate (3.28). For old neutron stars, whose ages are much longer than 10^6 years, the temperature T of the star is $\lessapprox 5 \times 10^5$ K [65]. However, millisecond pulsars tend to be somewhat warmer, $T \sim 10^7 - 10^8$ K [66]. We will take the pulsar temperatures to be at the lower end of this range, $T \sim 10^7$ K. The mass of the star is directly obtained from observations of these objects [58, 59] where they exist. The mass of PSR J1748-2446ad has been determined to be $1.96 \pm 0.04\, M_\odot$ [58]. The mass of PSR B1937+21 has not been measured and we take it to be equal to the nominal neutron star mass $\sim 1.4 M_\odot$ [59]. Similarly, the stellar radius for both pulsars is taken to be the nominal size of a neutron star ~ 12 km [59].

The frequencies and damping rates of phonon modes were estimated in [57]. In placing bounds we will mostly concentrate on excitations of the lowest-frequency $l = 1$ and $l = 2$ modes by the absorption of a scalar. We are also interested in the $l = 0$ oscillations for the purposes of mixing estimates (see Section 3.4.1). In particular, we focus on absorption into the lowest-frequency stellar oscillations, which have 0 radial nodes (or 1, in the case of the dipole oscillation). Of course, one could also include absorption into higher-frequency oscillations with the same angular structure but more radial nodes—but these are at progressively higher frequenices ω_n and the absorption rate is $\propto \omega_n^{-4}$, so summing over them does not notably enhance the absorption rate. The lowest-frequency $l = 0$ and $l = 2$ phonons are typically at frequencies $\omega_1 \sim 2\pi(2$ kHz), and the $l = 1$ mode is typically at $\omega_1 \sim 2\pi(4$ kHz), somewhat higher because the lowest-frequency dipole phonon has a node in the star. Of these, the $l = 2$ mode undergoes damping through gravitational radiation with a damping rate $\Gamma \sim 10$ Hz. The $l = 0$ and $l = 1$ modes do not damp through gravitational radiation in a non-rotating pulsar. But, in a rapidly rotating pulsar, whose rotational frequency is $\sim$ kHz, these modes will also radiate efficiently through gravitational wave emission, both at a rate suppressed roughly by $\sim 10^{-1}$ compared to the quadrupole phonon.

We have estimated the $l = 0, 1$ damping rates by noting that the rotating star has equilibrium density $\rho_0 \propto (Y_{00} + cY_{20})$, where $c \sim 0.2$ corresponds to the quadrupole moment $Q \sim G^2 M^3$ of a rapidly rotating star [60]. The continuity equation $\delta\rho = -\nabla \cdot (\rho_0 \boldsymbol{\delta}\mathbf{r})$ relates the $\delta r \sim Y_{lm}$ displacements to the resulting density perturbations. Taking simple approximate wave functions for the breathing and dipole phonon modes $\delta r \sim Y_{00}, Y_{11}$, and a stellar density profile $\rho_0 \propto (1 - (r/R)^2)$, we find that the $l = 0$ phonon mode decays via quadrupole radiation at a rate $\Gamma_{l=0} \sim 0.1\, \Gamma_{l=2}$. The $l = 1$ mode decays via octupole radiation, yet because it oscillates at a higher frequency the decay rate is similar. This is

admittedly a rough estimate, but sufficient for us for two reasons: first, both the mixing cutoffs and the ψ_{211} superradiance bounds are only mild functions of Γ, and second, our strongest bounds in any case come from ψ_{322} superradiance, which is unaffected by these estimates except through the (very mild) effects on mixing.

As we go to higher masses, the superradiant modes will have higher angular momentum. The absorption of these modes will then lead to excitation of phonon modes with $l > 2$. The superradiance rate of these high angular momentum modes is suppressed due to two reasons. First, the overlap of the mode with the star is suppressed, as the modes have high angular momentum. Second, the absorption of these modes results in excitation of modes of high angular momentum in the star. These high angular momentum modes are not as highly damped by gravitational wave emission since they correspond to higher multipole excitations of the star. The damping rates of modes with $l \geq 2$ are given by $\Gamma \sim 10^{5-2l}$ Hz [57]. Both these effects suppress the superradiance rate, limiting the ability of this method to probe scalars of mass $\mu \gg \Omega$. For this reason, we will only place bounds on scalar masses superradiant in the $l = 1$ and $l = 2$ modes.

With these parameters, in figures 3.2 and 3.3, we place bounds in the $\epsilon - \mu$ plane for scalar interactions with the neutron, using the existence of the pulsars PSR J1748-2446ad (716 Hz) and PSR B1937+21 (642 Hz) respectively. Figure 3.4 represents bounds that could be placed with the discovery of an isolated pulsar rotating at 1200 Hz, and relates them to the other constraints. These bounds consider the superradiant modes ψ_{211} and ψ_{322}, coupling respectively to dipolar and quadrupolar oscillations in the star. The bounds exhibit wiggles at masses μ of the scalar that are integral multiples of the stellar rotational frequency Ω. This is because the superradiance condition $\mu - m\Omega < 0$ is satisfied by modes of increasing angular momentum as we go up in μ. We note that existing bounds are $\epsilon \lesssim 5 \times 10^{-23}$ for most of this parameter space [42], set by weak equivalence principle tests with torsion balances. We are able to improve on these by up to 3 orders of magnitude. The bounds are maximally good in the region right near $\mu \approx 2\Omega$. This is slightly different from our original expectation of $\mu \approx \Omega$, and a result of the more efficient coupling and dissipation of the quadrupolar modes (see Section 3.3.1.1).

The bounds in Figures 3.2, 3.3, and 3.4 are cut off above and on the left when the superradiant mode is damped by astrophysical anisotropies, primarily the free procession wobble and tidal forces from the companion star (as discussed in section 3.4.1). At large couplings, the free procession wobble causes the ψ_{322} superradiant mode to be sufficiently strongly mixed with absorptive modes, providing the upper limit to the constraints. This occurs when the Yukawa coupling mediates a force comparable to gravity ($\epsilon \sim G m_n^2 \sim 10^{-19}$), and so wobble-induced scattering to certain absorptive scalar states becomes nearly as efficient as scattering into gravitons (i.e., the superradiant process). The constraints due to PSR J1748-2446ad are additionally limited at low masses μ due to disruption of the superradiant growth by its companion star. This typically occurs because in this region, the superradiant modes have large Bohr radii with a suppressed overlap with the star. But, the damped absorptive modes ψ_{n00} always have support at the origin making their damping rates significantly bigger than the superradiant growth rates. Consequently, the condition (3.31)

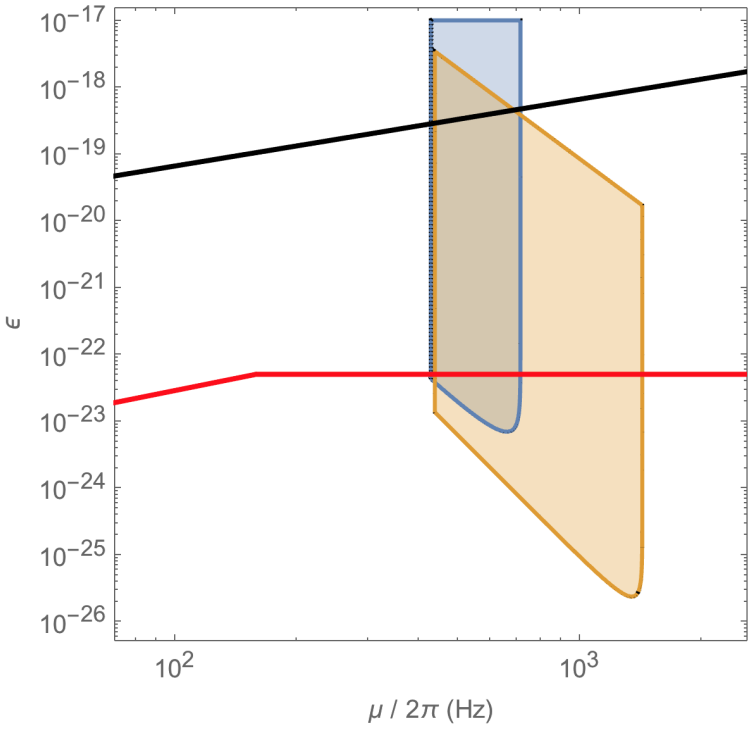

Figure 3.2: Constraints imposed by the existence of PSR J1748-2446ad (716 Hz) on scalars of mass μ with Yukawa coupling ϵ to neutrons. Shaded regions are excluded due to superradiance into ψ_{211} (blue) and ψ_{322} (orange) scalar modes. The right most boundaries are fixed by the superradiance condition $m\Omega - \mu > 0$, and on the left constraints are limited by mixing from companion star tidal forces. The ψ_{322} constraints are limited at large coupling due to mixing through the free precession wobble. The red line shows existing constraints from torsion balance experiments. The black line represents the mass-coupling relation for the QCD axion, assuming $\theta_{eff} \sim 1$ in the star.

becomes increasingly harder to satisfy as tidal forces cause mixing between the superradiant and absorptive modes. PSR B1937+21 (Figure 3.3) avoids mixing from a stellar companion because is a nearly isolated pulsar with its closest companion at least $\sim 3 \times 10^8$ km away with mass $\lessapprox 10^{-9} M_\odot$. We take the hypothetical 1200 Hz pulsar (Figure 3.4) to be similarly isolated. PSR J1748-2446ad (Figure 3.2) on the other hand has a companion of mass $\sim 0.1 M_\odot$ at a distance 3.9×10^6 km away from it.

Our results take on an additional meaning if indeed $\theta_{\text{eff}} \sim 1$ in a neutron star, as predicted by various neutron star equations of state [56]. In this case, the QCD axion acquires a CP-violating Yukawa coupling to neutrons $\epsilon \sim \theta_{\text{eff}} m_n / f_a \sim m_n / f_a$, and the vertical axis on our plots can be read off as $(f_a/\text{GeV})^{-1}$. We are thus able to exclude QCD axions with Planck scale decay constants. We stress that this claim depends on the equation of state of the

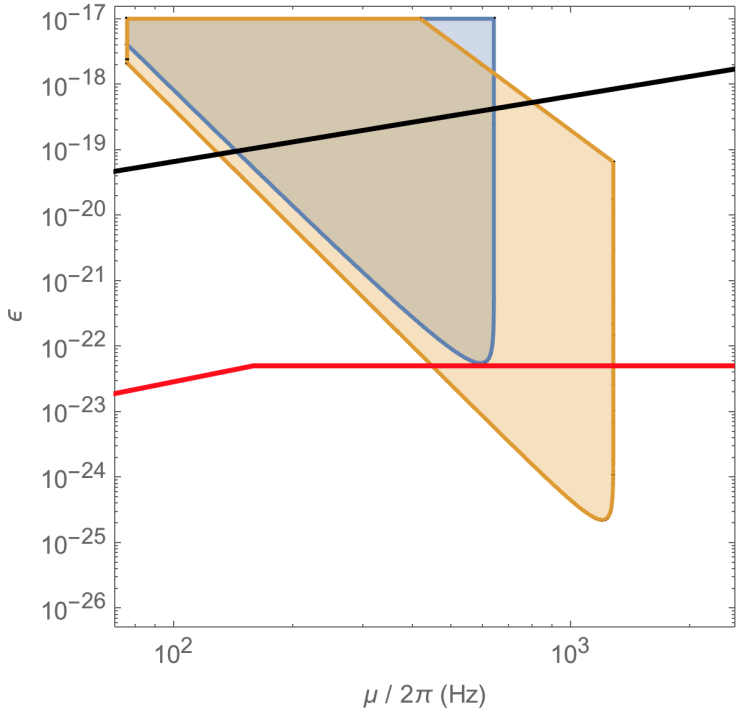

Figure 3.3: Constraints imposed by the existence of PSR B1937-21 (642 Hz) on scalars of mass μ with Yukawa coupling ϵ to neutrons. Shaded regions are excluded due to superradiance into ψ_{211} (blue) and ψ_{322} (orange) scalar modes. The right most boundaries are fixed by the superradiance condition $m\Omega - \mu > 0$. The ψ_{322} constraints are limited at large coupling due to mixing through the free precession wobble. The red line shows existing constraints from torsion balance experiments. The black line represents the mass-coupling relation for the QCD axion, assuming $\theta_{eff} \sim 1$ in the star.

neutron star.

We have thus constrained any scalars (or pseudoscalars) with a Yukawa coupling (3.6) to neutrons. We improve on the existing torsion balance constraints for scalar masses 2×10^{-12} eV $\lesssim \mu \lesssim 6 \times 10^{-12}$ eV (430 Hz $\lesssim \mu/2\pi \lesssim$ 1420 Hz), and (pending the pulsar equation of state) constrain QCD axions with Planck-scale decay constants and masses 5×10^{-13} eV $\lesssim \mu \lesssim 3 \times 10^{-12}$ eV (120 Hz $\lesssim \mu/2\pi \lesssim$ 800 Hz).

3.5 Conclusions

The superradiant instabilty of the gravitationally bound states of millisecond pulsars allows their use as an interesting laboratory to search for light, weakly coupled particles. Measurements from the two fastest known pulsars PSR J1748-2446ad and PSR B1937+21 place

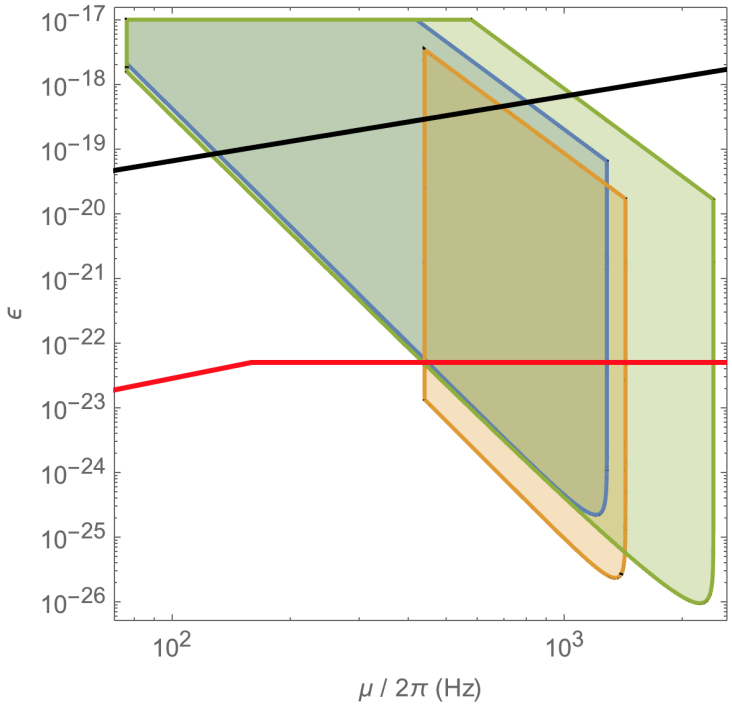

Figure 3.4: Constraints on scalars of mass μ with Yukawa coupling ϵ to neutrons. Shaded regions are excluded due to superradiance into ψ_{322} by PSR B1937-21 (642 Hz, blue), PSR J1748-2446ad (716 Hz, orange), and a hypothetical isolated pulsar rotating with a speed of 1200 Hz (green). The PSR J1748-2446ad constraints jut below the others primarily due to the star's larger mass (1.96 $M_\odot$ vs 1.4 $M_\odot$) The red line shows existing constraints from torsion balance experiments. The black line represents the mass-coupling relation for the QCD axion, assuming $\theta_{eff} \sim 1$ in the star.

bounds on scalars with wavelengths between 100 km - 10^4 km, improving current bounds by two to four orders of magnitude over this range. Also, if $\theta_{\text{eff}} \sim 1$ in a neutron star as predicted by some equations of state, the QCD axion with a mass in the range $\mu \sim 800$ Hz - 9000 Hz would be ruled out. The discussions in this paper were restricted to scalars with Yukawa interactions to neutrons. It may be interesting to study a larger class of interacting systems. Using the methods of this paper, it can be readily checked that pseudo-scalar interactions of Ψ with nuclei/electrons cannot be constrained by superradiance using known parameters of milli-second pulsars. A careful consideration of mixing with absorptive modes in context of the electromagnetic mechanisms of [54, 55] may allow the results of those papers to be reinterpreted as realistic constraints. Other potentially dissipative mechanisms would also be interesting to investigate, such as an oscillating neutron electric dipole moment induced by an axion-like coupling.

Intriguingly, there appears to be an absence of pulsars with frequencies above ~ 700 Hz.

This is a puzzling phenomenon since many equations of state of the neutron star can support frequencies well above 1 kHz before break up [67]. It is unclear if this phenomenon can be explained through standard model processes such as gravitational wave emission, though a variety of astrophysical mechanisms have been proposed [68, 69, 70, 71, 72, 73]. (Some of these, such as the r-mode instability, are superradiance phenomena in their own right.) A particle that is sufficiently strongly coupled to the neutron star medium, with a mass around the breakup frequency, can furnish such a rapid cut off. This explanation could be tested with the discovery of more rapidly rotating pulsars. A pulsar braking mechanism caused by superradiance would lead to the clustering of pulsars at roughly half the mass of the putative particle. A conventional source for damping the stellar rotation such as gravitational wave emission would predict a gentler demise of pulsars on the curve up to rapid rotation. This anomaly may provide an impetus to search for new light particles that couple to neutrons with mass around $\mu \sim 2\pi \cdot 1500$ Hz in laboratory searches.

Chapter 4

White Dwarfs as Dark Matter Detectors

Dark matter that is capable of sufficiently heating a local region in a white dwarf will trigger runaway fusion and ignite a type Ia supernova. This was originally proposed by Graham et al. and used to constrain primordial black holes which transit and heat a white dwarf via dynamical friction. In this paper, we consider dark matter (DM) candidates that heat through the production of high-energy standard model (SM) particles, and show that such particles will efficiently thermalize the white dwarf medium and ignite supernovae. Based on the existence of long-lived white dwarfs and the observed supernovae rate, we derive new constraints on ultra-heavy DM with masses greater than 10^{16} GeV which produce SM particles through DM-DM annihilations, DM decays, and DM-SM scattering interactions in the stellar medium. As a concrete example, we place bounds on supersymmetric Q-ball DM in parameter space complementary to terrestrial bounds. We put further constraints on DM that is captured by white dwarfs, considering the formation and self-gravitational collapse of a DM core which heats the star via decays and annihilations within the core. It is also intriguing that the DM-induced ignition discussed in this work provide an alternative mechanism of triggering supernovae from sub-Chandrasekhar, non-binary progenitors.

4.1 Introduction

Identifying the nature of dark matter (DM) remains one of the clearest paths beyond the Standard Model (SM) and it is thus fruitful to study the observable signatures of any yet-allowed DM candidate. Many direct detection experiments are designed to search for DM, e.g. [74, 75], yet these lose sensitivity to heavier DM due to its diminished number density. Even for a strongly-interacting candidate, if the DM mass is above $\sim 10^{22}$ GeV a terrestrial detector of size $\sim (100\text{ m})^2$ will register fewer than one event per year. While these masses are large compared to those of fundamental particles, it is reasonable to suppose that DM may exist as composite states just as the SM produces complex structures with mass much

larger than fundamental scales (e.g., you, dear reader). Currently there is a wide range of unexplored parameter space for DM candidates less than $\sim 10^{48}$ GeV, above which the DM will have observable gravitational microlensing effects [76]. For such ultra-heavy DM, indirect signatures in astrophysical systems are a natural way forward. One such signal first proposed in [77] is that DM can trigger runaway fusion and ignite type Ia supernovae (SN) in sub-Chandrasekhar white dwarf (WD) stars.

In addition to constraining the properties of DM, this raises the intriguing possibility that DM-induced runaway fusion is responsible for a fraction of observed astrophysical transients. The progenitors of type Ia SN are not fully understood [78], and recent observations of sub-Chandrasekhar [79, 80], hostless [81], and unusual type Ia SN [82] suggest that multiple progenitor systems and ignition mechanisms are operative. Other suspected WD thermonuclear events, such as the Ca-rich transients [83], are also poorly understood. While mechanisms for these events have been proposed [84, 85, 86, 87], the situation is yet unclear and it is worthwhile to consider new sources of thermonuclear ignition.

Runaway thermonuclear fusion requires both a heating event and the lack of significant cooling which might quench the process. The WD medium is particularly suited to this as it is dominated by degeneracy pressure and undergoes minimal thermal expansion, which is the mechanism that regulates fusion in main sequence stars. Thermal diffusion is the primary cooling process in a WD, and it can be thwarted by heating a large enough region. The properties of a localized heating necessary to trigger runaway fusion were computed in [88]. Consequently, it was realized [77] that if DM is capable of sufficiently heating a WD in this manner, it will result in a SN with sub-Chandrasekhar mass progenitor. This was used to place limits on primordial black holes which transit a WD and cause heating by dynamical friction, although the authors of [77] identify several other heating mechanisms which may be similarly constrained. Note that the idea of using observations of WDs to constrain DM properties has been pursued before, e.g. through an anomalous heating of cold WDs [89, 90] or a change in the equilibrium structure of WDs with DM cores [91]. These are quite distinct from the observational signature considered in this work, which is the DM trigger of a type Ia SN (although see [92] for a related analysis).

In this paper, we examine DM candidates which have additional non-gravitational interactions and are thus capable of heating a WD and igniting a SN through the production of SM particles. An essential ingredient in this analysis is understanding the length scales over which SM particles deposit energy in a WD medium. We find that most high energy particles thermalize rapidly, over distances shorter than or of order the critical size for fusion. Particle production is thus an effective means of igniting WDs. Constraints on these DM candidates come from either observing specific, long-lived WDs or by comparing the measured rate of type Ia SN with that expected due to DM. It is important to note that these constraints are complementary to direct searches—it is more massive DM that is likely to trigger SN, but also more massive DM that has low terrestrial flux. The WD detector excels in this regime due to its large surface area $\sim (10^4 \text{ km})^2$, long lifetime $\sim$ Gyr, and high density. We demonstrate these constraints for generic classes of DM models that produce SM particles via DM-SM scattering, DM-DM collisions, or DM decays, and consider the significantly en-

hanced constraints for DM that is captured in the star. For these cases, we are able to place new bounds on DM interactions for masses greater than $m_\chi \gtrsim 10^{16}$ GeV. As a concrete example we consider ultra-heavy Q ball DM as found in supersymmetric extensions of the SM.

The rest of the paper is organized as follows. We begin in Section 4.2 by reviewing the mechanism of runaway fusion in a WD. In Section 4.3 we study the heating of a WD due to the production of high-energy SM particles. Detailed calculations of the stopping of such particles are provided in Appendix B.1. In Section 4.4 we parameterize the explosiveness and event rate for generic classes of DM-WD encounters, and in Section 4.5 we derive schematic constraints on such models. The details of DM capture in a WD are reserved for Appendix B.2. Finally we specialize to the case of Q-balls in Section 4.6, and conclude in Section 4.7.

4.2 White Dwarf Runaway Fusion

We first review the conditions for which a local energy deposition in a WD results in runaway fusion. Any energy deposit will eventually heat ions within some localized region—parameterize this region by its linear size L_0, total kinetic energy $\mathcal{E}_0$ and typical temperature T_0. These scales evolve in time, but it will be useful to describe a given heating event by their initial values.

The fate of a heated region is either a nonviolent diffusion of the excess energy across the star, or a runaway fusion chain-reaction that destroys the star. The precise outcome depends on L_0, $\mathcal{E}_0$ and T_0. There is a critical temperature T_f, set by the energy required for ions to overcome their mutual Coulomb barrier, above which fusion occurs. For carbon burning, $T_f \sim$ MeV [93]. Any heated region $T_0 > T_f$ will initially support fusion, although this is not sufficient for runaway as cooling processes may rapidly lower the temperature below T_f. This cooling will not occur if the corresponding timescale is larger than the timescale at which fusion releases energy. Cooling in a WD is dominated by thermal diffusion, and the diffusion time increases as the size of the heated region. However, the timescale for heating due to fusion is independent of region size. Thus, for a region at temperature $\gtrsim T_f$, there is a critical size above which the heated region does not cool but instead initiates runaway. For a region at the critical fusion temperature T_f, we call this critical size the *trigger size* λ_T. The value of λ_T is highly dependent on density, and in a WD is set by the thermal diffusivity of either photons or degenerate electrons. This critical length scale has been computed numerically in [88] for a narrow range of WD densities and analytically scaled for other WD masses in [77]. As in [77], we will restrict our attention to carbon-oxygen WDs in the upper mass range $\sim 0.85 - 1.4\ M_\odot$ (these will yield the most stringent constraints on DM). This corresponds to a central number density of ions $n_{\rm ion} \sim 10^{30} - 10^{32}$ cm^{-3} and a trigger size of $\lambda_T \sim 10^{-3} - 10^{-5}$ cm.

If a heated region is smaller than the trigger size, its thermal evolution is initially dominated by diffusion. However, this will still result in runaway fusion if the temperature is of

order T_f by the time the region diffuses out to the trigger size. For our purposes it is more natural to phrase this in terms of the total energy $\mathcal{E}_0$ deposited during a heating event. Of course, the relation between energy $\mathcal{E}_0$ and temperature T_0 depends on the rate at which WD constituents—ions, electrons, and photons—thermalize with each other within the region size L_0. Given that the different species thermalize rapidly, the excess energy required to raise the temperature to T_f in a volume V is given by a sum of their heat capacities

$$\frac{\mathcal{E}_0}{V} \gtrsim \int_0^{T_f} dT(n_{\rm ion} + n_e^{2/3}T + T^3), \tag{4.1}$$

where n_e is the number density of electrons. Note that we use the heat capacity of a degenerate gas of electrons, since the Fermi energy $E_F \gtrsim$ MeV for the densities we consider. The minimum energy deposit necessary to trigger runaway fusion is simply

$$\begin{aligned} \mathcal{E}_{\rm boom} &\sim \lambda_T^3(n_{\rm ion}T_f + n_e^{2/3}T_f^2 + T_f^4) \\ &\approx 10^{16} - 10^{23}\ \text{GeV}. \end{aligned} \tag{4.2}$$

$\mathcal{E}_{\rm boom}$ is shown over the range of WD masses in Figure 4.1, where we have employed a numerical formulation of the WD mass-density relation as given by [94]. Once again, for a given WD density the critical energy threshold is primarily set by λ_T—this length scale has been carefully computed and tabulated in [88], along with the attendant assumptions. In any case, we expect the simplified expression (4.2) to be accurate at the order of magnitude level, and we refrain from a more detailed analysis here. Thus for a heating event characterized by its L_0, $\mathcal{E}_0$, and $T_0 \gtrsim T_f$, there is an *ignition condition*:

$$\mathcal{E}_0 \gtrsim \mathcal{E}_{\rm boom} \cdot \max\left\{1, \frac{L_0}{\lambda_T}\right\}^3. \tag{4.3}$$

Any $\mathcal{E}_0$ satisfying this condition is minimized for L_0 less than the trigger size, where it is also independent of the precise value of L_0. For broader deposits, the necessary energy is parametrically larger than $\mathcal{E}_{\rm boom}$ by a volume ratio $(L_0/\lambda_T)^3$. As a result, understanding the L_0 for different kinds of heating events in a WD is critical to determining whether or not they are capable of destroying the star.

4.3 Particle Heating of White Dwarfs

Production of high-energy SM particles in a WD will result in heating of the stellar medium. The critical quantity to understand is the length scale over which such heating occurs—this scale determines the efficiency of the heating event in triggering runaway fusion, as described by condition (4.3). Note that this is a question of purely SM physics. The unknown physics of DM will serve only to set the initial properties of the SM particles.

We find that SM particles efficiently heat the WD regardless of species or energy (neutrinos are a slight exception)—the heating length is typically less than or of order the trigger

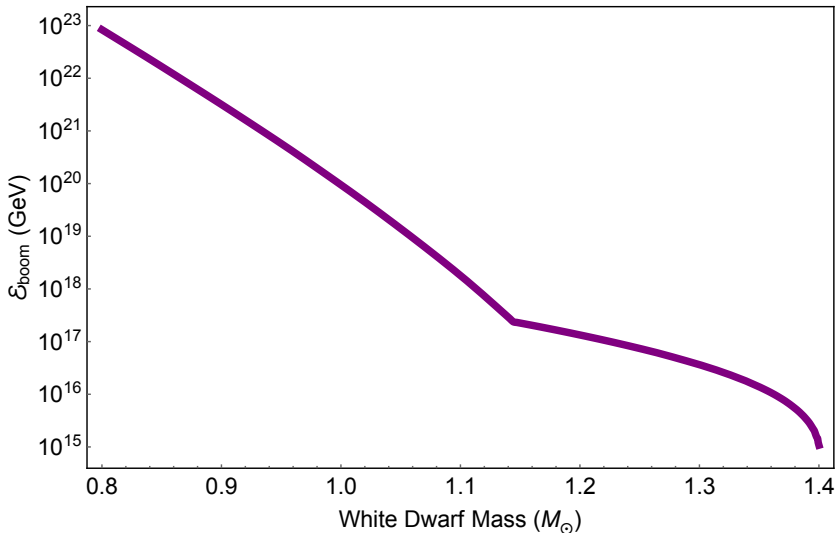

Figure 4.1: The minimum energy deposit (4.2) necessary to trigger runaway fusion, based on numerical results for λ_T [88] and the WD mass-density relation [94].

size λ_T. This is accomplished primarily through hadronic showers initiated by collisions with carbon ions. In some cases electromagnetic showers are important, however at high energies these are suppressed by density effects and even photons and electrons are dominated by hadronic interactions. These showers rapidly stop high-energy particles due to their logarithmic nature, transferring the energy into a cloud of low-energy particles which heat the medium through elastic scatters. A schematic for the flow of energy during deposition is given in Figure 4.2. In this light, the WD operates analogously to a particle detector, including hadronic and electromagnetic "calorimeter" components. Runaway fusion provides the necessary amplification to convert a detected event into an observable signal.

The remainder of this section will discuss the above heating process in more detail. We summarize the dominant source of energy loss and the resulting stopping lengths λ for SM particles of incident kinetic energy ϵ. The total path length traveled by a particle before depositing $\mathcal{O}(1)$ of its energy is approximately

$$R_{\rm SP} \sim \frac{\epsilon}{dE/dx}, \tag{4.4}$$

where dE/dx is the stopping power in the WD medium. If the mean free path to hard scatter $\lambda_{\rm hard}$ is smaller than this path length $R_{\rm SP}$, then the particle undergoes a random walk with $N_{\rm hard}$ scatters, and the net displacement is reduced by $\sqrt{N_{\rm hard}}$. We therefore approximate the stopping length as

$$\lambda \sim \min\left\{R_{\rm SP}, \sqrt{R_{\rm SP}\lambda_{\rm hard}}\right\} \tag{4.5}$$

This random walk behavior is relevant for low-energy elastic scatters.

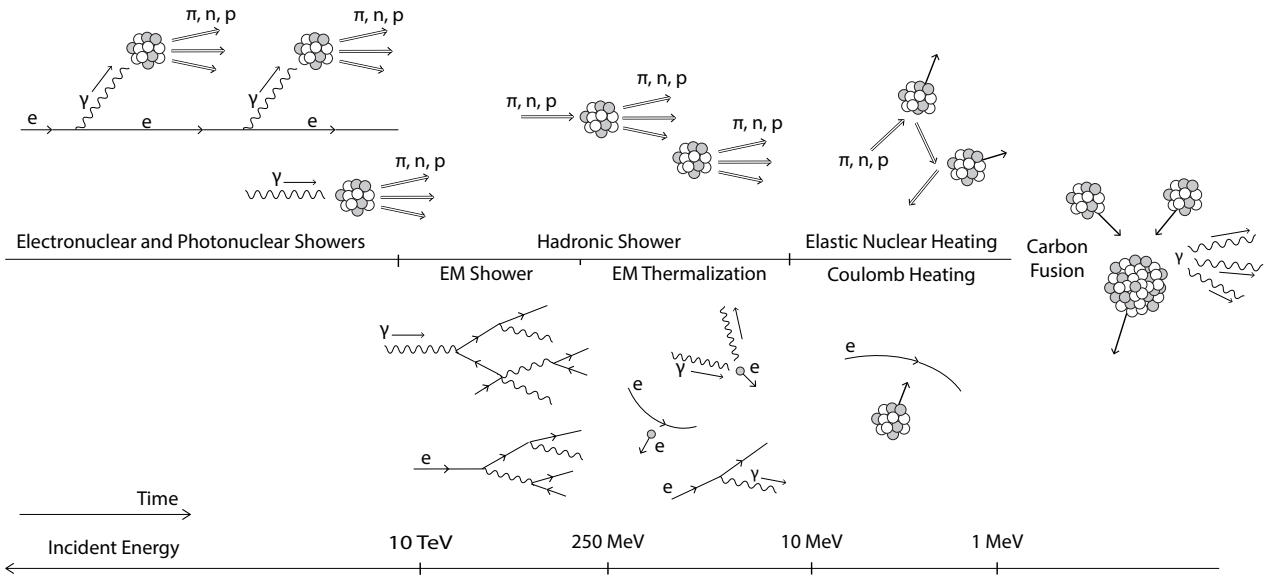

Figure 4.2: Dominant energy loss and thermalization processes in the WD as a function of energy, with energy decreasing towards the right. Hadronic processes are shown in the upper panel and EM processes in the lower panel. High energy particles will induce showers that terminate into elastic thermalization of the WD ions, moving from left to right in the diagram. The quoted energies are for a $\sim 1.37\ M_\odot$ WD, although the cartoon is qualitatively the same for all densities.

Stopping lengths are plotted in Figures 4.3 and 4.4, and a detailed treatment of the stopping powers is given in Appendix B.1. We will consider incident light hadrons, photons, electrons, and neutrinos—as we are concerned with triggering runaway fusion, we restrict our attention to energies $\epsilon \gg T_f \sim$ MeV.

4.3.1 High-Energy Showers

Hadronic Showers. Incident hadrons with kinetic energy larger than the nuclear binding scale ~ 10 MeV will undergo violent inelastic collisions with carbon ions resulting in an $\mathcal{O}(1)$ number of secondary hadrons. This results in a roughly collinear shower of hadrons of size

$$X_{\rm had} \sim \frac{1}{n_{\rm ion}\sigma_{\rm inel}} \log\left(\frac{\epsilon}{10\ {\rm MeV}}\right) \approx 10^{-6}\ {\rm cm} \left(\frac{10^{32}\ {\rm cm}^{-3}}{n_{\rm ion}}\right). \tag{4.6}$$

where the inelastic nuclear cross section is $\sigma_{\rm inel} \approx 100$ mb and we have taken the logarithm to be ~ 10. The shower terminates into pions and nucleons of energy ~ 10 MeV, whose cooling is discussed below. Note that neutral pions of energy $10 - 100$ MeV have a decay length

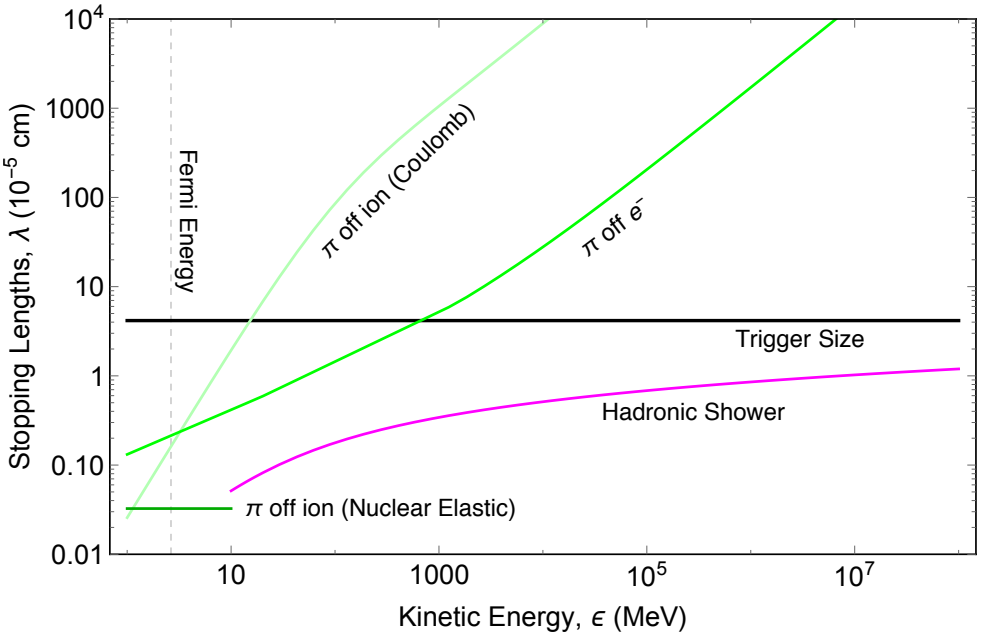

Figure 4.3: Stopping lengths for incident hadrons as a function of kinetic energy in a WD of density $n_{\rm ion} \sim 10^{31}$ cm^{-3} ($\approx 1.25\ M_\odot$), including the hadronic shower length (magenta). Any discontinuities in the stopping lengths are due to approximate analytic results in the different energy regimes. See Appendix B.1 for calculation details.

to photons of $\delta_{\pi^0} \sim 10^{-6}$ cm. Hadronic showers will therefore generate an electromagnetic component carrying an $\mathcal{O}(1)$ fraction of the energy.

Photonuclear and Electronuclear Showers. A photon or electron can directly induce hadronic showers via production of a quark-antiquark pair, depicted in Figure 4.5. The LPM effect, discussed below, ensures that these process dominate the stopping of photons and electrons at high energies, $\epsilon \gtrsim 10^4 - 10^6$ GeV.

The only substantial difference between photonuclear showers and purely hadronic ones is that they require a longer distance to initiate. Roughly, the photonuclear cross section is suppressed relative to the hadronic inelastic cross section $\sigma_{\rm inel}$ by a factor of α, and so the photon range is

$$\lambda_{\gamma A} \approx 10^{-5}\ \text{cm} \left(\frac{10^{32}\ \text{cm}^{-3}}{n_{\rm ion}} \right). \tag{4.7}$$

Here $\lambda_{\gamma A}$ is the distance to initiate a hadronic shower, whereas the shower itself extends a distance $X_{\rm had}$. Note that $\lambda_{\gamma A}$ is of order the trigger size.

The electronuclear showers are qualitatively different, as the electron survives the interaction. This process is best described as a continuous energy loss of the electron, due to

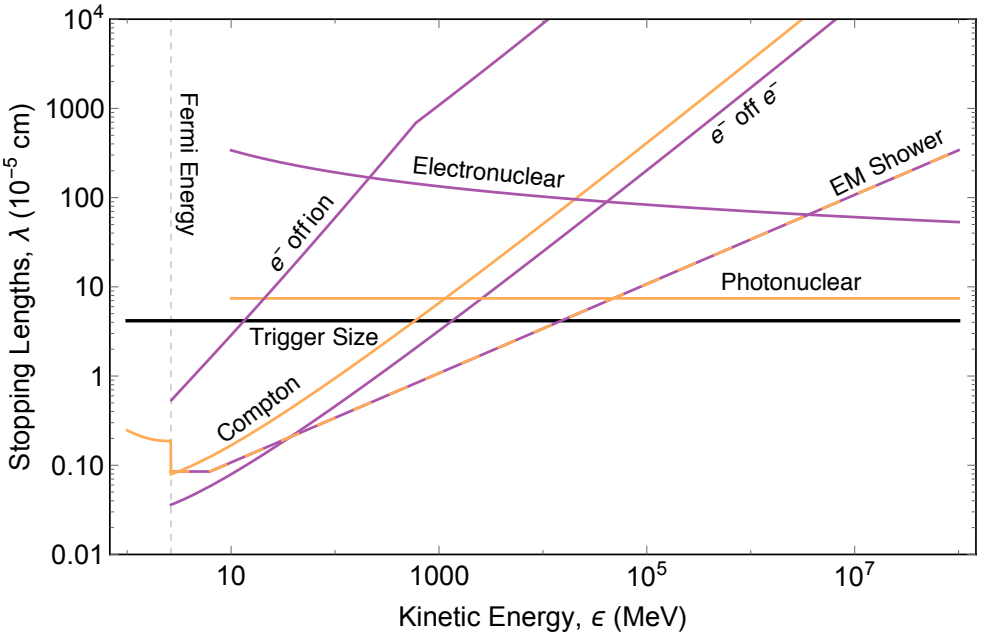

Figure 4.4: Stopping lengths of incident photons (orange) and electrons (purple) as a function of kinetic energy in a WD of density $n_{\rm ion} \sim 10^{31}$ cm^{-3} ($\approx 1.25\ M_\odot$), including the EM shower length (dashed). Any discontinuities in the stopping lengths are due to approximate analytic results in the different energy regimes. See Appendix B.1 for calculation details.

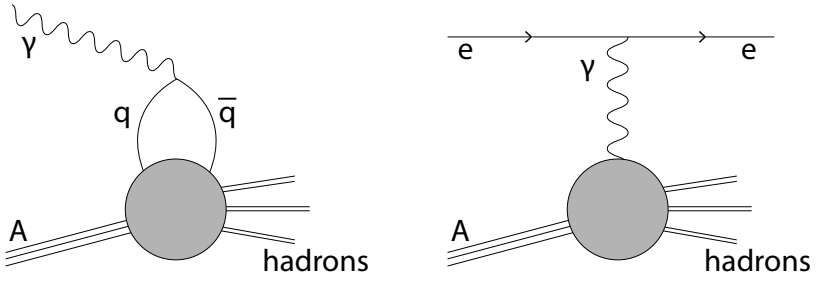

Figure 4.5: Photonuclear (left) and Electronuclear (right) interactions. The shaded region contains, at high energies, the familiar point-like processes of deep inelastic scattering and for energies below $\Lambda_{\rm QCD}$ is best described by exchange of virtual mesons.

radiation of virtual photons into hadronic showers. The stopping power is again radiative, which gives the constant stopping length

$$\lambda_{eA} \approx 10^{-4}\ \text{cm} \left(\frac{10^{32}\ \text{cm}^{-3}}{n_{\text{ion}}} \right). \tag{4.8}$$

This is suppressed by an additional factor of α relative to the photonuclear interaction, although a full calculation also yields an $\mathcal{O}(10)$ logarithmic enhancement. We see that the electronuclear length scale λ_{eA} is at most larger than the trigger size by an order of magnitude.

Electromagnetic Showers. Of course, electrons and photons can also shower through successive bremsstrahlung and pair-production. An electromagnetic shower proceeds until a critical energy ~ 100 MeV, at which point these radiative processes become subdominant to elastic Coulomb and Compton scattering. Below this scale radiation can still be important, though electromagnetic showers do not occur. Note that bremsstrahlung and pair-production are strictly forbidden for incident energies below the Fermi energy E_F.

At sufficiently high electron/photon energies and nuclear target densities, electromagnetic showers are elongated due to the Landau-Pomeranchuk-Migdal (LPM) effect. High-energy radiative processes necessarily involve small momentum transfers to nuclei. These soft virtual photons cannot be exchanged with only a single ion, but rather interact simultaneously with multiple ions. This generates a decoherence, suppressing bremsstrahlung/pair-production above an energy E_{LPM} which scales inversely with density:

$$E_{\text{LPM}} \approx 1\ \text{MeV} \left(\frac{10^{32}\ \text{cm}^{-3}}{n_{\text{ion}}} \right) \tag{4.9}$$

The corresponding shower lengths are

$$X_{\text{EM}} \approx X_0 \cdot \begin{cases} \left(\frac{\epsilon}{E_{\text{LPM}}} \right)^{1/2} & \epsilon > E_{\text{LPM}} \\ 1 & \epsilon < E_{\text{LPM}} \end{cases} \tag{4.10}$$

where

$$X_0 \approx 10^{-7}\ \text{cm} \left(\frac{10^{32}\ \text{cm}^{-3}}{n_{\text{ion}}} \right) \tag{4.11}$$

is the unsuppressed EM shower length. See Appendix B.1.3 for details. At the highest WD densities radiative processes are always LPM-suppressed, while at lower densities we observe both regimes. We emphasize that for all densities, throughout the energy range where it is relevant, the length of electromagnetic showers is never parametrically larger than the trigger size.

Neutrinos. Neutrinos scatter off nuclei with a cross section that increases with energy. In these interactions, an $\mathcal{O}(1)$ fraction of the neutrino energy is transferred to the nucleus with the rest going to produced leptons—this is sufficient to start a hadronic shower [95, 96]. At an energy of $\sim 10^{11}$ GeV, [95] calculates the neutrino-nuclear cross section to be $\sim 10^{-32}$ cm^2. Conservatively assuming this value for even higher energies, we find a neutrino mean free path in a WD of order ~ 10 cm. Therefore, any high-energy neutrino released in the WD will (on average) only interact after traveling a distance $\gg \lambda_T$. As per the discussion above, this makes the heating of a WD via the release of multiple neutrinos highly inefficient due to the (enormous) volume dilution factor in (4.3). Interestingly, a *single* high-energy neutrino with energy greater than $\mathcal{E}_{\rm boom}$ will still be able to efficiently heat the star and trigger a runaway. This is because the neutrino mean free path is simply a displacement after which a compact shower of size $X_{\rm had}$ occurs. If the energy contained in a single shower is large enough, then the heating caused by this single neutrino can effectively be considered as a separate and efficient heating event.

4.3.2 Low-Energy Elastic Heating

The showers of high-energy particles described above terminate in a cloud of low-energy $\epsilon \sim 10$ MeV neutrons, protons, and charged pions, and $\epsilon \sim 10 - 100$ MeV electrons and photons. Of course, particles at these energies may also be directly produced by the DM. At these energies, elastic nuclear, Coulomb, and Compton scatters dominate and eventually lead to the thermalization of ions. Once again, the physical expressions for all computed stopping powers and stopping lengths are given in Appendix B.1 whereas we simply quote the relevant numerical values here.

Hadrons. Neutral hadrons are the simplest species we consider, interacting at low-energies only through elastic nuclear scatters with cross section $\sigma_{\rm el} \approx 1$ b, where 1 b $= 10^{-24}$ cm^2. Note that the large ion mass requires $\sim 10 - 100$ hard scatters to transfer the hadron's energy in the form of a random-walk. This elastic heating range is

$$\lambda_{\rm el} \approx 10^{-7}\ {\rm cm} \left(\frac{10^{32}\ {\rm cm}^{-3}}{n_{\rm ion}} \right), \tag{4.12}$$

and is always less than the trigger size.

Charged hadrons are also subject to Coulomb interactions, which would provide the dominant stopping in terrestrial detectors. In this case, however, Coulomb scatters off degenerate WD electrons are strongly suppressed and charged hadrons predominantly undergo elastic nuclear scatters like their neutral brethren. This suppression is due to (1) motion of the electrons, which fixes the relative velocity to be $\mathcal{O}(1)$ and removes the enhancement of Coulomb stopping usually seen at low velocity, and (2) Pauli blocking, which forces the incident particle to scatter only electrons near the top of the Fermi sea. For an incident particle with velocity $v_{\rm in} \ll 1$, the first effect suppresses the stopping power by a factor of

$v_{\rm in}^2$ relative to that off stationary, non-degenerate electrons and the second by an additional factor of $v_{\rm in}$. Note that there is a small range of energies in which Coulomb scatters off ions dominate the stopping of charged hadrons—either way, both length scales are well below the trigger size.

Electrons and Photons. For electrons and photons below $\sim$ 100 MeV the dominant interactions are Coulomb scatters off WD electrons and Compton scatters, respectively. The length scale of these processes is smaller than any interaction with ions, and so these electrons and photons will thermalize into a compact electromagnetic "gas" with a size set by the radiative length scale $X_{\rm EM}$. The EM gas will cool and diffuse to larger length scales, eventually allowing thermalization with nuclei via the subdominant Coulomb scatters of electrons off ions. The photons of the EM gas will not undergo photonuclear showers here, as the gas will cool below $\sim$ 10 MeV by the time it diffuses out to a size $\lambda_{\gamma A}$. This gas temperature is initially at most $\sim$ 100 MeV. At these temperatures the heat capacity is dominated by photons, so as the gas diffuses to a size $\lambda_{\gamma A}$ it cools by a factor $(X_{\rm EM}/\lambda_{\gamma A})^{3/4} \sim 10^{-2}-10^{-1}$. Note that for temperatures T less than E_F, the electrons are partially degenerate and heating proceeds via the thermal tail with kinetic energies $\epsilon \sim E_F + T$. Therefore, the relevant thermalization process is Coulomb scattering of electrons off ions.

Like the hadronic elastic scatters, an electron Coulomb scattering off ions will occasionally hard scatter, and thus deposit its energy along a random walk. This reduces the stopping length at low energies, yielding

$$\lambda_{\rm coul} \approx 10^{-6}\ {\rm cm} \left(\frac{\epsilon}{10\ {\rm MeV}}\right)^{3/2} \left(\frac{10^{32}\ {\rm cm}^{-3}}{n_{\rm ion}}\right) \tag{4.13}$$

which is below the trigger size.

4.4 Dark Matter-Induced Ignition

Any DM interaction that produces SM particles in a WD has the potential to ignite the star, provided that sufficient SM energy is produced. The distribution in space, momentum, and species of these SM products is dependent on unknown DM physics and is needed to determine the rate of DM-induced ignition. This can be done precisely for a specific DM model, as we do for Q-balls in Section 4.6. In this Section, however, we study some general features of DM-WD encounters involving DM that possesses interactions with itself and the SM. We collect below the basic formulas relating DM model parameters to ignition criteria, SN rate, etc.

DM can generically heat a WD through three basic processes: DM-SM scattering, DM-DM collisions, and DM decays. For ultra-heavy DM, these processes can be complicated events involving many (possibly dark) final states, analogous to the interactions of heavy nuclei. In the case of DM-SM scattering, we consider both elastic and inelastic DM scatters

off WD constituents, e.g. carbon ions. We classify DM candidates into three types according to the interaction that provides the dominant source of heating, and refer to these as scattering, collision, and decay candidates. We also make the simplifying assumption that the above events are "point-like", producing SM products in a localized region (smaller than the heating length) near the interaction vertex. Where this is not the case (as in our elastic scattering and Q-ball constraints, see Sections 4.5.2 and 4.6), then the same formalism applies but with the event size added to the stopping length.

The SN rate may be greatly enhanced if DM is captured in the star, so we also consider separately "transiting DM" and "captured DM". In general, there is some loss of DM kinetic energy in the WD. In the transit scenario, this energy loss is negligible and the DM simply passes through the star. In the capture scenario, the energy loss is not directly capable of ignition but is sufficient to stop the DM and cause it to accumulate in the star. Energy loss may be due to a variety of processes, but for simplicity we will focus on an DM-nuclei elastic scattering. Of course, due to the velocity spread of DM in the rest frame of a WD, there will necessarily be both transiting and captured DM populations in the star.

4.4.1 DM Transit

DM-SM Scattering. Runaway fusion only occurs in the degenerate WD interior where thermal expansion is suppressed as a cooling mechanism. The outer layers of the WD, however, are composed of a non-degenerate gas and it is therefore essential that a DM candidate penetrate this layer in order to ignite a SN. We parameterize this by a DM stopping power $(dE/dx)_{\rm SP}$, the kinetic energy lost by the DM per distance traveled in the non-degenerate layer, and demand that

$$\left(\frac{dE}{dx}\right)_{\rm SP} \ll \frac{m_\chi v_{\rm esc}^2}{R_{\rm env}}, \tag{4.14}$$

where $R_{\rm env}$ is the nominal size of the non-degenerate WD envelope and $v_{\rm esc} \sim 10^{-2}$ is the escape velocity of the WD, at which the DM typically transits the star.

DM-SM scattering will result in a continuous energy deposit along the DM trajectory (if the interaction is rare enough for this not to be true, then the encounter is analogous to the case of DM decay). This is best described by a linear energy transfer $(dE/dx)_{\rm LET}$, the kinetic energy of SM particles produced per distance traveled by the DM. If these products have a heating length L_0 then the energy deposit must at minimum be taken as the energy transferred along a distance L_0 of the DM trajectory. Importantly, as per the ignition condition (4.3), such a deposition is *less* explosive unless L_0 is smaller than the trigger size λ_T. We thus consider the energy deposited over the larger of these two length scales. Assuming the energy of the DM is roughly constant during this heating event, the ignition condition is:

$$\left(\frac{dE}{dx}\right)_{\rm LET} \gtrsim \frac{\mathcal{E}_{\rm boom}}{\lambda_T} \cdot \max\left\{\frac{L_0}{\lambda_T}, 1\right\}^2. \tag{4.15}$$

Note that the DM stopping power $(dE/dx)_{\rm SP}$ and the linear energy transfer $(dE/dx)_{\rm LET}$ are related in the case of elastic scatters, but in general the two quantities may be controlled by different physics. In addition, a transit event satisfying condition (4.14) will have negligible energy loss over the parametrically smaller distances λ_T or L_0, validating (4.15).

The above condition sums the individual energy deposits along the DM trajectory as though they are all deposited simultaneously. This is valid if the DM moves sufficiently quickly so that this energy does not diffuse out of the region of interest before the DM has traversed the region. We therefore require that the diffusion time $\tau_{\rm diff}$ across a heated region of size L at temperature T_f be larger than the DM crossing-time:

$$\tau_{\rm diff} \sim \frac{L^2}{\alpha(T_f)} \gg \frac{L}{v_{\rm esc}}, \tag{4.16}$$

where $\alpha(T)$ is the temperature-dependent diffusivity. This condition is more stringent for smaller regions, so we focus on the smallest region of interest, $L = \lambda_T$. Then (4.16) is equivalent to demanding that the escape speed is greater than the conductive speed of the fusion wave front, $v_{\rm cond} \sim \alpha(T_f)/\lambda_T$. Numerical calculations of $v_{\rm cond}$ are tabulated in [88], and indeed condition (4.16) is satisfied for all WD densities.

The rate of transit events is directly given by the flux of DM through a WD

$$\Gamma_{\rm trans} \sim \frac{\rho_\chi}{m_\chi} R_{\rm WD}^2 \left(\frac{v_{\rm esc}}{v_{\rm halo}}\right)^2 v_{\rm halo}, \tag{4.17}$$

where ρ_χ is the DM density in the region of the WD, and $R_{\rm WD}$ is the WD radius. Here $v_{\rm halo} \sim 10^{-3}$ is the virial velocity of our galactic halo. Note the $(v_{\rm esc}/v_{\rm halo})^2 \sim 100$ enhancement due to gravitational focusing.

We will not consider here captured DM that heats the star via scattering events, as such heating will typically cause ignition before capture occurs. However, it is possible to cause ignition after capture if the collection of DM leads to an enhanced scattering process.

DM-DM Collisions and DM Decays. For a point-like DM-DM collision or DM decay event releasing particles of heating length L_0, ignition will occur if the total energy in SM products satisfies condition (4.3). Such an event will likely result in both SM and dark sector products, so we parameterize the resulting energy in SM particles as a fraction $f_{\rm SM}$ of the DM mass. For non-relativistic DM, the DM mass is the dominant source of energy and therefore $f_{\rm SM} \lesssim 1$ regardless of the interaction details. A single DM-DM collision or DM decay has an ignition condition:

$$m_\chi f_{\rm SM} \gtrsim \mathcal{E}_{\rm boom} \cdot \max\left\{\frac{L_0}{\lambda_T}, 1\right\}^3. \tag{4.18}$$

Thus the WD is sensitive to annihilations/decays of DM masses $m_\chi \gtrsim 10^{16}$ GeV.

DM that is not captured traverses the WD in a free-fall time $t_{\rm ff} \sim R_{\rm WD}/v_{\rm esc}$, and the rate of DM-DM collisions within the WD parameterized by cross section $\sigma_{\chi\chi}$ is:

$$\Gamma_{\rm SN}^{\rm ann} \sim \left(\frac{\rho_\chi}{m_\chi}\right)^2 \sigma_{\chi\chi} \left(\frac{v_{\rm esc}}{v_{\rm halo}}\right)^3 v_{\rm halo} R_{\rm WD}^3. \tag{4.19}$$

Similarly the net DM decay rate inside the WD parameterized by a lifetime τ_χ is:

$$\Gamma_{\rm SN}^{\rm decay} \sim \frac{1}{\tau_\chi}\frac{\rho_\chi}{m_\chi} \left(\frac{v_{\rm esc}}{v_{\rm halo}}\right) R_{\rm WD}^3. \tag{4.20}$$

4.4.2 DM Capture

Review of DM Capture. We first summarize the capture and subsequent evolution of DM in the WD, ignoring annihilations or decays—see Appendix B.2 for details. Consider a spin-independent, elastic scattering off carbon ions with cross section $\sigma_{\chi A}$. The rate of DM capture in gravitating bodies is of course very well-studied [97, 98]. However, this rate must be modified when the DM requires multiple scatters to lose the necessary energy for capture. Ultimately, for ultra-heavy DM the capture rate is of the form

$$\Gamma_{\rm cap} \sim \Gamma_{\rm trans} \cdot \min\left\{1, \overline{N}_{\rm scat} \frac{m_{\rm ion} v_{\rm esc}^2}{m_\chi v_{\rm halo}^2}\right\}, \tag{4.21}$$

where $\overline{N}_{\rm scat} \sim n_{\rm ion}\sigma_{\chi A} R_{\rm WD}$ is the average number of DM-carbon scatters during one DM transit. For the remainder of this Section, all results are given numerically assuming a WD central density $n_{\rm ion} \sim 10^{31}$ cm^{-3}. The relevant parametric expressions are presented in further detail in Appendix B.2.

Once DM is captured, it eventually thermalizes with the stellar medium at velocity $v_{\rm th} \sim (T_{\rm WD}/m_\chi)^{1/2}$, where $T_{\rm WD}$ is the WD temperature. The dynamics of this process depend on the strength of the DM-carbon interaction, namely on whether energy loss to carbon ions provides a small perturbation to the DM's gravitational orbit within the star or whether DM primarily undergoes Brownian motion in the star due to collisions with carbon. For simplicity, we will focus here only on the former case, corresponding roughly to interactions

$$\sigma_{\chi A} \lesssim \frac{m_\chi}{\rho_{\rm WD} R_{\rm WD}} \sim 10^{-26}\ {\rm cm}^2 \left(\frac{m_\chi}{10^{16}\ {\rm GeV}}\right) \tag{4.22}$$

where the DM is able to make more than a single transit through the star before thermalizing. Note that the opposite regime indeed also provides constraints on captured DM and is unconstrained by other observations, see Figure 4.11, however the resulting limits are similar to those presented here.

In the limit (4.22), captured DM will thermalize by settling to a radius $R_{\rm th}$ given by the balance of gravity and the thermal energy $T_{\rm WD}$,

$$R_{\rm th} \approx 0.1\ {\rm cm} \left(\frac{m_\chi}{10^{16}\ {\rm GeV}}\right)^{-1/2}. \tag{4.23}$$

This settling proceeds in two stages. Captured DM will initially be found on a large, bound orbit that exceeds the size of the WD, decaying after many transits of the star until the orbital size is fully contained within the WD. This occurs after a time

$$t_1 \approx 7 \times 10^{16}\ \mathrm{s} \left(\frac{m_\chi}{10^{16}\ \mathrm{GeV}}\right)^{3/2} \left(\frac{\sigma_{\chi A}}{10^{-35}\ \mathrm{cm}^2}\right)^{-3/2}. \tag{4.24}$$

The DM then completes many orbits within the star until its orbital size decays to the thermal radius, occurring after a further time

$$t_2 \approx 10^{14}\ \mathrm{s} \left(\frac{m_\chi}{10^{16}\ \mathrm{GeV}}\right) \left(\frac{\sigma_{\chi A}}{10^{-35}\ \mathrm{cm}^2}\right)^{-1}. \tag{4.25}$$

Note that the difference in scalings between t_1 and t_2 is due to the fact that, while the two times are ultimately determined by scattering in the star, the dynamics of the settling DM are quite distinct in each case. t_1 is dominated by the time spent on the largest orbit outside the WD (which additionally depends on $\sigma_{\chi A}$) while t_2 is dominated by the time spent near the thermal radius. Subsequently the DM will begin steadily accumulating at R_{th}, with the possibility of self-gravitational collapse if the collected mass of DM exceeds the WD mass within this volume. This occurs after a time

$$t_{\mathrm{sg}} \approx 10^{9}\ \mathrm{s} \left(\frac{m_\chi}{10^{16}\ \mathrm{GeV}}\right)^{-1/2} \left(\frac{\sigma_{\chi A}}{10^{-35}\ \mathrm{cm}^2}\right)^{-1}. \tag{4.26}$$

Of course, not all of these stages may be reached within the age of the WD τ_{WD}. The full time to collect and begin self-gravitating is $t_1 + t_2 + t_{\mathrm{sg}}$.

At any point during the above evolution, captured DM has the potential to trigger a SN. We will consider ignition via either the decay or annihilation of captured DM. Of particular interest are events occurring within a collapsing DM core, as such cores have the additional ability to ignite a WD for DM masses less than $\mathcal{E}_{\mathrm{boom}}$, either via multiple DM annihilations or by the formation of a black hole. This is the focus of forthcoming work [99]. In the following, we restrict attention to the limit (4.22) and require DM masses sufficiently large so that a single collision or decay will ignite the star, and give only a quick assessment of DM core collapse.

Captured DM-DM Collisions. We now turn to the rate of DM-DM collisions for captured DM. Of course, the thermalizing DM constitutes a number density of DM throughout the WD volume. Assuming that $t_1 + t_2 < \tau_{\mathrm{WD}}$, the total rate of annihilations for this "in-falling" DM is peaked near the thermal radius and is of order:

$$\Gamma_{\mathrm{infall}} \sim \frac{(\Gamma_{\mathrm{cap}} t_2)^2}{R_{\mathrm{th}}^3} \sigma_{\chi\chi} v_{\mathrm{th}}. \tag{4.27}$$

If $\Gamma_{\mathrm{infall}} t_2 > 1$, then a SN will be triggered by the in-falling DM population. Otherwise if $\Gamma_{\mathrm{infall}} t_2 < 1$, the DM will start accumulating at the thermal radius. If $t_{\mathrm{sg}} \ll t_2$ (as expected

for such heavy DM masses) there will be no collisions during this time and thus a collapse will proceed. For a DM sphere consisting of N particles at a radius r, the rate of annihilations is

$$\Gamma_{\text{collapse}} \sim \frac{N^2}{r^3}\sigma_{\chi\chi}v_\chi, \tag{4.28}$$

$$v_\chi \sim \sqrt{\frac{GNm_\chi}{r}}. \tag{4.29}$$

Of course, there may be some stabilizing physics which prevents the DM from collapsing and annihilating below a certain radius, such as formation of a black hole or bound states. To illustrate the stringent nature of the collapse constraint we will simply assume some benchmark stable radius, as in Figure 4.9. We assume that the timescale for collapse at this radius is set by DM cooling t_{cool}, which is related to t_2. Note that if a single collision has not occurred during collapse, one may additionally examine annihilations of the subsequent in-falling DM down to the stable radius—for simplicity, we do not consider this scenario.

Captured DM Decays. Lastly, we compute the rate of decays for captured DM, which is simply proportional to the number of DM particles in the WD available for decay at any given instance. In the transit scenario (4.20), this rate is $\Gamma \sim \tau_\chi^{-1}\Gamma_{\text{trans}}t_{\text{ff}}$. In the capture scenario, this number is instead determined by the thermalization time within the WD $\Gamma \sim \tau_\chi^{-1}\Gamma_{\text{cap}}t_2$, conservatively assuming that after a thermalization time, the DM quickly collapses and stabilizes to an "inert" core incapable of further decay. If this is not the case, then the captured DM decay rate is given by $\Gamma \sim \tau_\chi^{-1}\Gamma_{\text{cap}}\tau_{\text{WD}}$.

4.5 Dark Matter Constraints

We now constrain some generic DM candidates which will ignite a WD via one of the processes parameterized in Section 4.4. These release SM particles that deposit their energy and thermalize ions within a distance described in Section 4.3. First, however, we review how WD observables constrain DM candidates capable of triggering SN.

4.5.1 Review of WD Observables

Following the discussion of [77], our constraints come from (1) the existence of heavy, long-lived white dwarfs, or (2) the measured type Ia SN rate. The ages of WD can be estimated by measuring their temperature and modeling their cooling over time. This has been extensively studied, see for example [100], and it is found that typical age of an old WD is of order $\sim 1\,\text{Gyr}$. RX J0648.04418 is one such nearby star and one of the heavier known WDs, with a mass $\sim 1.25\,M_\odot$ [101] and local dark matter density which we take to be $\rho_\chi \sim 0.4\,\text{GeV/cm}^3$. Of course, this is not the only known heavy WD—the Sloan Digital Sky Survey [102] has found 20+ others. The NuStar collaboration has also recently uncovered evidence for the likely existence of heavy WDs near the galactic center [103], where the DM density is assumed

to be much greater $\rho_\chi \gtrsim 10^3$ GeV/cm^3 [104]. Such heavy candidates are particularly suited for our constraints as the energy deposit necessary to trigger SN (4.3) is a decreasing function of WD mass. However, less dense white dwarfs are significantly more abundant in the galaxy. Thus, even if a sufficiently massive DM is unable to trigger a violent heating event within the lifetime of a WD, it could still ignite enough lighter WDs to affect the measured SN rate of ~ 0.3 per century. The DM-induced SN rate is estimated using the expected number of white dwarfs per galaxy $\sim 10^{10}$ and their mass distribution [102]. Simulations indicate that only WD masses heavier than $\sim 0.85\ M_\odot$ will result in optically visible SN [77]. Therefore, most of the stars exploded in this manner will be in the mass range $\sim 0.85 - 1\ M_\odot$, resulting in weaker SN than expected of typical Chandrasekhar mass WDs.

To summarize, a bound on DM parameters can be placed if either a single explosive event occurs during the lifetime of an observed star such as RX J0648.04418, or the SN rate due to such DM events throughout the galaxy exceeds the measured value. Note that for low-mass WDs dominated by photon diffusion, $\mathcal{E}_{\rm boom}$ is a strong function of WD density. The average density for WDs is typically a factor $\sim 10^{-2} - 10^{-1}$ less than the central density, although it is found that the WD density only changes by an $\mathcal{O}(1)$ fraction from the central value up to a distance $\sim R_{\rm WD}/2$ [105]. Therefore the central density is a valid approximation as long as we consider heating events within this "modified" WD volume. For simplicity, we employ this approach.

4.5.2 Scattering Constraints

In order to constrain a DM model with a scattering interaction, we require that it satisfy the ignition condition (4.15). This is given in terms of an LET, which parameterizes the ability for DM to release sufficient energy to the star in the form of SM particles. Here we consider a DM elastic scattering off carbon ions with cross section $\sigma_{\chi A}$, which has an LET:

$$\left(\frac{dE}{dx}\right)_{\rm LET} \sim n_{\rm ion}\sigma_{\chi A} m_{\rm ion} v_{\rm esc}^2. \tag{4.30}$$

This can be expressed in terms of the cross section per nucleon $\sigma_{\chi n}$—see Appendix B.2 Each elastic scatter transfers an energy of order $m_{\rm ion} v_{\rm esc}^2 \approx 1 - 10$ MeV to the target nuclei, thus enabling fusion reactions. Note that the stopping power of the DM in the non-degenerate envelope is of the same form, but with the density replaced by its diminished value in this region. It is interesting that combining the ignition condition (4.15) with the requirement that the DM adequately penetrates the non-degenerate layer (4.14) yields a lower bound on DM mass.

$$m_\chi > \mathcal{E}_{\rm boom}\left(\frac{R_{\rm env}}{\lambda_T}\right)\left(\frac{\rho_{\rm env}}{\rho_{\rm WD}}\right)\frac{1}{v_{\rm esc}^2}, \tag{4.31}$$

where $\rho_{\rm WD}$ is the central density of the WD. Here $R_{\rm env} \approx 50$ km is the width of a non-degenerate WD envelope—the density in this region $\rho_{\rm env}$ is typically a small fraction $\sim 10^{-3}$

of the central density [106]. We conservatively take the envelope to be composed of carbon ions; if it were primarily hydrogen or helium, then the condition for penetration is weakened by 4 orders of magnitude due to the reduced energy transfer and cross section for scattering. We find that the DM must be heavier than $\sim 10^{28}$ GeV to ensure an explosive transit of a 1.25 $M_\odot$ WD *and* minimal loss of kinetic energy in the non-degenerate layer. For the sake of comparison this corresponds to a macroscopic DM mass of order ~ 20 kg.

Of course, this bound is only applicable if the energy input to the WD is solely coming from DM kinetic energy. We may also consider DM inelastic scattering off carbon ions which transfer more than $\sim$ MeV per collision. Examples of such a process include baryon-number violating interactions which can release the nucleon mass energy $\sim$ GeV per collision. This is similar to Q-balls, which absorb the baryon number of nuclear targets and liberate binding energy rather than transferring kinetic energy—this interaction is examined in Section 4.6. Note that the assumption of a "point-like" interaction requires that the physical size of the DM is much smaller than λ_T—this is sensible up to masses of order $\sim 10^{47}$ GeV, at which point the gravitational radius of the DM exceeds λ_T.

In Figure 4.6 we constrain the DM elastic scattering cross section per nucleon $\sigma_{\chi n}$ as a function of DM mass m_χ using the different classes of observables described above. Note that the scattering cross sections constrained here are incredibly large $\gtrsim 10^{-10}$ cm^2—however, the constraints from WDs reach to very large masses for which no other constraints exist. At these masses, the most stringent limits on DM elastic scattering are from CMB and Lyman-α spectrum analysis [107], which constrain $\frac{\sigma_{\chi n}}{m_\chi} < \frac{10^{-3}\text{b}}{\text{GeV}}$. These cross sections also require that the DM involved be macroscopically large, of order or larger than the trigger size, and so the interaction is decidedly not "point-like." This fact does not weaken our constraints, however, since the energy transferred to each ion in the DM's path is greater than $\sim$ MeV.

4.5.3 Collision and Decay Constraints

In order to constrain a DM model through its annihilations or decays within a WD, we require that it satisfy the ignition condition (4.18). Consider a single annihilation or decay with $f_{\text{SM}} = 1$ that releases a spectrum of SM particles. As shown in Section 4.3, the constraint has minimal dependence on the released species if the typical energy ϵ of secondary products is greater than an MeV. In the case of neutrinos, we may simply demand that ϵ is sufficiently large that a single neutrino can ignite the star. With this schematic for the DM interaction, we can constrain the cross section for collision $\sigma_{\chi\chi}$ and lifetime τ_χ. This is done in Figures 4.7 and 4.8 in the case of transiting DM using the different classes of observables for DM-DM collisions and DM decays, respectively.

Of course there are existing limits on DM annihilations and decays, complementary to the ones placed from WDs. DM annihilations/decays inject energy and affect the ionization history of our universe, which can be probed by measurements of the CMB temperature and polarization angular spectrum [110, 108, 109]. These constraints are of order $\sigma_{\chi\chi} v < 10^{-27}\ \frac{\text{cm}^3}{\text{s}} \left(\frac{m_\chi}{10\ \text{GeV}}\right)$ for annihilations, and $\tau_\chi > 10^7$ Gyr for decay. There are also constraints

on DM annihilation/decays in our halo from the cosmic ray (CR) flux seen in large terrestrial detectors. Here we provide a crude estimate of the expected constraints from CRs in the case of DM annihilation (decays are qualitatively similar). A more detailed analysis is beyond the scope of this work. The Pierre Auger Observatory [111] has detected the flux of $E_{\rm th} \sim 10^{11}$ GeV cosmic rays with an exposure of order $A_{\rm PA} \sim 40000$ km^2 sr yr. Ultra-heavy DM annihilations $m_\chi > 10^{16}$ GeV will generally produce secondary particles of energy $\epsilon \gtrsim E_{\rm th}$ via final-state radiation. For a simple 2-2 process (e.g. $\chi\chi \to qq$), the expected number of final-state particles radiated at $E_{\rm th}$ due to QCD showers is approximated by the Sudakov double logarithm

$$N_{\rm rad} \sim \frac{4\alpha_s}{\pi} \log\left(\frac{m_\chi}{\Lambda_{\rm QCD}}\right) \log\left(\frac{m_\chi}{E_{\rm th}}\right) \approx 100, \tag{4.32}$$

where α_s is the QCD coupling constant. Similarly, the estimated number of final-state particles at $E_{\rm th}$ due to EW showers is ≈ 50. We expect that CRs at this energy originating in our galaxy will be able to strike the earth unattenuated. Thus, such events would affect the measured CR flux of Pierre Auger unless

$$\left(\frac{\rho_\chi}{m_\chi}\right)^2 \sigma_{\chi\chi} v \frac{R_{\rm halo}}{4\pi} N_{\rm rad} \times A_{\rm PA} \lesssim 1. \tag{4.33}$$

Here we assume an average value for DM density $\rho_\chi \approx 0.4$ GeV/cm^3 as a reasonable approximation to the integral over our galactic halo volume. Surprisingly, the above CR constraints are (within a few orders of magnitude) comparable to the constraints due to the observation of long-lived WDs. This is actually due to a coincidence in the effective "space-time volumes" of the two systems. A terrestrial CR detector such as Pierre Auger sees events within a space-time volume ($R_{\rm det}^2 R_{\rm halo} \times t_{\rm det}$), where $R_{\rm det} \sim 50$ km, $R_{\rm halo} \sim 10$ kpc, and $t_{\rm det} \sim 10$ yr. This is similar in magnitude to the WD space-time volume ($R_{\rm WD}^3 \times \tau_{\rm WD}$).

In the case of captured DM, we show the constraints on $\sigma_{\chi\chi}$ and τ_χ assuming a benchmark value of the elastic scattering cross section $\sigma_{\chi n} = 10^{-32}$ cm^2. With regards to DM-DM collisions, we also assume a stabilizing radius for the collapsing DM sphere. This is done in Figures 4.9 and 4.10—for simplicity, here we only show the constraints from the existence of nearby, heavy WDs.

It is important to note that there is a large parameter space in $\sigma_{\chi n}$ which will lead to DM capture, thermalization, and core collapse in a WD. This is depicted in Figure 4.11, along with the existing constraints on DM elastic scattering. As detailed in [112], direct detection experiments such as Xenon 1T [113] are only sensitive to DM masses $m_\chi < 10^{17}$ GeV. For even larger masses $m_\chi < 10^{26}$ GeV there are constraints from the MACRO experiment [114] and from ancient excavated mica. The latter has been studied in [115]. We have similarly estimated the bounds from MACRO assuming a detectable threshold of ~ 5 MeV/cm [114].

4.6 Q-balls

Having derived constraints on generic models of ultra-heavy DM, we turn towards a concrete example. In various supersymmetric extensions of the SM, non-topological solitons called Q-balls can be produced in the early universe [116, 117]. If these Q-balls were stable, they would comprise a component of the DM today. For gauge-mediated models with flat scalar potentials, the Q-ball mass and radius are given by

$$M_Q \sim m_S Q^{3/4}, \quad R_Q \sim m_S^{-1} Q^{1/4}, \tag{4.34}$$

where m_S is related to the scale of supersymmetry breaking, and Q is the global charge of the Q-ball—in our case, baryon number. The condition $M_Q/Q < m_p$ ensures that the Q-ball is stable against decay to nucleons. The interaction of relic Q-balls with matter depends on its ability to retain electric charge [118]. We restrict our attention to electrically neutral Q-balls, which induce the dissociation of incoming nucleons and in the process absorb their baryonic charge. During this proton decay-like process, excess energy of order $\Lambda_{\rm QCD}$ is released via the emission of 2–3 pions. We assume that for each Q-ball inelastic collision, there is equal probability to produce π^0 and $\pi^\pm$ under the constraint of charge conservation. The cross section for this interaction is approximately geometric

$$\sigma_Q \sim \pi R_Q^2, \tag{4.35}$$

and thus grows with increasing Q. Note that a sufficiently massive Q-ball will become a black hole if $R_Q \lesssim G M_Q$. In the model described above, this translates into a condition $(M_{\rm pl}/m_S)^4 \lesssim Q$.

We now determine the explosiveness of a Q-ball transit. This process is described by a linear energy transfer

$$\left(\frac{dE}{dx}\right)_{\rm LET} \sim n_{\rm ion} \sigma_Q N_\pi \epsilon, \tag{4.36}$$

where the nuclear interaction results in $N_\pi \approx 30$ pions released, each with kinetic energy $\epsilon \approx 500$ MeV. These pions induce hadronic showers which terminate in low-energy hadrons that rapidly transfer their energy to ions via elastic scatters, as discussed in Section 4.3. The pions have a heating length $X_{\rm had} \lesssim \lambda_T$; however, we will see the Q-ball has a finite size $R_Q \gtrsim X_{\rm had}$ in the region we are able to constrain. So, as mentioned in Section 4.4, we take the heating length to be $L_0 \sim R_Q + X_{\rm had} \sim R_Q$. The ignition condition is then given by equations (4.15) and (4.36):

$$R_Q^2 \gtrsim \frac{1}{n_{\rm ion}} \frac{\mathcal{E}_{\rm boom}}{\lambda_T} \max\left\{\frac{R_Q}{\lambda_T}, 1\right\}^2 \left(\frac{1}{10\ \text{GeV}}\right). \tag{4.37}$$

This implies $\sigma_Q \gtrsim 10^{-12}$ cm^2 is sufficient to ignite a 1.25 $M_\odot$ WD, which corresponds to a charge $Q \gtrsim 10^{42}\ (m_S/\text{TeV})^4$. Note that for sufficiently large Q, the radius will grow larger than λ_T. This situation still results in ignition, however, as the energy ~ 10 GeV released

per ion is much larger than the $\sim$ MeV needed per ion for fusion. Note finally that the Q-ball interaction described above results in minimal slowing for Q-balls this massive, so transits will easily penetrate the non-degenerate WD envelope (4.14).

The existing limits on Q-balls primarily come from Super-Kamiokande and air fluorescence detectors of cosmic rays (OA, TA) [119]. However, the constraints that come from considering the ignition of WDs are in a fundamentally new and complementary region of parameter space. These are plotted in Figure 4.13. We have also included the constraints that result from gravitational heating of a WD during a Q-ball transit, as in [77].

4.7 Discussion

The detection of ultra-heavy DM is an open problem which will likely require a confluence of astrophysical probes. Here we present a guide to constraining these candidates through DM-SM scatters, DM-DM annihilations, and DM decays inside a WD that release sufficient SM energy to trigger runaway fusion. In particular, we calculate the energy loss of high-energy particles due to SM interactions within the WD medium and determine the conditions for which a general energy deposition will heat a WD and ignite SN. Ultra-heavy DM that produces greater than 10^{16} GeV of SM particles in a WD is highly constrained by the existence of heavy WDs and the measured SN rate. The formalism provided will enable WDs to be applied as detectors for any DM model capable of heating the star through such interactions. We have done so for baryonic Q-balls, significantly constraining the allowed parameter space in a complementary way to terrestrial searches.

We have explored briefly the application of this WD instability to self-gravitational collapse of DM cores, which has very interesting possibilities. The decay or annihilation of DM which is captured by a WD and forms a self-gravitating core is highly constrained for DM with mass greater than 10^{16} GeV. In addition, such collapsing cores can provide enough heating via multiple annihilations to ignite the star for much smaller DM masses than those considered here, e.g. 10^7 GeV, and can induce SN through other means such as the formation and evaporation of mini black holes. These will be addressed in future work [99].

Finally, in addition to the constraints mentioned above, the general phenomenology of these DM-induced runaways will be the ignition of sub-Chandrasekhar mass WDs, possibly with no companion star present. Some of the mechanisms considered above are also likely to initiate fusion far from the center of the star. This is in contrast with conventional single-degenerate and double-degenerate mechanisms, which require a companion star and ignite fusion near the center of a super-Chandrasekhar mass WD [78]. This raises the tantalizing possibility that DM encounters with WDs provide an alternative explosion mechanism for type Ia SN or similar transient events, and that these events may be distinguishable from conventional explosions. Understanding and searching for possible distinguishing features of DM-induced events is an important follow-up work.

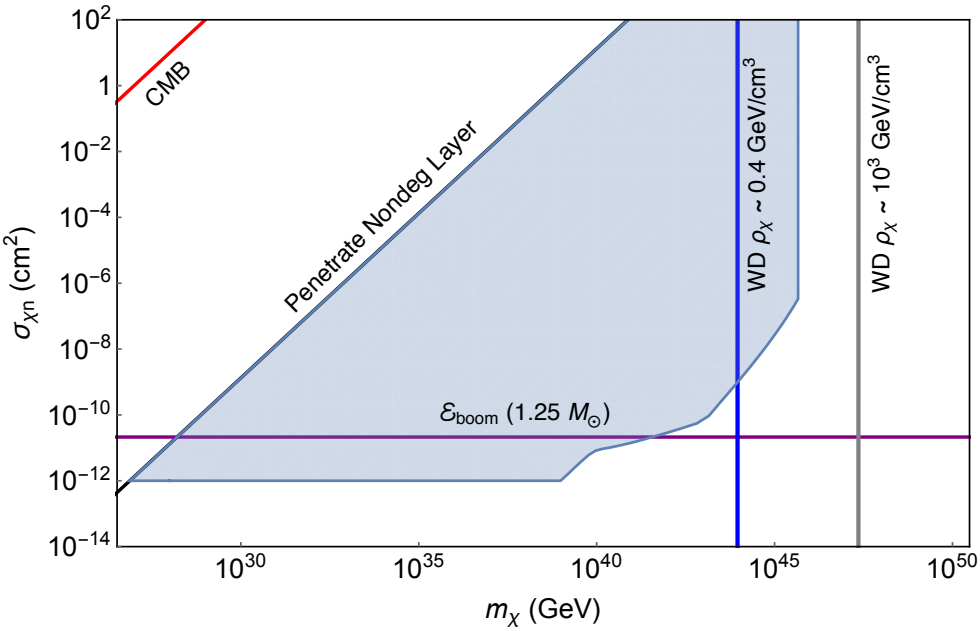

Figure 4.6: Constraints on DM-carbon elastic scattering cross section. Bounds come from demanding that the DM transit triggers runaway fusion (4.15) and occurs at a rate (4.17) large enough to either ignite a 1.25 $M_\odot$ WD in its lifetime or exceed the measured SN rate in our galaxy (blue shaded). We also demand that the DM penetrates the non-degenerate stellar envelope, taken at the highest densities, without losing appreciable kinetic energy. Constraints from the CMB/large-scale structure [107] are depicted as well.

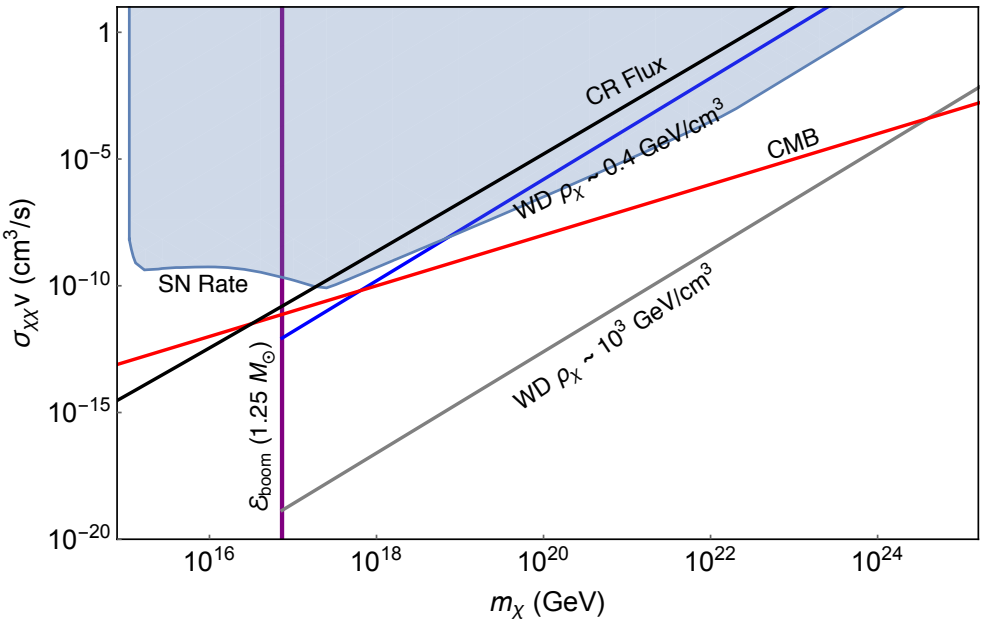

Figure 4.7: Constraints on DM-DM collision cross section to SM products of energy $\epsilon \gg$ MeV. Bounds come from demanding that the DM transit interaction triggers runaway fusion (4.18) and occurs at a rate (4.19) large enough to either ignite an observed 1.25 $M_\odot$ WD in its lifetime or exceed the measured SN rate in our galaxy (blue shaded). Also shown are the CMB [108] (red) and CR flux (black) constraints on DM annihilations.

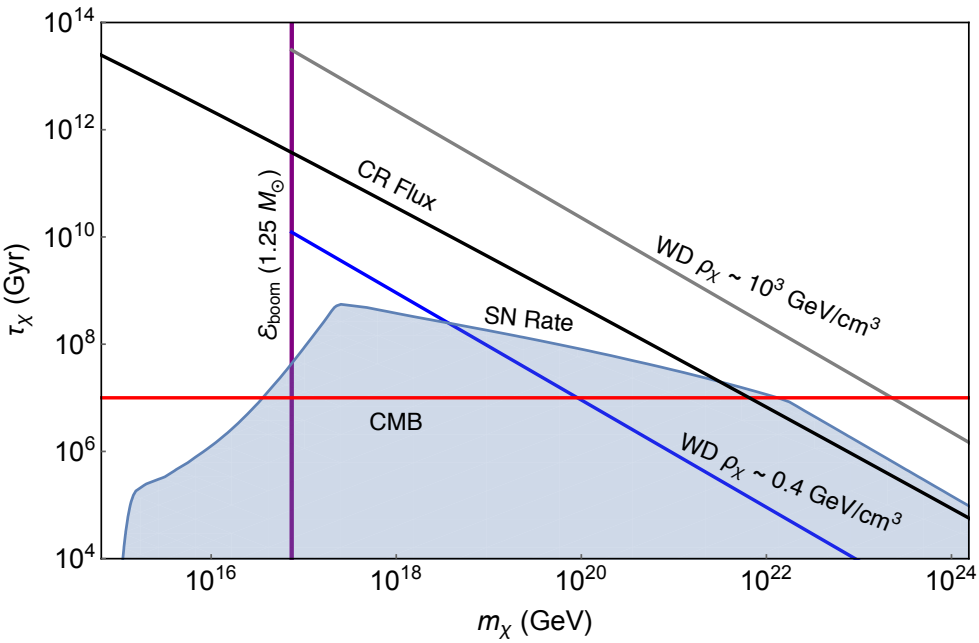

Figure 4.8: Constraints on DM decay to SM products of energy $\epsilon \gg$ MeV. Bounds come from demanding that the DM transit interaction triggers runaway fusion (4.18) and occurs at a rate (4.20) large enough to either ignite an observed 1.25 $M_\odot$ WD in its lifetime or exceed the measured SN rate in our galaxy (blue shaded). Also shown are the CMB [109] (red) and CR flux (black) constraints on DM lifetime.

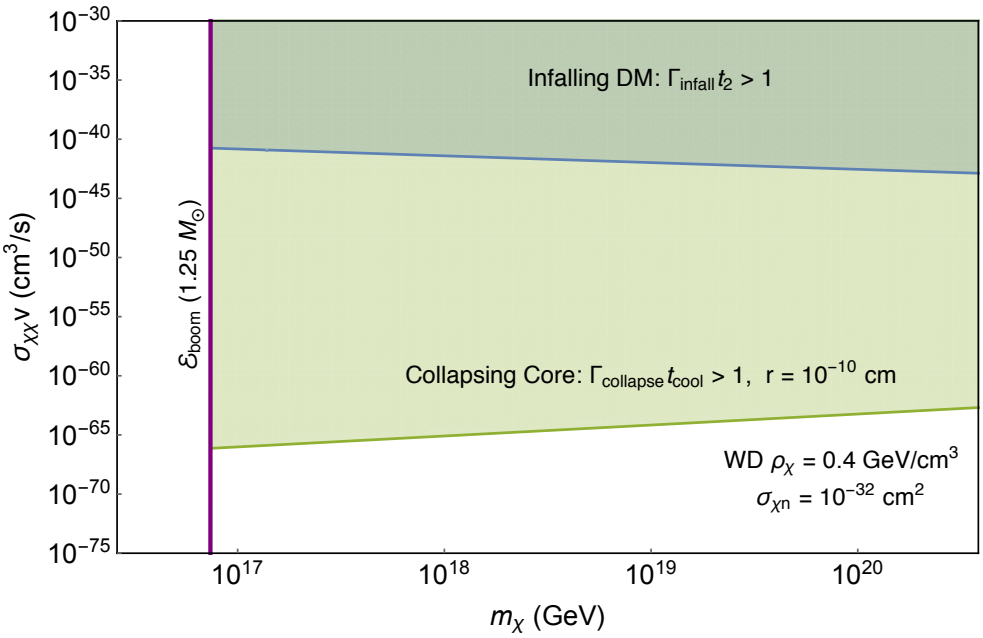

Figure 4.9: Constraints on DM-DM collision cross section to SM products of energy $\epsilon \gg$ MeV, assuming DM is captured with an elastic scattering cross section $\sigma_{\chi n} = 10^{-32}$ cm^2. Bounds come from the observation of 1.25 $M_\odot$ WDs in local DM density. We consider the annihilation rate during the in-falling thermalization stage (4.27) (blue shaded) and during self-gravitational collapse (4.28) to a stable radius $r = 10^{-10}$ cm (green shaded). See text for details.

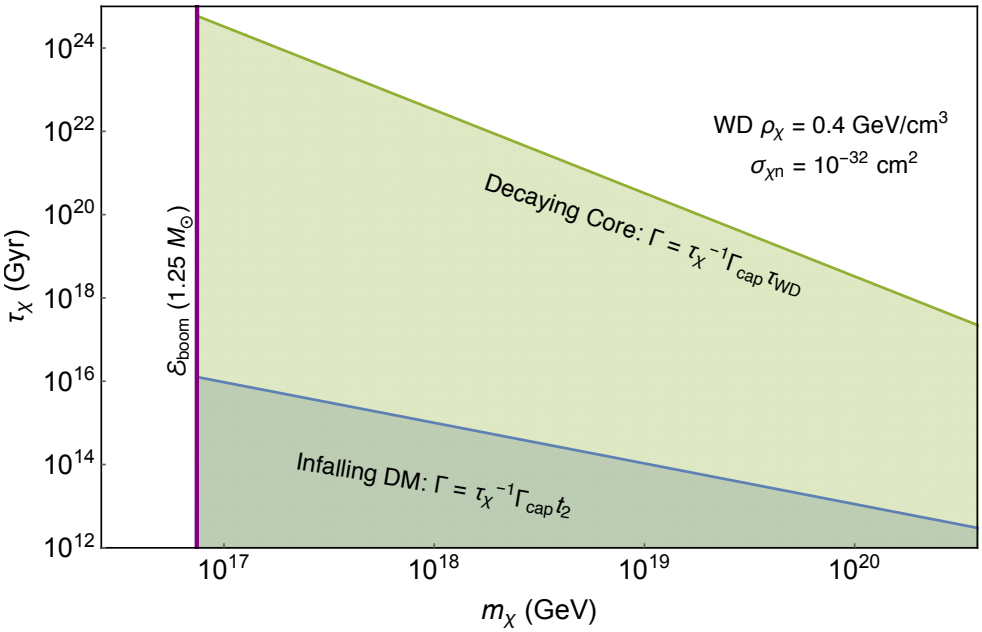

Figure 4.10: Constraints on DM decay to SM products of energy $\epsilon \gg$ MeV, assuming DM is captured with an elastic scattering cross section $\sigma_{\chi n} = 10^{-32}$ cm^2. Bounds come from the observation of 1.25 $M_\odot$ WDs in local DM density. We consider the rate of decays during the in-falling thermalization stage (blue shaded) and for a decaying DM core (green shaded). See text for details.

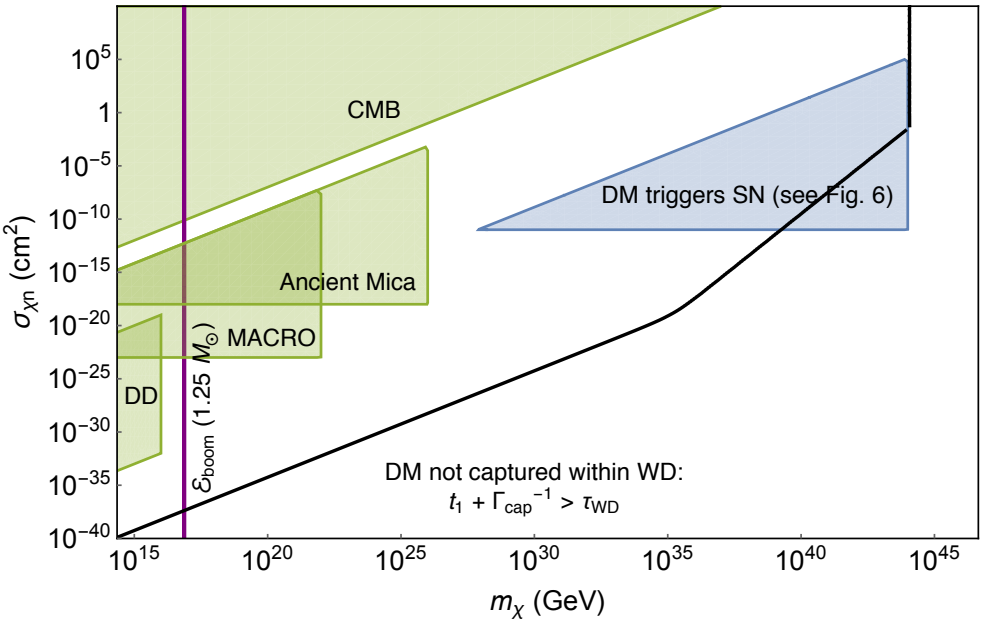

Figure 4.11: Viable parameter space (above the black line) in which DM-nucleon elastic scattering leads to DM capture in a 1.25 $M_\odot$ WD. All of this space is subject to constraints on DM decay and DM-DM annihilation analogous to those given in Figures 4.10 and 4.9. Note the blue region, reproducing Figure 4.6, indicates DM which causes SN via elastic heating. We also indicate here estimates of the scattering constraints from cosmology, direct detection, MACRO, and ancient mica [115].

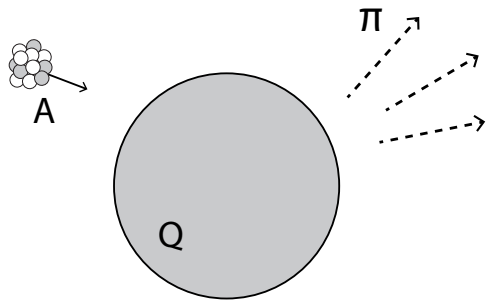

Figure 4.12: Interaction of a baryonic Q-ball with a nucleus A. The Q-ball destroys the nucleus and absorbs its baryonic charge, while the excess energy is radiated into roughly A outgoing pions of energy $\Lambda_{\rm QCD}$.

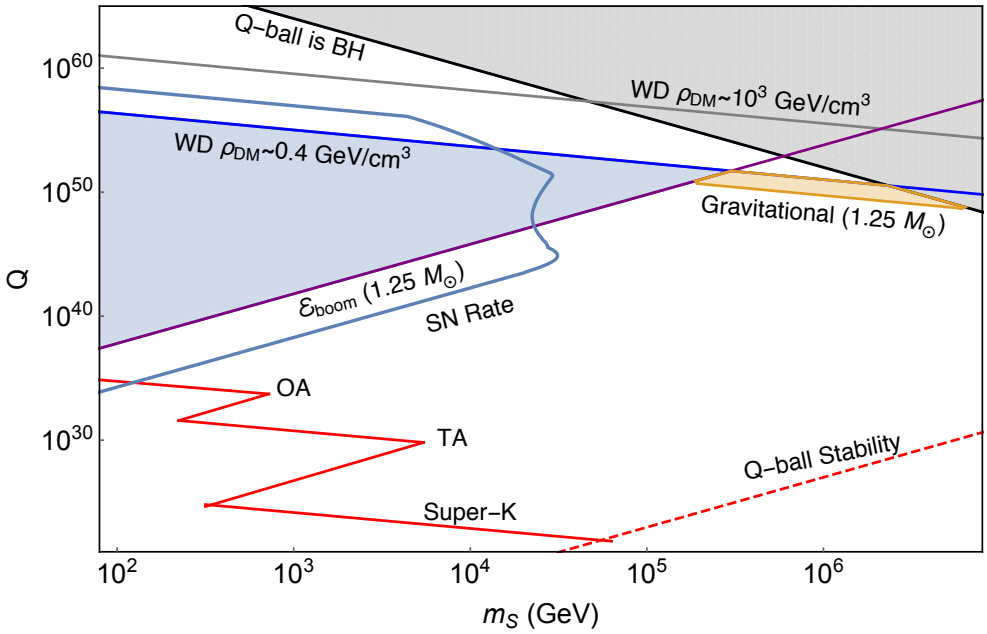

Figure 4.13: Constraints on Q-ball DM. Bounds come from demanding that the Q-ball interaction during a DM transit is capable of igniting WDs, occurring at a rate large enough to either ignite a single observed 1.25 $M_\odot$ WD in its lifetime (WD in local DM density is blue shaded) or exceed the measured SN rate in our galaxy. Also shown is the corresponding constraint from gravitational heating of WDs (orange shaded), and existing limits from terrestrial detectors (red) [119].

References

[1] Ryan Janish et al. "Axion production and detection with superconducting RF cavities" (2019). arXiv: 1904.07245 [hep-ph].

[2] David E. Kaplan, Surjeet Rajendran, and Paul Riggins. "Particle Probes with Superradiant Pulsars" (2019). in preparation.

[3] Peter W. Graham et al. "White Dwarfs as Dark Matter Detectors". *Phys. Rev.* D98.11 (2018), p. 115027. DOI: 10.1103/PhysRevD.98.115027. arXiv: 1805.07381 [hep-ph].

[4] R. D. Peccei and Helen R. Quinn. "CP Conservation in the Presence of Instantons". *Phys. Rev. Lett.* 38 (1977), pp. 1440–1443. DOI: 10.1103/PhysRevLett.38.1440.

[5] R. D. Peccei and Helen R. Quinn. "Constraints Imposed by CP Conservation in the Presence of Instantons". *Phys. Rev.* D16 (1977), pp. 1791–1797. DOI: 10.1103/PhysRevD.16.1791.

[6] Steven Weinberg. "A New Light Boson?" *Phys. Rev. Lett.* 40 (1978), pp. 223–226. DOI: 10.1103/PhysRevLett.40.223.

[7] Frank Wilczek. "Problem of Strong P and T Invariance in the Presence of Instantons". *Phys. Rev. Lett.* 40 (1978), pp. 279–282. DOI: 10.1103/PhysRevLett.40.279.

[8] John Preskill, Mark B. Wise, and Frank Wilczek. "Cosmology of the Invisible Axion". *Phys. Lett.* B120 (1983), pp. 127–132. DOI: 10.1016/0370-2693(83)90637-8.

[9] L. F. Abbott and P. Sikivie. "A Cosmological Bound on the Invisible Axion". *Phys. Lett.* B120 (1983), pp. 133–136. DOI: 10.1016/0370-2693(83)90638-X.

[10] Michael Dine and Willy Fischler. "The Not So Harmless Axion". *Phys. Lett.* B120 (1983), pp. 137–141. DOI: 10.1016/0370-2693(83)90639-1.

[11] Peter W. Graham, David E. Kaplan, and Surjeet Rajendran. "Cosmological Relaxation of the Electroweak Scale". *Phys. Rev. Lett.* 115.22 (2015), p. 221801. DOI: 10.1103/PhysRevLett.115.221801. arXiv: 1504.07551 [hep-ph].

[12] Peter W. Graham, David E. Kaplan, and Surjeet Rajendran. "Relaxation of the Cosmological Constant" (2019). arXiv: 1902.06793 [hep-ph].

[13] Peter Svrcek and Edward Witten. "Axions In String Theory". *JHEP* 06 (2006), p. 051. DOI: 10.1088/1126-6708/2006/06/051. arXiv: hep-th/0605206.

[14] Asimina Arvanitaki et al. "String Axiverse". *Phys. Rev.* D81 (2010), p. 123530. DOI: 10.1103/PhysRevD.81.123530. arXiv: 0905.4720 [hep-th].

[15] Pierre Sikivie. "Experimental Tests of the Invisible Axion". *Phys. Rev. Lett.* 51 (1983), pp. 1415–1417. DOI: 10.1103/PhysRevLett.51.1415.

[16] K. Van Bibber et al. "Proposed experiment to produce and detect light pseudoscalars". *Phys. Rev. Lett.* 59 (1987), pp. 759–762. DOI: 10.1103/PhysRevLett.59.759.

[17] P. Sikivie, D. B. Tanner, and Karl van Bibber. "Resonantly enhanced axion-photon regeneration". *Phys. Rev. Lett.* 98 (2007), p. 172002. DOI: 10.1103/PhysRevLett.98.172002. arXiv: hep-ph/0701198.

[18] Klaus Ehret et al. "Resonant laser power build-up in ALPS: A 'Light-shining-through-walls' experiment". *Nucl. Instrum. Meth.* A612 (2009), pp. 83–96. DOI: 10.1016/j.nima.2009.10.102. arXiv: 0905.4159 [physics.ins-det].

[19] Klaus Ehret et al. "New ALPS Results on Hidden-Sector Lightweights". *Phys. Lett.* B689 (2010), pp. 149–155. DOI: 10.1016/j.physletb.2010.04.066. arXiv: 1004.1313 [hep-ex].

[20] Robin Bahre et al. "Any light particle search II – Technical Design Report". *JINST* 8 (2013), T09001. DOI: 10.1088/1748-0221/8/09/T09001. arXiv: 1302.5647 [physics.ins-det].

[21] F. Hoogeveen. "Terrestrial axion production and detection using RF cavities". *Phys. Lett.* B288 (1992), pp. 195–200. DOI: 10.1016/0370-2693(92)91977-H.

[22] Joerg Jaeckel and Andreas Ringwald. "A Cavity Experiment to Search for Hidden Sector Photons". *Phys. Lett.* B659 (2008), pp. 509–514. DOI: 10.1016/j.physletb.2007.11.071. arXiv: 0707.2063 [hep-ph].

[23] Fritz Caspers, Joerg Jaeckel, and Andreas Ringwald. "Feasibility, engineering aspects and physics reach of microwave cavity experiments searching for hidden photons and axions". *JINST* 4 (2009), P11013. DOI: 10.1088/1748-0221/4/11/P11013. arXiv: 0908.0759 [hep-ex].

[24] M. Betz et al. "First results of the CERN Resonant Weakly Interacting sub-eV Particle Search (CROWS)". *Phys. Rev.* D88.7 (2013), p. 075014. DOI: 10.1103/PhysRevD.88.075014. arXiv: 1310.8098 [physics.ins-det].

[25] Peter W. Graham et al. "Experimental Searches for the Axion and Axion-Like Particles". *Ann. Rev. Nucl. Part. Sci.* 65 (2015), pp. 485–514. DOI: 10.1146/annurev-nucl-102014-022120. arXiv: 1602.00039 [hep-ex].

[26] A. Grassellino et al. "Nitrogen and argon doping of niobium for superconducting radio frequency cavities: a pathway to highly efficient accelerating structures". *Supercond. Sci. Technol.* 26 (2013), p. 102001. DOI: 10.1088/0953-2048/26/10/102001. arXiv: 1306.0288 [physics.acc-ph].

[27] Roni Harnik. *SRF-based dark matter search: Theory Motivation*. https://indico.fnal.gov/event/19433/session/2/contribution/1/material/slides/0.pdf.

[28] Anna Grasselino. *SRF-based dark matter search: Experiment*. https://indico.fnal.gov/event/19433/session/2/contribution/2/material/slides/0.pdf.

[29] Zachary Bogorad et al. "Probing ALPs and the Axiverse with Superconducting Radiofrequency Cavities" (2019). arXiv: 1902.01418 [hep-ph].

[30] Yonatan Kahn, Benjamin R. Safdi, and Jesse Thaler. "Broadband and Resonant Approaches to Axion Dark Matter Detection". *Phys. Rev. Lett.* 117.14 (2016), p. 141801. DOI: 10.1103/PhysRevLett.117.141801. arXiv: 1602.01086 [hep-ph].

[31] Saptarshi Chaudhuri et al. "Radio for hidden-photon dark matter detection". *Phys. Rev.* D92.7 (2015), p. 075012. DOI: 10.1103/PhysRevD.92.075012. arXiv: 1411.7382 [hep-ph].

[32] S. Posen, N. Valles, and M. Liepe. "RF Magnetic Field Limits of Nb and Nb_3Sn". *Phys. Rev. Lett.* 115.4 (2015), p. 047001. DOI: 10.1103/PhysRevLett.115.047001.

[33] M. Martinello et al. "Effect of Interstitial Impurities on the Field Dependent Microwave Surface Resistance of Niobium". *Appl. Phys. Lett.* 109 (2016), p. 062601. DOI: 10.1063/1.4960801. arXiv: 1606.04174 [physics.acc-ph].

[34] Z. Charifoulline. "Residual resistivity ratio (RRR) measurements of LHC superconducting NbTi cable strands". *IEEE Trans. Appl. Supercond.* 16.2 (2006), pp. 1188–1191. DOI: 10.1109/TASC.2006.873322.

[35] Ping Ao and David J. Thouless. "Berry's phase and the Magnus force for a vortex line in a superconductor". *Phys. Rev. Lett.* 70 (14 Apr. 1993), pp. 2158–2161. DOI: 10.1103/PhysRevLett.70.2158. URL: https://link.aps.org/doi/10.1103/PhysRevLett.70.2158.

[36] James F. Annett. *Superconductivity, Superfluids and Condensates*. Oxford University Press, 2003.

[37] Jonathan L. Ouellet. private communication.

[38] S. M. Anton et al. "Magnetic Flux Noise in dc SQUIDs: Temperature and Geometry Dependence". *Phys. Rev. Lett.* 110 (14 Apr. 2013), p. 147002. DOI: 10.1103/PhysRevLett.110.147002. URL: https://link.aps.org/doi/10.1103/PhysRevLett.110.147002.

[39] V. Anastassopoulos et al. "New CAST Limit on the Axion-Photon Interaction". *Nature Phys.* 13 (2017), pp. 584–590. DOI: 10.1038/nphys4109. arXiv: 1705.02290 [hep-ex].

[40] Peter W. Graham et al. "Parametrically enhanced hidden photon search". *Phys. Rev.* D90.7 (2014), p. 075017. DOI: 10.1103/PhysRevD.90.075017. arXiv: 1407.4806 [hep-ph].

[41] Wayne Hu, Rennan Barkana, and Andrei Gruzinov. "Cold and fuzzy dark matter". *Phys. Rev. Lett.* 85 (2000), pp. 1158–1161. DOI: 10.1103/PhysRevLett.85.1158. arXiv: astro-ph/0003365.

[42] E. G. Adelberger, Blayne R. Heckel, and A. E. Nelson. "Tests of the gravitational inverse square law". *Ann. Rev. Nucl. Part. Sci.* 53 (2003), pp. 77–121. DOI: 10.1146/annurev.nucl.53.041002.110503. arXiv: hep-ph/0307284.

[43] Asimina Arvanitaki and Sergei Dubovsky. "Exploring the String Axiverse with Precision Black Hole Physics". *Phys. Rev.* D83 (2011), p. 044026. DOI: 10.1103/PhysRevD.83.044026. arXiv: 1004.3558 [hep-th].

[44] Asimina Arvanitaki, Masha Baryakhtar, and Xinlu Huang. "Discovering the QCD Axion with Black Holes and Gravitational Waves". *Phys. Rev.* D91.8 (2015), p. 084011. DOI: 10.1103/PhysRevD.91.084011. arXiv: 1411.2263 [hep-ph].

[45] Masha Baryakhtar, Robert Lasenby, and Mae Teo. "Black hole superradiance signatures of ultralight vectors". *Phys. Rev. D* 96 (3 Aug. 2017), p. 035019. DOI: 10.1103/PhysRevD.96.035019. URL: https://link.aps.org/doi/10.1103/PhysRevD.96.035019.

[46] R. P. Fender, E. Gallo, and D. Russell. "No evidence for black hole spin powering of jets in X-ray binaries". *Mon. Not. Roy. Astron. Soc.* 406.3 (Aug. 2010), pp. 1425–1434. ISSN: 0035-8711. DOI: 10.1111/j.1365-2966.2010.16754.x.

[47] Samir D. Mathur. "The Information paradox: A Pedagogical introduction". *Class. Quant. Grav.* 26 (2009), p. 224001. DOI: 10.1088/0264-9381/26/22/224001. arXiv: 0909.1038 [hep-th].

[48] Ahmed Almheiri et al. "Black Holes: Complementarity or Firewalls?" *JHEP* 02 (2013), p. 062. DOI: 10.1007/JHEP02(2013)062. arXiv: 1207.3123 [hep-th].

[49] David E. Kaplan and Surjeet Rajendran. "Firewalls in General Relativity". *Phys. Rev.* D99.4 (2019), p. 044033. DOI: 10.1103/PhysRevD.99.044033. arXiv: 1812.00536 [hep-th].

[50] Ya. B. Zel'dovich. "Amplification of cylindrical electromagnetic waves reflected from a rotating body". *Sov. Phys. JETP* 35.6 (1972), pp. 1085–1087. URL: http://www.jetp.ac.ru/cgi-bin/dn/e_035_06_1085.pdf.

[51] Mauricio Richartz et al. "General universal superradiant scattering". *Phys. Rev.* D80 (2009), p. 124016. DOI: 10.1103/PhysRevD.80.124016. arXiv: 0909.2317 [gr-qc].

[52] Jacob D. Bekenstein and Marcelo Schiffer. "The Many faces of superradiance". *Phys. Rev.* D58 (1998), p. 064014. DOI: 10.1103/PhysRevD.58.064014. arXiv: gr-qc/9803033.

[53] Vitor Cardoso, Richard Brito, and Joao L. Rosa. "Superradiance in stars". *Phys. Rev.* D91.12 (2015), p. 124026. DOI: 10.1103/PhysRevD.91.124026. arXiv: 1505.05509 [gr-qc].

[54] Vitor Cardoso, Paolo Pani, and Tien-Tien Yu. "Superradiance in rotating stars and pulsar-timing constraints on dark photons". *Phys. Rev.* D95.12 (2017), p. 124056. DOI: 10.1103/PhysRevD.95.124056. arXiv: 1704.06151 [gr-qc].

[55] Francesca V. Day and Jamie I. McDonald. "Axion superradiance in rotating neutron stars" (2019). arXiv: 1904.08341 [hep-ph].

[56] J. M. Lattimer and M. Prakash. "Neutron star structure and the equation of state". *Astrophys. J.* 550 (2001), p. 426. DOI: 10.1086/319702. arXiv: astro-ph/0002232.

[57] C. Cutler, L. Lindblom, and R. J. Splinter. "Damping times for neutron star oscillations". *Astrophys. J.* 363 (Nov. 1990), pp. 603–611. DOI: 10.1086/169370.

[58] Jason W. T. Hessels et al. "A radio pulsar spinning at 716-hz". *Science* 311 (2006), pp. 1901–1904. DOI: 10.1126/science.1123430. arXiv: astro-ph/0601337.

[59] S. R. Kulkarni. "The First Decade of Millisecond Pulsars: an Overview". In: *Millisecond Pulsars. A Decade of Surprise*. Ed. by A. S. Fruchter, M. Tavani, and D. C. Backer. Vol. 72. Astronomical Society of the Pacific Conference Series. 1995, p. 79.

[60] William G. Laarakkers and Eric Poisson. "Quadrupole moments of rotating neutron stars". *Astrophys. J.* 512 (1999), pp. 282–287. DOI: 10.1086/306732. arXiv: gr-qc/9709033.

[61] D. I. Jones. "Gravitational waves from freely precessing neutron stars". *ICTP Lect. Notes Ser.* 3 (2001), pp. 357–370.

[62] Benjamin J. Owen. "Maximum elastic deformations of compact stars with exotic equations of state". *Phys. Rev. Lett.* 95 (2005), p. 211101. DOI: 10.1103/PhysRevLett.95.211101. arXiv: astro-ph/0503399.

[63] C. M. Espinoza et al. "A study of 315 glitches in the rotation of 102 pulsars". *Mon. Not. Roy. Astron. Soc.* 414 (June 2011), pp. 1679–1704. DOI: 10.1111/j.1365-2966.2011.18503.x. arXiv: 1102.1743 [astro-ph.HE].

[64] E. S. Phinney and S. R. Kulkarni. "Binary and Millisecond Pulsars". *Ann. Rev. Astron. Astrophys.* 32.1 (1994), pp. 591–639. DOI: 10.1146/annurev.aa.32.090194.003111.

[65] Dima G. Yakovlev and C. J. Pethick. "Neutron star cooling". *Ann. Rev. Astron. Astrophys.* 42 (2004), pp. 169–210. DOI: 10.1146/annurev.astro.42.053102.134013. arXiv: astro-ph/0402143.

[66] Mikhail E. Gusakov, Andrey I. Chugunov, and Elena M. Kantor. "Explaining observations of rapidly rotating neutron stars in low-mass x-ray binaries". *Phys. Rev.* D90.6 (2014), p. 063001. DOI: 10.1103/PhysRevD.90.063001. arXiv: 1305.3825 [astro-ph.SR].

[67] G. B. Cook, S. L. Shapiro, and S. A. Teukolsky. "Rapidly rotating neutron stars in general relativity: Realistic equations of state". *Astrophys. J.* 424 (Apr. 1994), pp. 823–845. DOI: 10.1086/173934.

[68] Alessandro Patruno, Brynmor Haskell, and Caroline D'Angelo. "Gravitational Waves and the Maximum Spin Frequency of Neutron Stars". *Astrophys. J.* 746.1, 9 (Feb. 2012), p. 9. DOI: 10.1088/0004-637X/746/1/9. arXiv: 1109.0536 [astro-ph.HE].

[69] Lars Bildsten. "Gravitational Radiation and Rotation of Accreting Neutron Stars". *Astrophys. J.* 501.1 (July 1998), pp. L89–L93. DOI: 10.1086/311440. URL: https://doi.org/10.1086%2F311440.

[70] Curt Cutler. "Gravitational waves from neutron stars with large toroidal B fields". *Phys. Rev. D* 66 (8 Oct. 2002), p. 084025. DOI: 10.1103/PhysRevD.66.084025. URL: https://link.aps.org/doi/10.1103/PhysRevD.66.084025.

[71] Nils Andersson, Kostas D. Kokkotas, and Bernard F. Schutz. "Gravitational radiation limit on the spin of young neutron stars". *Astrophys. J.* 510 (1999), p. 846. DOI: 10.1086/306625. arXiv: astro-ph/9805225.

[72] Nils Andersson. "A New class of unstable modes of rotating relativistic stars". *Astrophys. J.* 502 (1998), pp. 708–713. DOI: 10.1086/305919. arXiv: gr-qc/9706075.

[73] Lee Lindblom, Benjamin J. Owen, and Sharon M. Morsink. "Gravitational radiation instability in hot young neutron stars". *Phys. Rev. Lett.* 80 (1998), pp. 4843–4846. DOI: 10.1103/PhysRevLett.80.4843. arXiv: gr-qc/9803053.

[74] D. S. Akerib et al. "Results from a search for dark matter in the complete LUX exposure". *Phys. Rev. Lett.* 118.2 (2017), p. 021303. DOI: 10.1103/PhysRevLett.118.021303. arXiv: 1608.07648 [astro-ph.CO].

[75] R. Agnese et al. "Results from the Super Cryogenic Dark Matter Search Experiment at Soudan". *Phys. Rev. Lett.* 120.6 (2018), p. 061802. DOI: 10.1103/PhysRevLett.120.061802. arXiv: 1708.08869 [hep-ex].

[76] Kim Griest, Agnieszka M. Cieplak, and Matthew J. Lehner. "Experimental Limits on Primordial Black Hole Dark Matter from the First 2 yr of Kepler Data". *Astrophys. J.* 786.2 (2014), p. 158. DOI: 10.1088/0004-637X/786/2/158. arXiv: 1307.5798 [astro-ph.CO].

[77] Peter W. Graham, Surjeet Rajendran, and Jaime Varela. "Dark Matter Triggers of Supernovae". *Phys. Rev.* D92.6 (2015), p. 063007. DOI: 10.1103/PhysRevD.92.063007. arXiv: 1505.04444 [hep-ph].

[78] Dan Maoz and Filippo Mannucci. "Type-Ia supernova rates and the progenitor problem, a review". *Publ. Astron. Soc. Austral.* 29 (2012), p. 447. DOI: 10.1071/AS11052. arXiv: 1111.4492 [astro-ph.CO].

[79] R. Scalzo et al. "Type Ia supernova bolometric light curves and ejected mass estimates from the Nearby Supernova Factory". *Mon. Not. Roy. Astron. Soc.* 440.2 (2014), pp. 1498–1518. DOI: 10.1093/mnras/stu350. arXiv: 1402.6842 [astro-ph.CO].

[80] R. A. Scalzo, A. J. Ruiter, and S. A. Sim. "The ejected mass distribution of type Ia supernovae: A significant rate of non-Chandrasekhar-mass progenitors". *Mon. Not. Roy. Astron. Soc.* 445.3 (2014), pp. 2535–2544. DOI: 10.1093/mnras/stu1808. arXiv: 1408.6601 [astro-ph.HE].

[81] Sean L. McGee and Michael L. Balogh. "Constraints on intragroup stellar mass from hostless Type Ia supernova". *Mon. Not. Roy. Astron. Soc.* 403 (2010), p. 79. DOI: 10.1111/j.1745-3933.2010.00819.x. arXiv: 0912.3455 [astro-ph.CO].

[82] Ryan J. Foley et al. "Type Iax Supernovae: A New Class of Stellar Explosion". *Astrophys. J.* 767 (2013), p. 57. DOI: 10.1088/0004-637X/767/1/57. arXiv: 1212.2209 [astro-ph.SR].

[83] Mansi M. Kasliwal et al. "Calcium-rich gap transients in the remote outskirts of galaxies". *Astrophys. J.* 755 (2012), p. 161. DOI: 10.1088/0004-637X/755/2/161. arXiv: 1111.6109 [astro-ph.HE].

[84] S. E. Woosley and T. A. Weaver. "Sub-Chandrasekhar mass models for Type IA supernovae". *Astrophys. J.* 423 (Mar. 1994), pp. 371–379. DOI: 10.1086/173813.

[85] M. Fink, W. Hillebrandt, and F. K. Roepke. "Double-detonation supernovae of sub-Chandrasekhar mass white dwarfs". *Astron. Astrophys.* (2007). DOI: 10.1051/0004-6361:20078438. arXiv: 0710.5486 [astro-ph].

[86] R. Pakmor, M. Kromer, and S. Taubenberger. "Helium-ignited violent mergers as a unified model for normal and rapidly declining Type Ia Supernovae". *Astrophys. J.* 770 (2013), p. L8. DOI: 10.1088/2041-8205/770/1/L8. arXiv: 1302.2913 [astro-ph.HE].

[87] P. H. Sell et al. "Calcium-Rich Gap Transients: Tidal Detonations of White Dwarfs?" *Mon. Not. Roy. Astron. Soc.* 450.4 (2015), pp. 4198–4206. DOI: 10.1093/mnras/stv902. arXiv: 1504.05584 [astro-ph.HE].

[88] F. X. Timmes and S. E. Woosley. "The conductive propagation of nuclear flames. I - Degenerate C + O and O + NE + MG white dwarfs". *Astrophys. J.* 396 (Sept. 1992), pp. 649–667. DOI: 10.1086/171746.

[89] Gianfranco Bertone and Malcolm Fairbairn. "Compact Stars as Dark Matter Probes". *Phys. Rev.* D77 (2008), p. 043515. DOI: 10.1103/PhysRevD.77.043515. arXiv: 0709.1485 [astro-ph].

[90] Matthew McCullough and Malcolm Fairbairn. "Capture of Inelastic Dark Matter in White Dwarves". *Phys. Rev.* D81 (2010), p. 083520. DOI: 10.1103/PhysRevD.81.083520. arXiv: 1001.2737 [hep-ph].

[91] S. -C. Leung et al. "Dark-matter admixed white dwarfs". *Phys. Rev.* D87.12 (2013), p. 123506. DOI: 10.1103/PhysRevD.87.123506. arXiv: 1305.6142 [astro-ph.CO].

[92] Joseph Bramante. "Dark matter ignition of type Ia supernovae". *Phys. Rev. Lett.* 115.14 (2015), p. 141301. DOI: 10.1103/PhysRevLett.115.141301. arXiv: 1505.07464 [hep-ph].

[93] L. R. Gasques et al. "Nuclear fusion in dense matter: Reaction rate and carbon burning". *Phys. Rev.* C72 (2005), p. 025806. DOI: 10.1103/PhysRevC.72.025806. arXiv: astro-ph/0506386.

[94] F. X. Timmes. *Cold White Dwarfs*. URL: http://cococubed.asu.edu/code_pages/coldwd.shtml.

[95] Raj Gandhi et al. "Neutrino interactions at ultrahigh-energies". *Phys. Rev.* D58 (1998), p. 093009. DOI: 10.1103/PhysRevD.58.093009. arXiv: hep-ph/9807264.

[96] J. A. Formaggio and G. P. Zeller. "From eV to EeV: Neutrino Cross Sections Across Energy Scales". *Rev. Mod. Phys.* 84 (2012), pp. 1307–1341. DOI: 10.1103/RevModPhys.84.1307. arXiv: 1305.7513 [hep-ex].

[97] William H. Press and David N. Spergel. "Capture by the sun of a galactic population of weakly interacting massive particles". *Astrophys. J.* 296 (1985), pp. 679–684. DOI: 10.1086/163485.

[98] Andrew Gould. "Resonant Enhancements in WIMP Capture by the Earth". *Astrophys. J.* 321 (1987), p. 571. DOI: 10.1086/165653.

[99] Ryan Janish, Vijay Narayan, and Paul Riggins. "Supernovae from dark matter gravitational collapse" (2019). in preparation.

[100] D. E. Winget et al. "An independent method for determining the age of the universe". *Astrophys. J.l* 315 (Apr. 1987), pp. L77–L81. DOI: 10.1086/184864.

[101] Sandro Mereghetti. "RX J0648.0–4418: the fastest-spinning white dwarf". In: *Proceedings, 13th Marcel Grossmann Meeting on Recent Developments in Theoretical and Experimental General Relativity, Astrophysics, and Relativistic Field Theories (MG13): Stockholm, Sweden, July 1-7, 2012*. 2015, pp. 2459–2461. DOI: 10.1142/9789814623995_0469. arXiv: 1302.4634 [astro-ph.HE].

[102] S. J. Kleinman et al. "SDSS DR7 White Dwarf Catalog". *Astrophys. J. Suppl.* 204, 5 (Jan. 2013), p. 5. DOI: 10.1088/0067-0049/204/1/5. arXiv: 1212.1222 [astro-ph.SR].

[103] Kerstin Perez et al. "Extended hard-X-ray emission in the inner few parsecs of the Galaxy". *Nature* 520 (Apr. 2015), p. 646. URL: https://doi.org/10.1038/nature14353%20http://10.0.4.14/nature14353.

[104] Fabrizio Nesti and Paolo Salucci. "The Dark Matter halo of the Milky Way, AD 2013". *JCAP* 1307 (2013), p. 016. DOI: 10.1088/1475-7516/2013/07/016. arXiv: 1304.5127 [astro-ph.GA].

[105] S. Chandrasekhar. *An Introduction to the Study of Stellar Structure*. University of Chicago Press, 1939.

[106] R. Kippenhahn and A. Weigert. *Stellar Structure and Evolution*. Springer, 1994.

[107] Cora Dvorkin, Kfir Blum, and Marc Kamionkowski. "Constraining Dark Matter-Baryon Scattering with Linear Cosmology". *Phys. Rev.* D89.2 (2014), p. 023519. DOI: 10.1103/PhysRevD.89.023519. arXiv: 1311.2937 [astro-ph.CO].

[108] Tracy R. Slatyer, Nikhil Padmanabhan, and Douglas P. Finkbeiner. "CMB Constraints on WIMP Annihilation: Energy Absorption During the Recombination Epoch". *Phys. Rev.* D80 (2009), p. 043526. DOI: 10.1103/PhysRevD.80.043526. arXiv: 0906.1197 [astro-ph.CO].

[109] Tracy R. Slatyer and Chih-Liang Wu. "General Constraints on Dark Matter Decay from the Cosmic Microwave Background". *Phys. Rev.* D95.2 (2017), p. 023010. DOI: 10.1103/PhysRevD.95.023010. arXiv: 1610.06933 [astro-ph.CO].

[110] Nikhil Padmanabhan and Douglas P. Finkbeiner. "Detecting dark matter annihilation with CMB polarization: Signatures and experimental prospects". *Phys. Rev.* D72 (2005), p. 023508. DOI: 10.1103/PhysRevD.72.023508. arXiv: astro-ph/0503486.

[111] Alexander Aab et al. "The Pierre Auger Cosmic Ray Observatory". *Nucl. Instrum. Meth.* A798 (2015), pp. 172–213. DOI: 10.1016/j.nima.2015.06.058. arXiv: 1502.01323 [astro-ph.IM].

[112] Gregory D. Mack, John F. Beacom, and Gianfranco Bertone. "Towards Closing the Window on Strongly Interacting Dark Matter: Far-Reaching Constraints from Earth's Heat Flow". *Phys. Rev.* D76 (2007), p. 043523. DOI: 10.1103/PhysRevD.76.043523. arXiv: 0705.4298 [astro-ph].

[113] E. Aprile et al. "First Dark Matter Search Results from the XENON1T Experiment". *Phys. Rev. Lett.* 119.18 (2017), p. 181301. DOI: 10.1103/PhysRevLett.119.181301. arXiv: 1705.06655 [astro-ph.CO].

[114] M. Ambrosio et al. "Final results of magnetic monopole searches with the MACRO experiment". *Eur. Phys. J.* C25 (2002), pp. 511–522. DOI: 10.1140/epjc/s2002-01046-9. arXiv: hep-ex/0207020.

[115] David M. Jacobs, Glenn D. Starkman, and Bryan W. Lynn. "Macro Dark Matter". *Mon. Not. Roy. Astron. Soc.* 450.4 (2015), pp. 3418–3430. DOI: 10.1093/mnras/stv774. arXiv: 1410.2236 [astro-ph.CO].

[116] Sidney R. Coleman. "Q Balls". *Nucl. Phys.* B262 (1985). [Erratum: Nucl. Phys.B269, 744(1986)], p. 263. DOI: 10.1016/0550-3213(85)90286-X,10.1016/0550-3213(86)90520-1.

[117] Alexander Kusenko and Mikhail E. Shaposhnikov. "Supersymmetric Q balls as dark matter". *Phys. Lett.* B418 (1998), pp. 46–54. DOI: 10.1016/S0370-2693(97)01375-0. arXiv: hep-ph/9709492.

[118] Alexander Kusenko et al. "Experimental signatures of supersymmetric dark matter Q balls". *Phys. Rev. Lett.* 80 (1998), pp. 3185–3188. DOI: 10.1103/PhysRevLett.80.3185. arXiv: hep-ph/9712212.

[119] Michael Dine and Alexander Kusenko. "The Origin of the matter - antimatter asymmetry". *Rev. Mod. Phys.* 76 (2003), p. 1. DOI: 10.1103/RevModPhys.76.1. arXiv: hep-ph/0303065.

[120] David A. Hill. *Electromagnetic Fields in Cavities*. Wiley, 2009.

[121] K. Grohmann et al. "Current comparators with superconducting shields". *Cryogenics* 14 (1974), pp. 499–502.

[122] S. Tavernier. *Experimental Techniques in Nuclear and Particle Physics*. Springer, 2010.

[123] T.-S. H. Lee and R. P. Redwine. "Pion-Nucleus Interactions". *Annu. Rev. Nucl. Part. Sci.* 52.1 (2002), pp. 23–63. DOI: 10.1146/annurev.nucl.52.050102.090713. URL: https://doi.org/10.1146/annurev.nucl.52.050102.090713.

[124] Lisa Gerhardt and Spencer R. Klein. "Electron and Photon Interactions in the Regime of Strong LPM Suppression". *Phys. Rev.* D82 (2010), p. 074017. DOI: 10.1103/PhysRevD.82.074017. arXiv: 1007.0039 [hep-ph].

[125] Spencer Klein. "Suppression of Bremsstrahlung and pair production due to environmental factors". *Rev. Mod. Phys.* 71 (1999), pp. 1501–1538. DOI: 10.1103/RevModPhys.71.1501. arXiv: hep-ph/9802442.

[126] H. Bethe and W. Heitler. "On the Stopping of fast particles and on the creation of positive electrons". *Proc. Roy. Soc. Lond.* A146 (1934), pp. 83–112. DOI: 10.1098/rspa.1934.0140.

[127] Stuart L. Shapiro and Saul A. Teukolsky. *Black Holes, White Dwarfs, and Neutron Stars*. Wiley, 1983.

[128] John David Jackson. *Classical electrodynamics*. 3rd ed. New York, NY: Wiley, 1999. ISBN: 9780471309321. URL: http://cdsweb.cern.ch/record/490457.

[129] Bruno Rossi. *High Energy Particles*. Prentice-Hall, Inc., Englewood Cliffs, NJ, 1952.

[130] Richard H. Helm. "Inelastic and Elastic Scattering of 187-Mev Electrons from Selected Even-Even Nuclei". *Phys. Rev.* 104 (1956), pp. 1466–1475. DOI: 10.1103/PhysRev.104.1466.

[131] Joseph Bramante, Antonio Delgado, and Adam Martin. "Multiscatter stellar capture of dark matter". *Phys. Rev.* D96.6 (2017), p. 063002. DOI: 10.1103/PhysRevD.96.063002. arXiv: 1703.04043 [hep-ph].

[132] Chris Kouvaris and Peter Tinyakov. "Constraining Asymmetric Dark Matter through observations of compact stars". *Phys. Rev.* D83 (2011), p. 083512. DOI: 10.1103/PhysRevD.83.083512. arXiv: 1012.2039 [astro-ph.HE].

Appendices

Appendix A

Appendices relating to Chapter 2

A.1 Estimate of the axion-induced fields

In this appendix we estimate the magnitude of the axion-induced fields, assuming a simple geometry for the production cavity and toroidal conversion region. From the expressions for the axion source field (2.6) and effective current (2.9), the axion-induced magnetic field at a detection point $\vec{r}$ is generally of the form:

$$\vec{B}_a(\vec{r}) = \frac{i\omega g^2}{(4\pi)^2}\, e^{i\omega t} \int_{\rm pc} d^3y \int_{\rm cr} d^3x \qquad \text{(A.1)}$$
$$\left\{ \vec{\lambda} \times \vec{B}_0\left(\vec{x}\right) \left[\frac{1}{\lambda^3} + \frac{i\omega}{\lambda^2}\right] \frac{e^{-i\omega\lambda}\, e^{ik_a|\vec{x}-\vec{y}|}}{|\vec{x}-\vec{y}|} \left(\vec{E}\cdot\vec{B}\right)_\omega \right\}.$$

Here the integration $\vec{y}$ is taken over the volume of the production cavity, $\vec{x}$ is over the volume of the conversion region, and $\vec{\lambda} = (\vec{r} - \vec{x})$ is the separation vector between points in the toroid and a detection point $\vec{r}$. The time-dependent $J_{\rm eff}$ has been evaluated at the retarded time $t_r = t - \lambda$. (A.1) also uses the approximation that the axion-induced fields fully propagate outside of the toroid, as expected for quasistatic frequencies. B_a lies in the poloidal direction and has an amplitude:

$$\hat{z}\cdot\vec{B}_a = \frac{g^2 B_{\rm pc}^2 B_0}{\omega^2}\beta(\vec{r}), \qquad \text{(A.2)}$$

where the dimensionless form factor β contains information about the choice of cavity modes, etc.

First we specify the dimensions involved. Consider a circular cylindrical cavity ("pill-box") of radius a and height h. The resonant frequencies are

$$\omega_{npq}^{\rm TM} = \sqrt{\left(\frac{x_{np}}{a}\right)^2 + \left(\frac{q\pi}{h}\right)^2} \qquad \text{(A.3)}$$
$$\omega_{npq}^{\rm TE} = \sqrt{\left(\frac{x'_{np}}{a}\right)^2 + \left(\frac{q\pi}{h}\right)^2},$$

for TM_{npq} and TE_{npq} modes respectively, where x_{np} and x'_{np} are the pth roots of the nth order Bessel function $J_n(x)$ and its derivative $J'_n(x)$ [120]. Setting $a = h/2 = 10$ cm ensures resonant frequencies of order $\approx$ GHz for low-lying modes, typical of SRF cavities.

Next consider a toroid of inner radius R and rectangular cross section of height and width R. We take the cylindrical cavity to be aligned axially with the toroid, with a minimal separation distance of $(h+R)/2$. Though this should be gapped toroid, we can approximate the static field contained inside the toroidal volume as

$$\vec{B}_0(r) = B_0 \left(\frac{R}{r}\right) \hat{\phi}, \tag{A.4}$$

for $r \in [R, 2R]$ where r is the cylindrical radial distance from the center. If we require the toroid size saturates the quasistatic limit $R\omega \sim 1$, an economical choice for the dimension is simply $R = a$.

We now consider the axion source in this setup. The source axion field is greatest when $\vec{E} \cdot \vec{B}$ is maximal and coherent throughout the production cavity volume. Since we have assumed a cylindrical cavity with no external field, it is necessary to drive multiple modes to ensure a non-vanishing $(\vec{E} \cdot \vec{B})_\omega$. The choice of these modes is not obvious and requires care even in this simple setup.

To demonstrate an ill-advised choice consider the TM_{010} and TM_{111} modes which results in $(\vec{E}\cdot\vec{B})_\omega \propto \sin(\pi z/h)\sin(\phi)$. Note that the integral of $(\vec{E}\cdot\vec{B})_\omega$ vanishes over $z \in [-h/2, h/2]$ of the production cavity. This z-dependence is in fact a general feature of any cylindrical cavity modes chosen, but it is not detrimental as we are operating in the near-field regime. Rather, TM_{010} and TM_{111} represents a poor choice of modes because of the ϕ dependence—the sourced axion field will be purely harmonic in the azimuthal angle, and thus would integrate over the toroid to give a highly suppressed signal field near the center. This cancellation is essentially a consequence of the symmetry and alignment of the cylindrical setup and is easily avoidable. One potential solution is to place the production cavity in a position off the axial axis. Another is to modify the toroid wiring so $\vec{B}_0$ also varies with the azimuthal angle while still being effectively confined. One can also select cavity modes such that $(\vec{E} \cdot \vec{B})_\omega$ is not purely harmonic in ϕ: the lowest-lying combination of cylindrical modes which yields this angular behavior is the TM_{111} and TE_{111} modes.

In any case, we can estimate a reasonable upper limit to β in (A.2) by postulating a perfectly *uniform* $\vec{E} \cdot \vec{B}$ throughout the production cavity volume. Taking this optimal axion source, we numerically find that β is roughly constant for points in the center of the toroid:

$$\beta_{\text{optimal}} \approx 7 \cdot 10^{-2}, \quad z = 0 \text{ and } r \leq R. \tag{A.5}$$

Here we have also taken the limit in which the mass is negligible, $m_a \ll \omega$. At masses $m_a \gtrsim \omega$, there is the usual exponential drop-off from producing off-shell axions. If we instead use a perhaps more realistic axion source by driving the TM_{111} and TE_{111} combination, we numerically find that $\beta_{\text{realistic}} \approx 4 \cdot 10^{-4}$, again roughly constant near the center of the toroid.

In summary, we expect the form factor β can in principle be made $\mathcal{O}(0.1)$ in any suitably engineered designs. As discussed, it is important to determine a suitable geometry and

choice of modes to be driven in the SRF production cavity, as a poor choice could lead to a significant suppression of the signal fields.

A.2 A toy model for screening

We ultimately rely on the quasistatic approximation in assuming the axion-induced fields propagate $\mathcal{O}(1)$ out of the gapped toroid, similar to [30]. This limits the size of the toroid to be less than or of order the inverse frequency of the axion. However it is important to understand the *degree* to which the fields outside the toroid are suppressed at larger frequencies or larger toroid size. This is a complicated boundary-value problem and a full study would require a detailed numerical computation which is outside the scope of this work. We will demonstrate here the power-law nature of this suppression.

To gain some intuition, consider an electromagnetic field of frequency ω impinging on a perfect conducting sheet. If the conductor is infinitely large, then the incoming field is reflected and vanishes on the far side of the conductor (i.e., metals are shiny). An analogous behavior holds for fields sourced inside of a region bounded by a closed conducting surface—the field is exactly screened outside (i.e., phones do not work in elevators). The common feature is that the conductors lack a boundary. We thus expect incident fields to be suppressed, but not exactly screened, outside of a large yet finite conductor with a definite boundary. This will occur when the conductor size H is much larger than the wavelength ω^{-1}.

Now suppose the conductor is small relative to ω^{-1}. This is just the quasistatic limit, so we may asses the conductor's response by considering its response to a static field. In this familiar situation, the field will induce charges and currents on the surface of the conductor in order to screen the bulk. It is clear that the boundaries play an important role in this limit. For example, a conducting block in a static electric field will develop a screening charge density on the boundary, which modifies the net external field but does not result in a parametrically small external field. For $\omega H \ll 1$ we therefore expect the field on the far side of the conductor to only differ from the incident field by $\mathcal{O}(1)$ factors.

We study here a toy model of electromagnetic fields incident on a finite cylindrical conductor. The parametric effects of screening can be sensibly extracted in the high-frequency limit, and we find the magnitude of external, detected fields are only power-law suppressed compared to the internal fields. The physical mechanism underlying this suppression, as summarized in Sec. 2.3.3, is expected to hold generically in varied geometries.

Consider a perfectly conducting cylinder of height H and radius R. More precisely, take this to be a tube of negligible thickness separating an inner and outer cylindrical wall. Suppose there is an EM field $(\vec{E}_a, \vec{B}_a) = (E_a\hat{z}, B_a\hat{\phi})$, sourced by an infinite line of current $I_a e^{i\omega t}\hat{z}$ "in the throat" of the cylinder. This is labelled suggestively in analogy to fields sourced by the axion interaction with a static magnetic field, although for simplicity we assume a spatially uniform I_a. We specifically examine the limit of a thin cylinder and take $R \sim \omega^{-1} \ll H$, which is of course well beyond the quasistatic approximation. Here the fields

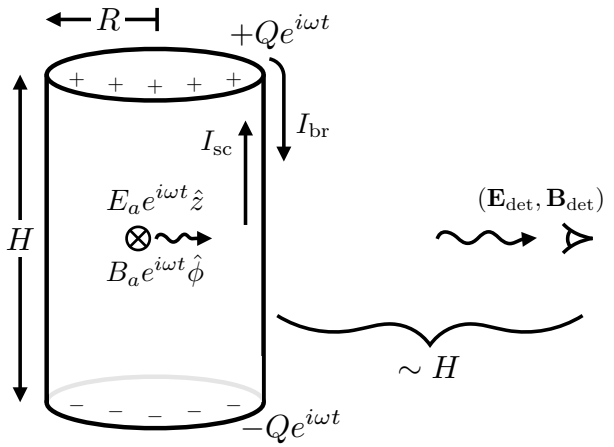

Figure A.1: Screening of EM fields $(\vec{E}_a, \vec{B}_a)$ sourced inside a finite cylindrical wall. In the high-frequency limit, the conductor response results in charge buildup Q on the edges and a configuration of screening currents $I_{\rm sc}$, $I_{\rm br}$ on the inner and outer surfaces. These in turn determine the fields $(\vec{E}_{\rm det}, \vec{B}_{\rm det})$ detected outside the cylinder.

radiated by I_a are cylindrical plane waves, with approximate magnitudes:

$$E_a(r) \sim B_a(r) \sim \omega I_a e^{i\omega t} \left(\frac{1}{\omega r}\right)^{1/2}, \quad R \lesssim r \lesssim H. \tag{A.6}$$

These source fields will be compared to the detected fields $(\vec{E}_{\rm det}, \vec{B}_{\rm det})$ at a point $r \sim H$ outside the cylinder. This is depicted in Fig. A.1. From here on, we restrict our attention to the behavior of fields in the region $R \lesssim r \lesssim H$, extending from the cylindrical surface to the detection point. We will also ignore any contributions to the fields due to the source wire I_a "sticking out" the ends, since this finite cylinder is intended to resemble an "unwrapped" version of our gapped toroid.

To determine the detected fields, the conductor response is paramount. Boundary conditions dictate that the electric and magnetic fields vanish in the thickness of the cylinder, and the z-component of the electric field vanishes on the surface. Importantly, for a finite cylinder the inner and outer surfaces are connected, so that the current established on the inner wall is communicated in some form to the outer wall. This communication, and the detected fields that result, can be estimated by approximately satisfying boundary conditions as follows:

Firstly, I_a drives a screening current $I_{\rm sc}$ on the inner walls in order to cancel the source fields. By continuity, there is then necessarily a charge buildup $\pm Qe^{i\omega t}$ at the top and bottom edges of the cylinder, respectively. We will not attempt to explicitly satisfy boundary conditions near these edges (which involves complicated fringe effects). Instead, we will consider the effects of this charge on the rest of the cylinder at locations far from the edges—that is, $H/2 - |z| \gg R$, where $z = 0$ corresponds to the vertical center of the cylinder. Here

the oscillating rings of charge at $z = \pm H/2$ appear as points and produce an electric field on the cylinder surface:

$$\hat{z} \cdot \vec{E}_Q(R, z) \sim Q e^{i\omega t} \left(\frac{e^{-i\omega z_+}(1 + i\omega z_+)}{z_+^2} + \frac{e^{-i\omega z_-}(1 + i\omega z_-)}{z_-^2} \right), \tag{A.7}$$

where $z_\pm = H/2 \pm z$. Up to a phase, this is approximately

$$\hat{z} \cdot \vec{E}_Q(R, z) \sim \frac{\omega Q e^{i\omega t}}{H/2 - |z|} \cos(\omega z). \tag{A.8}$$

To continue satisfying boundary conditions, this field must now be canceled. Therefore, a "back-reaction" current $I_{\rm br}$ must be set up on the cylinder walls, chosen to cancel $\vec{E}_Q$. Numerically, we find that a current of the form $I_{\rm br}(z) \sim I_{\rm br} \cos(\omega z)$ sources electric fields with the necessary sinusoidal behavior:

$$\hat{z} \cdot \vec{E}_{\rm br}(R, z) \sim \frac{I_{\rm br} e^{i\omega t}}{H/2 - |z|} \cos(\omega z). \tag{A.9}$$

We can ensure that this back-reaction does not also violate the previously satisfied boundary conditions by taking $I_{\rm br}$ to flow in the same same direction on both inner and outer walls. It is notable that near the center of the cylinder, (A.9) vanishes as the height increases $H \to \infty$. Such a scaling can be understood by considering a $\cos(\omega z)$ current on the surface of an *infinitely* tall cylinder. In that case, the z-component of the electric field exactly vanishes as there is a cancellation between the field sourced by the current and the field sourced by stripes of charge which are present due to charge continuity. This cancellation is weaker near the edges of a finite cylinder, leading to larger $\hat{z} \cdot \vec{E}_{\rm br}$ there.

The above charges/currents must be self-consistent. The initial screening current $I_{\rm sc}$ on the inner wall, charge buildup Q on the edges, and back-reaction currents $I_{\rm br}$ on both walls here are related by charge continuity:

$$\frac{dQ}{dt} = i\omega Q \sim I_{\rm sc} - 2I_{\rm br}, \tag{A.10}$$

where the factor of 2 accounts for the fact that $I_{\rm br}$ flows in the same direction on both walls. Since the cylinder is tall and thin, we can invoke the infinite-cylinder solution to approximately cancel the source fields, and thus we take $I_{\rm sc} \sim I_a$ on the inner surface. Comparing (A.8) and (A.9), to cancel the fields produced by the charge buildup requires back-reaction currents of order $I_{\rm br} \sim \omega Q$. These currents, taken together, then approximately satisfy boundary conditions everywhere away from the edges. Now further demanding the constraint of continuity (A.10), we find the charge buildup should be $Q \sim I_a/\omega$, and therefore the back-reaction currents are of order $I_{\rm br} \sim I_a \cos(\omega z)$. The z-component of the back-reaction field is parametrically smaller than the source field (A.6) on the surface:

$$\frac{\hat{z} \cdot \vec{E}_{\rm br}(R, z)}{E_a(R, z)} \sim (\omega H)^{-1} \ll 1. \tag{A.11}$$

This is consistent with our use of the infinite-cylinder solution for the inner screening current $I_{\rm sc} \sim I_a$.

To summarize, we have found there are additional currents $I_{\rm br} \sim I_a \cos(\omega z)$ on the inner and outer cylinder surfaces, arising from the need to satisfy boundary conditions in the presence of charge build-up. These are inevitably of the same order as the source current, but with a crucial spatial modulation. Based on these currents, we estimate the detected fields at a point $r \lesssim H$ (and near $z \sim 0$) outside the cylinder:

$$\begin{aligned}\vec{E}_{\rm det}(r,z) &\sim I_a \cos(\omega z) e^{i\omega t}\left(\frac{1}{r}\hat{r} + \frac{1}{H+r}\hat{z}\right), \\ \vec{B}_{\rm det}(r,z) &\sim \frac{I_a}{r}\cos(\omega z) e^{i\omega t}\hat{\phi}.\end{aligned} \tag{A.12}$$

The fields radiated by the oscillating charges on the cylinder edges are of this same magnitude.

The charge buildup and back-reaction currents thus propagate fields outside the cylinder. Importantly, the magnitudes of these fields (A.12) fall off as r^{-1}, faster than the $r^{-1/2}$ behavior of the source fields (A.6) that would be seen if the conductor were not present. Comparing these, we see the magnitude of the external, detected field is power-law suppressed:

$$B_{\rm det}/B_a \sim (\omega H)^{-1/2} \ll 1. \tag{A.13}$$

This is fundamentally because the fields radiated by a modulated, multipolar current decay more rapidly than the fields from a spatially uniform current.

Lastly, we briefly comment on the low-frequency behavior of our toy model. The spatially modulated current distribution we had found on the surface is a consequence of modulated fields from non-negligible charge buildup—this feature, however, is only present at sufficiently high frequencies. In the opposite limit $R, H \ll \omega^{-1}$, the analogous secondary fields from charge buildup are uniform across the cylinder surface and drive an unmodulated current that results in equal and opposite currents flowing on the inner and outer surfaces. This is the familiar quasistatic result in which no screening occurs and a uniform current loop is established, as in the operation of a cryogenic current comparator [121].

Appendix B

Appendices relating to Chapter 4

B.1 Particle Stopping in a White Dwarf

Here we provide a more detailed analysis of the stopping power (energy loss per distance traveled) of high-energy SM particles in a carbon-oxygen WD due to strong and electromagnetic interactions. We consider incident electrons, photons, pions, and nucleons with kinetic energy greater than an MeV.

B.1.1 WD Medium

For the WD masses that we consider, the stellar medium consists of electrons and fully-ionized carbon nuclei with central number densities in the range $n_e = Z n_{\rm ion} \sim 10^{31} - 10^{33}$ cm^{-3} where $Z = 6$. The internal temperature is $T \sim$ keV [106]. The electrons are a degenerate and predominantly relativistic free gas, with Fermi energy

$$E_F = (3\pi^2 n_e)^{1/3} \sim 1 - 10 \text{ MeV}. \tag{B.1}$$

The carbon ions, however, are non-degenerate and do not form a free gas. The plasma frequency due to ion-ion Coulomb interactions is given by

$$\Omega_p = \left(\frac{4\pi n_{\rm ion} Z^2 \alpha}{m_{\rm ion}} \right)^{1/2} \sim 1 - 10 \text{ keV}, \tag{B.2}$$

where $m_{\rm ion}$ is the ion mass. Finally, the medium also contains thermal photons, though these are never significant for stopping particles as the photon number density $n_\gamma \sim T^3$ is much smaller than that of electrons or ions.

B.1.2 Nuclear Interactions

Elastic Scattering of Hadrons. Hadrons with energy less than the nuclear binding energy $E_{\rm nuc} \sim 10$ MeV will predominantly stop due to elastic nuclear scatters with ions. These

are hard scatters, resulting in a stopping power

$$\frac{dE}{dx} \sim n_{\rm ion}\sigma_{\rm el}\left(\frac{m}{m_{\rm ion}}\right)E \tag{B.3}$$

for a hadron of mass $m \ll m_{\rm ion}$ and kinetic energy E. $\sigma_{\rm el}$ is the elastic nuclear scattering cross section, which is of order $\sigma_{\rm el} \approx$ b at these energies and drops to $\sigma_{\rm el} \approx 0.1$ b above 10 MeV [122], ignoring the nontrivial effect of nuclear resonances in the intermediate regime $1 - 10$ MeV.

Inelastic Scattering of Hadrons. For energies above $E_{\rm nuc}$, the stopping of hadrons is dominated by inelastic nuclear scatters. In such a collision, an incoming hadron interacts with one or more nucleons to produce a $\mathcal{O}(1)$ number of additional hadrons which approximately split the initial energy. At incident energy greater than $\sim$ GeV, the majority of secondary hadrons are pions with transverse momenta ~ 100 MeV [122]. Below $\sim$ GeV, it is found that roughly equal fractions of protons, neutrons, and pions are produced in each collision [123]. We will thus have a roughly collinear shower terminating at an energy ~ 10 MeV which consists of pions for most of the shower's development and converts to an mix of pions and nucleons in the final decade of energy. This cascade is described by a radiative stopping power

$$\frac{dE}{dx} \sim n_{\rm ion}\sigma_{\rm inel}E, \tag{B.4}$$

where the inelastic nuclear cross section is given by $\sigma_{\rm inel} \approx 100$ mb and roughly constant in energy [122]. The total length of the shower is only logarithmically dependent on the initial hadron energy E,

$$X_{\rm had} \sim \frac{1}{n_{\rm ion}\sigma_{\rm inel}}\log\left(\frac{E}{E_{\rm nuc}}\right). \tag{B.5}$$

Photonuclear Interactions. Photons of energy greater than 10 MeV can also strongly interact with nuclei through the production of virtual quark-antiquark pairs. This is the dominant mode of photon energy loss at high energy. The photonuclear scatter destroys the photon and fragments the nucleus, producing secondary hadrons in a shower analogous to that described above. The photonuclear cross section $\sigma_{\gamma A}$ is roughly given by $\sigma_{\gamma A} \approx \alpha\sigma_{\rm inel}$, again ignoring the nuclear resonances that occur for $E \lesssim$ GeV [122]. For $E \gtrsim$ GeV, $\sigma_{\gamma A}$ is likely a slowly increasing function of energy due to the coherent interaction of the photon over multiple nucleons [124], however, instead of extrapolating this behavior we conservatively take a constant photonuclear cross section $\sigma_{\gamma A} \approx 1$ mb.

Electronuclear Interactions. Electrons can similarly lose energy to nuclei by radiating a virtual photon that undergoes a photonuclear scatter, which indeed provides the dominant energy loss for high energy electrons. The cross section for this process is roughly given by

the photonuclear cross section, scaled by a factor representing the probability to radiate such a photon. This can be estimated with the Weizsacker-Williams approximation, which gives a stopping power that is suppressed from the photonuclear result by α but enhanced by an $\mathcal{O}(10)$ logarithmic phase space factor [124]:

$$\frac{dE}{dx} \sim \alpha \; n_{\text{ion}} \sigma_{\gamma A} E \log\left(\frac{E}{m_e}\right). \tag{B.6}$$

Unlike the photonuclear interaction, the electronuclear event is a radiative process that preserves the original electron while leaving hadronic showers in its wake.

B.1.3 Radiative Processes

Electromagnetic showers due to successive bremsstrahlung and pair production events off carbon ions are the dominant stopping mechanisms for intermediate-energy electrons and photons. Both of these processes result in radiative stopping powers, derived semi-classically as [125]

$$\frac{dE}{dx} \sim \frac{E}{X_0}, \qquad X_0^{-1} = 4 n_{\text{ion}} Z^2 \frac{\alpha^3}{m_e^2} \log\Lambda. \tag{B.7}$$

X_0 is the well-known radiation length, and $\log\Lambda$ is a Coulomb form factor given by the range of effective impact parameters b:

$$\Lambda = \frac{b_{\text{max}}}{b_{\text{min}}}. \tag{B.8}$$

The maximal impact parameter is set by the plasma screening length (see B.1.4) and the minimum by the electron mass, below which the semi-classical description breaks down. Note that for the highest WD densities $\Lambda \lesssim 1$, in which case (B.7) ought be replaced by a fully quantum mechanical result as in [126]. This still results in a radiative stopping power, and so for simplicity we employ (B.7) with $\log\Lambda \sim \mathcal{O}(1)$ for all WD densities.

LPM Suppression A radiative event involving momentum transfer q to an ion must, quantum mechanically, occur over a length $\sim q^{-1}$. All ions within this region contribute to the scattering of the incident particle, and for sufficiently small q this results in a decoherence that suppresses the formation of photons or electron-positron pairs. This is the "Landau-Pomeranchuk-Midgal" (LPM) effect. The momentum transfer q in a given event decreases with increasing incident particle energy, and so the LPM effect will suppress radiative processes for energies greater than some scale E_{LPM}. This can be calculated semi-classically [125],

$$E_{\text{LPM}} = \frac{m_e^2 X_0 \alpha}{4\pi} \approx 1 \text{ MeV} \left(\frac{10^{32}\text{cm}^{-3}}{n_{\text{ion}}}\right). \tag{B.9}$$

which is quite small due to the high ion density in the WD. The stopping power for bremsstrahlung and pair production in the regime of LPM suppression $E > E_{\rm LPM}$ is

$$\frac{dE}{dx} \sim \frac{E}{X_0}\left(\frac{E_{\rm LPM}}{E}\right)^{1/2} \qquad E > E_{\rm LPM}. \tag{B.10}$$

In addition to the LPM effect, soft bremsstrahlung may be suppressed in a medium as the emitted photon acquires an effective mass of order the plasma frequency Ω_p. However, for high-energy electrons this dielectric suppression only introduces a minor correction to (B.10), in which soft radiation is already suppressed [125].

B.1.4 Elastic EM Scattering

Electron Coulomb Scattering off Ions. Coulomb collisions with ions are the mechanism by which electrons of energy $1-10$ MeV ultimately thermalize ions. In this scenario we may treat the ions as stationary and ignore their recoil during collisions. The nuclear charge will be screened by the mobile electrons of the medium, so incident particles scatter via a potential

$$V(\mathbf{r}) = \frac{Z\alpha}{r}e^{-r/\lambda_{\rm TF}}. \tag{B.11}$$

The screening length $\lambda_{\rm TF}$ is given in the Thomas-Fermi approximation by [127]:

$$\lambda_{\rm TF}^2 = \frac{E_F}{6\pi\alpha n_e} \sim \frac{1}{\alpha E_F^2}. \tag{B.12}$$

This plasma screening suppresses scatters with momentum transfers below $\sim \lambda_{\rm TF}^{-1}$, corresponding to a minimal energy transfer of $\omega_{\rm min} = \lambda_{\rm TF}^{-2}/2m_{\rm ion}$. Ions may in principle also cause screening through lattice distortion, however this may be ignored as the sound speed of the lattice $c_s \sim 10^{-2}$ is much smaller than the speed of an incident relativistic electron. From the Born approximation, the cross section for energy transfer ω is

$$\frac{d\sigma}{d\omega} = \frac{2\pi Z^2\alpha^2}{m_{\rm ion}v_{\rm in}^2}\frac{1}{(\omega+\omega_{\rm min})^2}, \tag{B.13}$$

where $v_{\rm in}$ is the incident velocity. Thus the stopping power is

$$\begin{aligned}\frac{dE}{dx} &= \int_0^{\omega_{\rm max}} d\omega\, n_{\rm ion}\frac{d\sigma}{d\omega}\omega \\ &\approx \frac{2\pi\, n_{\rm ion}Z^2\alpha^2}{m_{\rm ion}v_{\rm in}^2}\log\left(\frac{\omega_{\rm max}}{\omega_{\rm min}}\right),\end{aligned} \tag{B.14}$$

where the second line is valid if $\omega_{\rm max} \gg \omega_{\rm min}$. $\omega_{\rm max}$ is the maximum possible energy transfer. This may be due to 4-momentum conservation, or in the case of incident electrons, the

impossibility of scattering to a final energy less than E_F. 4-momentum conservation sets an upper bound $\omega_{\rm kin}$, which for a stationary target is

$$\omega_{\rm kin} = \frac{2m_{\rm ion}p^2}{m_{\rm ion}^2 + m^2 + 2Em_{\rm ion}}, \tag{B.15}$$

with p, E the incoming momentum and energy. The Fermi upper bound is $\omega_F = E - E_F$ so for incident electrons we take $\omega_{\rm max} = \min\{\omega_{\rm kin}, \omega_F\}$.

For scatters that transfer energy less than the plasma frequency Ω_p, one may be concerned about phonon excitations. This occurs for incident electrons with energy below ~ 10 MeV. We estimate this stopping power treating each ion as an independent oscillator with frequency Ω_p (an Einstein solid approximation) and compute the stopping power due to scatters which excite a single oscillator quanta. There are two key differences between this and the free ion case: incident particles must transfer an energy Ω_p, and the cross section to transfer momentum q is suppressed by a factor $q^2/2m_{\rm ion}\Omega_p = \omega_{\rm free}/\Omega_p$. $\omega_{\rm free}$ is the energy transfer that would accompany a free ion scatter with momentum transfer q. The resulting stopping power is unchanged from the free case (B.14), as the increased energy transfer compensates for the suppressed cross section.

As electrons transfer their energy at the rate (B.14), they occasionally experience a hard scatter with mean free path

$$\lambda_{\rm hard} \approx \frac{p^2 v_{\rm in}^2}{\pi n_{\rm ion} Z^2 \alpha^2}. \tag{B.16}$$

For sufficiently small incident energies, the electron experiences several hard scatters before it has deposited its energy by elastic scatters, and the stopping length is reduced by the resulting random walk. This effect is not significant for incident pions due to their larger mass.

Finally, we note that for highly energetic incident particles the cross section (B.13) should be modified to account for the recoil of the ion. However, at such energies the dominant stopping power will be from hadronic or electromagnetic showers anyway, so we do not include these recoil effects.

Relativistic Coulomb Scattering off Electrons. The scattering of incident electrons off degenerate electrons determines the termination energy of electromagnetic showers. This calculation demands two considerations not present when scattering off ions: the targets are not stationary and they require a threshold energy transfer in order to be scattered out of the Fermi sea. However for relativistic incident particle, with momentum $p \gg p_F$, the stopping power off electrons is ultimately of the same form as the stopping power off ions (B.14). In this limit, all particle velocities and the relative velocity is $\mathcal{O}(1)$, and the deflection of the incident particle will generally be small. It is reasonable then that scattering proceeds, up to $\mathcal{O}(1)$ factors, as though a heavy incident particle is striking a light, stationary target. The

cross section is given by the usual result,

$$\frac{d\sigma}{d\omega} \approx \frac{2\pi\alpha^2}{E_F}\frac{1}{\omega^2}, \tag{B.17}$$

where we have accounted for the target's motion by replacing its mass with its relativistic inertia $\approx E_F$. This is equivalent to a boost of the cross section from the rest frame of the target into the WD frame. Note that plasma screening can be ignored in this case, as Pauli-blocking will provide a more stringent cutoff on soft scatters. Scatters which transfer an energy $\omega \leq E_F$ will have a suppressed contribution to the stopping power as they can only access a fraction of the Fermi sea. In this limit it is sufficient to ignore these suppressed scatters:

$$\begin{aligned}\frac{dE}{dx} &= \int_{E_F}^{\omega_{\max}} d\omega\, n_e \frac{d\sigma}{d\omega}\omega \\ &\approx \frac{2\pi\, n_e\alpha^2}{E_F}\log\left(\frac{\omega_{\max}}{E_F}\right)\end{aligned} \tag{B.18}$$

where, as described above, $\omega_{\max} = \min\{\omega_{\rm kin}, \omega_F\}$. This derivation is admittedly quite heuristic, and so it has been checked with a detailed numerical calculation accounting fully for the target's motion and degeneracy. Equation (B.18) is indeed a good approximation to the stopping power for incident energies larger than the Fermi energy.

Non-Relativistic Coulomb Scattering off Electrons For non-relativistic incident particles, the Coulomb stopping off electrons becomes strongly suppressed due to degeneracy. Stopping in this limit appears qualitatively different than in the typical case—the slow incident particle is now bombarded by relativistic electrons from all directions. Note that only those scatters which slow the incident particle are allowed by Pauli-blocking.

As the electron speeds are much faster than the incident, a WD electron with momentum p_F will scatter to leading order with only a change in direction, so the momentum transfer is $|\vec{q}| \sim p_F$. We again take the incident momentum $p \gtrsim p_F$, which is valid for all incident particles we consider. This results in an energy transfer

$$\omega = \left|\frac{p^2}{2m} - \frac{(\vec{p}-\vec{q})^2}{2m}\right| \sim v_{\rm in}E_F. \tag{B.19}$$

For $v_{\rm in} \ll 1$ the energy transfer is less than Fermi energy, so Pauli-blocking will be important. The incident particle is only be able to scatter from an effective electron number density

$$n_{\rm eff} = \int_{E_F-\omega}^{E_F} g(E)\, dE \approx 3n_e\frac{\omega}{E_f}, \tag{B.20}$$

where $g(E)$ is the Fermi density of states. At leading order the electron is not aware of the small incident velocity, so the cross section is given by relativistic Coulomb scattering off

a stationary target $\sigma \sim \alpha^2/q^2$ [128]. The incident particle thus loses energy to degenerate electrons at a rate:

$$\frac{dE}{dt} \sim n_{\text{eff}}\, \sigma\, \omega \sim n_e \frac{\alpha^2}{E_F} v_{\text{in}}^2. \tag{B.21}$$

Note that this includes a factor of the relative velocity which is $\mathcal{O}(1)$. As a result, the stopping power is parametrically

$$\frac{dE}{dx} = \frac{1}{v_{\text{in}}} \frac{dE}{dt} \sim n_e \frac{\alpha^2}{E_F} v_{\text{in}}. \tag{B.22}$$

As above, this heuristic result has been verified with a full integration of the relativistic cross section.

We can compare (B.22) to the stopping power of non-relativistic, heavy particles off roughly stationary, non-degenerate electrons $\frac{dE}{dx} \sim n_e \frac{\alpha^2}{m_e v_{\text{in}}^2}$, which is the familiar setting of stopping charged particles in a solid due to ionization [129]. Evidently, the analogous stopping in a WD is parametrically suppressed by $v_{\text{in}}^3 m_e/E_F$. One factor of v_{in} is due to Pauli blocking, while the other factors are kinematic, due to the relativistic motion of the targets.

Compton Scattering Compton scattering off degenerate electrons is the dominant interaction for photons of incident energy $k \leq E_F$. As we will show, this stopping power is parametrically different from that of high-energy photons due to Pauli-blocking and the motion of the electron. For $k > E_F$, the effect of Pauli-blocking is negligible and the stopping power is simply:

$$\frac{dk}{dx} \sim \frac{\pi \alpha^2 n_e}{E_F} \log\left(\frac{k}{m_e}\right), \tag{B.23}$$

where again we have (partially) applied the heuristic $m_e \to E_F$ replacement to boost the usual result for stationary electrons while avoiding divergence at the Fermi energy. This, along with the low-energy estimate below, matches a full integration of the relativistic cross section well.

We now turn to the regime of interest, $k < E_F$. Only those electrons near the top of the Fermi sea are available to scatter, so the photon interacts with only the effective electron density (B.20). In addition, Compton scatters will only occur off electrons moving roughly collinear with the photon momentum - a head-on collision would result in an energy loss for the electron, which is forbidden by Pauli exclusion. In the electron rest frame these collinear scatters are Thompson-like, and the photon energy loss is dominated by backward scatters. For relativistic electrons near the Fermi surface, these scatters transfer an energy

$$\omega \sim k\left(1 - \frac{m_e^2}{4E_F^2}\right) \approx k. \tag{B.24}$$

The cross section can be taken in the electron rest frame $\sigma \sim \alpha^2/m_e^2$, along with an 'aiming' factor $1/4\pi$ to account for the restriction to initially parallel trajectories. This gives a stopping power

$$\frac{dk}{dx} \approx \frac{\alpha^2 n_e k^2}{4\pi m_e^2 E_F}. \tag{B.25}$$

B.2 Dark Matter Capture

Here we give a more detailed discussion of DM capture in a WD and its subsequent evolution. For the remainder of this appendix all numerical quantities are evaluated at a central WD density $\rho_{\rm WD} \sim 3 \times 10^8 \frac{\rm g}{\rm cm^3}$ ($n_{\rm ion} \sim 10^{31}$ cm^{-3}), for which the relevant WD parameters are [94]: $M_{\rm WD} \approx 1.25\ M_\odot$, $R_{\rm WD} \approx 4000$ km, and $v_{\rm esc} \approx 2 \times 10^{-2}$. Depending on the context, the relevant density may be the average value which we take to be $\sim 10^{30}$ cm^{-3}. We also assume an average value of the WD temperature $T_{\rm WD} \sim$ keV.

B.2.1 Capture Rate

Consider spin-independent DM elastic scattering off ions with cross section $\sigma_{\chi A}$. This is related to the per-nucleon cross section

$$\sigma_{\chi A} = A^2 \left(\frac{\mu_{\chi A}}{\mu_{\chi n}}\right)^2 F^2(q) \sigma_{\chi n} = A^4 F^2(q) \sigma_{\chi n}, \tag{B.26}$$

where $F^2(q)$ is the Helm form factor [130]. If the DM is at the WD escape velocity, the typical momentum transfer to ions is $q \sim \mu_{\chi A} v_{\rm esc} \sim 200$ MeV. As this q is less than or of order the inverse nuclear size, DM scattering off nuclei will be coherently enhanced. We find $F^2(q) \approx 0.1$ for $q \sim 200$ MeV.

For the DM to ultimately be captured, it must lose energy $\sim m_\chi v^2$, where v is the DM velocity (in the rest frame of the WD) asymptotically far away. Since typically $v \ll v_{\rm esc}$, the DM has velocity $v_{\rm esc}$ while in the star and must lose a fraction $(v/v_{\rm esc})^2$ of its kinetic energy to become captured. Properly, the DM velocity is described by a boosted Maxwell distribution peaked at the galactic virial velocity $v_{\rm halo} \sim 10^{-3}$. However, this differs from the ordinary Maxwell distribution by only $\mathcal{O}(1)$ factors [98], and we can approximate it by (ignoring the exponential Boltzmann tail):

$$\frac{dn_\chi}{dv} \approx \begin{cases} \frac{\rho_\chi}{m_\chi}\left(\frac{v^2}{v_{\rm halo}^3}\right) & v \le v_{\rm halo} \\ 0 & v > v_{\rm halo} \end{cases}. \tag{B.27}$$

The DM capture rate is given by an integral of the DM transit rate weighted by a probability for capture $P_{\rm cap}$

$$\Gamma_{\rm cap} \sim \int dv \frac{d\Gamma_{\rm trans}}{dv} P_{\rm cap}(v), \tag{B.28}$$

where the (differential) transit rate is

$$\frac{d\Gamma_{\rm trans}}{dv} \sim \frac{dn_\chi}{dv} R_{\rm WD}^2 \left(\frac{v_{\rm esc}}{v}\right)^2 v. \tag{B.29}$$

$P_{\rm cap}$ depends on both the *average* number of scatters in a WD

$$\overline{N}_{\rm scat} \sim n_{\rm ion} \sigma_{\chi A} R_{\rm WD}, \tag{B.30}$$

and the number of scatters *needed* for capture

$$N_{\rm cap} \sim \max\left\{1, \frac{m_\chi v^2}{m_{\rm ion} v_{\rm esc}^2}\right\}, \tag{B.31}$$

and is most generally expressed as a Poisson sum

$$P_{\rm cap} = 1 - \sum_{n=0}^{N_{\rm cap}-1} \exp(-\overline{N}_{\rm scat}) \frac{(\overline{N}_{\rm scat})^n}{n!}. \tag{B.32}$$

For our purposes we will approximate the sum as follows:

$$P_{\rm cap} \approx \begin{cases} 1 & \overline{N}_{\rm scat} > N_{\rm cap} \\ \overline{N}_{\rm scat} & \overline{N}_{\rm scat} < N_{\rm cap} \text{ and } N_{\rm cap} = 1 \\ 0 & \text{else} \end{cases}. \tag{B.33}$$

Here we ignore the possibly of capture if $\overline{N}_{\rm scat} < N_{\rm cap}$ except in the special case that only one scatter is needed for capture. If $\overline{N}_{\rm scat} > N_{\rm cap}$, we assume all DM is captured. Most accurately, this capture rate should be computed numerically, e.g. see [131]. However with the above simplifications we find that the capture rate is of order

$$\Gamma_{\rm cap} \sim \Gamma_{\rm trans} \cdot \min\left\{1, \overline{N}_{\rm scat} \min\{B, 1\}\right\}, \tag{B.34}$$
$$B \equiv \frac{m_{\rm ion} v_{\rm esc}^2}{m_\chi v_{\rm halo}^2}.$$

B here encodes the necessity of multiple scattering for capture. For ultra-heavy DM $m_\chi > 10^{15}$ GeV, $B \ll 1$ and essentially multiple scatters are always needed.

B.2.2 Thermalization and Collapse

Once DM is captured, it thermalizes to an average velocity

$$v_{\rm th} \sim \sqrt{\frac{T_{\rm WD}}{m_\chi}} \approx 10^{-11} \left(\frac{m_\chi}{10^{16}\ {\rm GeV}}\right)^{-1/2}, \tag{B.35}$$

and settles to the thermal radius

$$R_{\rm th} \sim \left(\frac{T_{\rm WD}}{G m_\chi \rho_{\rm WD}}\right)^{1/2} \approx 0.1 \text{ cm} \left(\frac{m_\chi}{10^{16} \text{ GeV}}\right)^{-1/2},$$

where its kinetic energy balances against the gravitational potential energy of the (enclosed) WD mass. This thermalization time can be explicitly calculated for elastic nuclear scatters [132]. The stopping power due to such scatters is

$$\frac{dE}{dx} \sim \rho_{\rm WD} \sigma_{\chi A}\, v\, \max\{v, v_{\rm ion}\}, \tag{B.36}$$

where $v_{\rm ion} \sim \sqrt{T_{\rm WD}/m_{\rm ion}}$ is the thermal ion velocity. The max function indicates the transition between "inertial" and "viscous" drag, as the DM velocity v slows to below $v_{\rm ion}$. DM first passes through the WD many times on a wide orbit until the size of its orbit decays to become contained in the star. The timescale for this process is

$$\begin{aligned} t_1 &\sim \left(\frac{m_\chi}{m_{\rm ion}}\right)^{3/2} \frac{R_{\rm WD}}{v_{\rm esc}} \frac{1}{\overline{N}_{\rm scat}} \frac{1}{\max\{\overline{N}_{\rm scat}, 1\}^{1/2}} \\ &\approx 7 \times 10^{16} \text{ s} \left(\frac{m_\chi}{10^{16} \text{ GeV}}\right)^{3/2} \left(\frac{\sigma_{\chi A}}{10^{-35} \text{ cm}^2}\right)^{-3/2}. \end{aligned} \tag{B.37}$$

Subsequently, the DM completes many orbits within the star until dissipation further reduces the orbital size to the thermal radius. The timescale for this process is

$$\begin{aligned} t_2 &\sim \left(\frac{m_\chi}{m_{\rm ion}}\right) \frac{1}{n_{\rm ion} \sigma_{\chi A}} \frac{1}{v_{\rm ion}} \\ &\approx 10^{14} \text{ s} \left(\frac{m_\chi}{10^{16} \text{ GeV}}\right) \left(\frac{\sigma_{\chi A}}{10^{-35} \text{ cm}^2}\right)^{-1}. \end{aligned} \tag{B.38}$$

There is an additional $\mathcal{O}(10)$ logarithmic enhancement of the timescale once the DM velocity has slowed below $v_{\rm ion}$. Note that time to complete a single orbit is set by the gravitational free-fall timescale:

$$t_{\rm ff} \sim \sqrt{\frac{1}{G \rho_{\rm WD}}} \approx 0.5 \text{ s}. \tag{B.39}$$

In the above description, we have assumed that the DM loses a negligible amount of energy during a single transit:

$$\frac{\sigma_{\chi A}}{m_\chi} \ll \frac{1}{\rho_{\rm WD} R_{\rm WD}}. \tag{B.40}$$

This also ensures that the dynamics of DM within the star is that of Newtonian gravity along with a small drag force. In the opposite regime, the qualitative evolution of captured DM differs from the picture presented in detail below. In this case there is no stage of external orbital motion corresponding to t_1—DM will instead rapidly thermalize to a speed $v_{\rm th}$ after

entering the star. The internal motion now proceeds as a gravitationally-biased random walk, with a net drift of DM towards the center of the star. For sufficiently large $\sigma_{\chi A}$, DM will collect at a radius $r_{\rm c}$ which is larger than $r_{\rm th}$ given above, due to a balance of gravity with outward Brownian diffusion. This may delay the onset of self-gravitation, possibly beyond $\tau_{\rm WD}$, as we now require the collection of a larger mass $\rho_{\rm WD} r_{\rm c}^3$. It is important to note that the differences between the Brownian and orbital regimes are immaterial for constraints on the decay of captured DM (e.g., Figure 4.10), which cares only about the quantity of DM present in the star. For annihilation constraints, however, the internal evolution of DM is quite important. For the largest unconstrained cross sections $\sigma_{\chi A}$ (see Figure 4.11), one can check that captured DM is distributed across a large fraction of the star due to Brownian motion and does not collapse. This DM population still yields a strong constraint on $\sigma_{\chi\chi}$, similar to but somewhat weaker than the constraints which can be placed on DM that undergoes self-gravitational collapse after capture (e.g., Figure 4.9).

When Brownian motion is insignificant, the DM will begin steadily accumulating at $R_{\rm th}$ after a time $t_1 + t_2$. Once the collected mass of DM at the thermal radius exceeds the WD mass within this volume, there is the possibility of self-gravitational collapse. The time to collect a critical number $N_{\rm sg}$ of DM particles is

$$\begin{aligned} t_{\rm sg} &\sim \frac{N_{\rm sg}}{\Gamma_{\rm cap}} \sim \frac{\rho_{\rm WD} R_{\rm th}^3}{m_\chi \Gamma_{\rm cap}} \\ &\approx 10^{10}\ {\rm s} \left(\frac{m_\chi}{10^{16}\ {\rm GeV}}\right)^{-1/2} \left(\frac{\sigma_{\chi A}}{10^{-35}\ {\rm cm}^2}\right)^{-1}, \end{aligned} \tag{B.41}$$

Typically, the timescale for collapse is then set by the DM sphere's ability to cool and shed gravitational potential energy. This is initially just t_2, while the time to collapse at any given radius r decreases once the DM velocity rises again above $v_{\rm ion}$:

$$\begin{aligned} t_{\rm cool} &\sim t_2 {\rm min}\{v_{\rm ion}/v_\chi, 1\} \\ v_\chi &\sim \sqrt{\frac{GNm_\chi}{r}}, \end{aligned} \tag{B.42}$$

where N is the number of collapsing DM particles. Note that when $m_\chi > 10^{21}$ GeV, the number of particles necessary for self-gravitation $N_{\rm sg}$ as defined in (B.41) is less than 2. In this case we should formally take $N_{\rm sg} = 2$.

Finally, there is a further subtlety that arises in the growing of DM cores for the large DM masses m_χ of interest to us. The time $t_{\rm sg}$ to collect a self-gravitating number of particles decreases for larger DM masses. However, the dynamics of the collapse are set by the cooling time, which is initially $t_{\rm cool} \propto m_\chi$. For $m_\chi > 10^{15}$ GeV, the collection time may be shorter than the cooling time $t_{\rm sg} < t_{\rm cool}$ (depending on the cross section). In fact, the collection time may even be shorter than the dynamical time $t_{\rm ff}$. If $t_{\rm ff} < t_{\rm sg} < t_{\rm cool}$, the DM core will be driven to shrink because of the gravitational potential of the over-collecting DM. The timescale for the shrinking is set by the capture rate of DM. Ultimately, the collapsing DM core will consist of $N_{\rm sg}$ enveloped in a "halo" of $\Gamma_{\rm cap} t_{\rm cool} \gg N_{\rm sg}$ particles, which will also

proceed to collapse. If instead $t_{\rm sg} < t_{\rm ff} < t_{\rm cool}$, the DM core will rapidly accumulate to this large number before dynamically adjusting. For the purpose of the collapse constraints on DM annihilation, if $t_{\rm sg} < t_{\rm cool}$ we will simply assume a number of collapsing particles $N = \Gamma_{\rm cap} t_{\rm cool}$. This is the case for the constraints plotted in Figure 4.9.